UNIVERSITY OF WARMIA AND MAZURY IN OLSZTYN

Technical Sciences

23(2) 2020

OLSZTYN 2020

Editorial Board

Ceslovas Aksamitauskas (Vilnius Gediminas Technical Univetsity, Lithuania), Olivier Bock (Institut National de L'Information Géographique et Forestiére, France), Stefan Cenkowski (University of Manitoba, Canada), Adam Chrzanowski (University of New Brunswick, Canada), Davide Ciucci (University of Milan-Bicocca, Italy), Sakamon Devahastin (King Mongkut's University of Technology Thonburi in Bangkok, Thailand), German Efremov (Moscow Open State University, Russia), Mariusz Figurski (Military University of Technology, Poland), Maorong Ge (Helmholtz--Zentrum Potsdam Deutsches GeoForschungsZentrum, Germany), Dorota Grejner-Brzezinska (The Ohio State University, USA), Janusz Laskowski (University of Life Sciences in Lublin, Poland), Arnold Norkus (Vilnius Gediminas Technical University, Lithuania), Stanisław Pabis (Warsaw University of Life Sciences-SGGW, Poland), Lech Tadeusz Polkowski (Polish-Japanese Institute of Information Technology, Poland), Arris Tijsseling (Technische Universiteit Eindhoven, Netherlands), Vladimir Tilipalov (Kaliningrad State Technical University, Russia), Alojzy Wasilewski (Koszalin University of Technology, Poland)

Editorial Committee

Marek Markowski (Editor-in-Chief), Piotr Artiemjew, Kamil Kowalczyk, Wojciech Sobieski, Piotr Srokosz, Magdalena Zielińska (Assistant Editor), Marcin Zieliński

Features Editors

Piotr Artiemjew (Information Technology), Marcin Dębowski (Environmental Engineering), Zdzisław Kaliniewicz (Biosystems Engineering), Grzegorz Królczyk (Materials Engineering), Marek Mróz (Geodesy and Cartography), Ryszard Myhan (Safety Engineering), Wojciech Sobieski (Mechanical Engineering), Piotr Srokosz (Civil Engineering), Jędrzej Trajer (Production Engineering)

Statistical Editor
Paweł Drozda

Executive Editor
Mariola Jezierska

The Technical Sciences is indexed and abstracted in BazTech (http://baztech.icm.edu.pl) and in IC Journal Master List (http://journals.indexcopernicus.com)

The Journal is available in electronic form on the web sites
http://www.uwm.edu.pl/techsci (subpage Issues)
http://wydawnictwo.uwm.edu.pl (subpage Czytelnia)

The electronic edition is the primary version of the Journal

PL ISSN 1505-4675
e-ISSN 2083-4527

© Copyright by Wydawnictwo UWM ● Olsztyn 2020

Address
ul. Jana Heweliusza 14
10-718 Olsztyn-Kortowo, Poland
tel.: +48 89 523 36 61
fax: +48 89 523 34 38
e-mail: wydawca@uwm.edu.pl

Ark. wyd. 7,0, ark. druk. 6,0, nakład 75 egz.
Druk – Zakład Poligraficzny UWM, zam. 16

Contents

Technical Sciences, 2020, 23(2), 115–130

UNIWERSYTET WARMIŃSKO-MAZURSKI W OLSZTYNIE

Quarterly peer-reviewed scientific journal
ISSN 1505-4675
e-ISSN 2083-4527
TECHNICAL SCIENCES
Homepage: www.uwm.edu.pl/techsci/

DOI: https://doi.org/10.31648/ts.5644

GEOMETRY EXTRACTION FROM GCODE FILES DESTINED FOR 3D PRINTERS

***Wojciech Kiński*[1], *Wojciech Sobieski*[2]**

[1]ORCID: 0000-0003-4973-7604
Department of Mechanical Engineering and Fundamentals of Machine Design
University of Warmia and Mazury, Olsztyn
[2]ORCID: 0000-0003-1434-5520
Department of Mechanical Engineering and Fundamentals of Machine Design
University of Warmia and Mazury, Olsztyn

Received 01 July 2020, accepted 22 July 2020, available online 22 July 2020.

Key words: GCODE, STL, additive manufacturing, 3D printers, reverse engineering.

Abstract

The paper presents a method of conversion of GCODE files designed for additive manufacturing in 3D printers to a format which may be conveniently visualized. In the investigations three different 3D models were created: a) shell model (a casing); b) solid model (a gear); c) model with curvilinear elements (a screw). All these models were converted to GCODE files. Next the reverse engineering was applied and GCODE files were converted to points sets. These points represent particular locations of the print head. In the developed algorithm the linear interpolation was added to obtain intermediate points between locations of the print head for longer sections. The final part shows an attempt of applying Poisson Surface Reconstruction in order to obtain the original geometry. The main motivation to develop a new software resulted from the observation that sometimes the original solid model is no longer available, while there is a need to change some geometry details or settings before production stage.

Correspondence: Wojciech Sobieski, Katedra Mechaniki i Podstaw Konstrukcji Maszyn, Wydział Nauk Technicznych, Uniwersytet Warmińsko-Mazurski, ul. M. Oczapowskiego 11, 10-957 Olsztyn, phone +48 (89) 523 32 40, e-mail: wojciech.sobieski@uwm.edu.pl.

Introduction

Nowadays the additive manufacturing (3D printing) are very popular and their importance grows every year. They are used in many areas of mechanical engineering (SHAHI 2016), material engineering (SZEBÉNYI et al. 2017), civil engineering (SHATORNAYA et al. 2017, TAY et al. 2017), architecture (MATHUR 2016), chemical sciences (PARRA-CABRERA et al. 2018), electronics (XU et al. 2016), medicine (HANGGE et al. 2018, TAPPA et al. 2017), food industry (GODOI et al. 2016, PITAYACHAVAL et al. 2018) and others. To obtain any printed object, in the first place its geometry, considering the limitations of the additive manufacturing technology, must be defined. To reach this aim, any software destined for preparing 3D geometry (in the STL file format) may be used. At this stage the assumptions related to the material used must be taken into account, too. It is also very important to note that virtual geometry cannot be printed directly with the use of a 3D printer. The geometry must be first converted to a set of instructions which will be sequentially read and executed by the printer (Fig. 1).

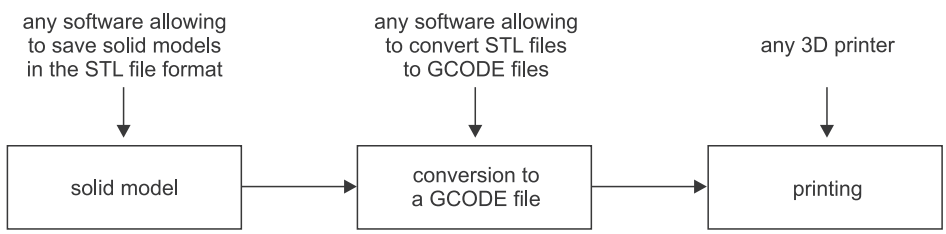

Fig. 1. Data flow from a solid model to the finished product

In particular, the movement of the print head and the material feeding speed must be specified. Here, a specific programming language, the so-called GCODE, is usually used (also RS-274; KRAMER et al. 2000). GCODE is a standardized command language that is used to operatenumerically controlled devices (CNC) (ISO 6983-1:2009). The main motivation to develop a new software resulted from own practical experience. It turns out that sometimes the original 3D solid model is no longer available, but a need arises to change some details of the geometry or settings of the printing process. Two options are possible in such a case: creation of the solid model from the beginning or converting the existing GCODE file to a format, which may be modify. The hereby paper is a try to apply the second approach. The possibility to save the time needed to prepare a second solid model is the main advantage of the idea presented.

The methodology applied covers four steps:

– preparing exemplary geometries in the STL format;
– converting STL files to GCODE files;

– decoding GCODE files to obtain a points set representing the subsequent coordinates of positioning the print head;

– surface reconstructing on the basis of the points set.

It should be noted that there are publications related to data conversion from STL files to GCODE files (so-called slicing) (GUERRERO-DE-MIERA et al. 2015, HU 2017, TOPÇU et al. 2011) or printing quality (BAUMANN et al. 2016, WANG et al. 2014) as well as articles on reverse engineering dealing with the use of 3D printers and scanners (BARONIO et al. 2016, DÚBRAVČÍK, KENDER 2012, ESLAMI 2017). However, among them the papers related to decoding of the GCODE language are very rare. Apparently, to the best of our knowledge, there is only one paper alluding to this issue (BAUMANN et al. 2017). In this paper a reconstruction algorithm is briefly presented. The Authors use similar methodology to ours, but the tools applied by them are different and they illustrate the algorithm with only one example. In particular, the software for slicing a STL model was different (Slic3r, v. 1.2.9 and the main programming language was Python). We tried to compare our code with the software developed by them, but it turned out, that the webpage indicated by the Authors in the paper (BAUMANN et al. 2017) is not available.

Materials and Methods

Materials

The object of analysis is a set of three files in the GCODE format which are intended for the execution of selected geometric objects with the use of 3D printing technique. Three basic types of shapes were taken into account (i.e. flat, solid and curved) and the most important instructions used in source files for 3D printers.

GCODE programming language

The GCODE language is a standardized command language that is very oft used to operate numerically controlled (CNC) devices (ISO 6983-1:2009). The source code in GCODE language consists of a series of individual instructions which, depending on the device, are able to make details by subtractive (e.g. CNC milling machine) or additive (3D printer) manufacturing. The GCODE commands (Tab. 1) can be created by using the following methods:

– creating a list of commands in a text editor;

– preparing the code using CAM software;

– entering commands directly via the control panel of the device.

In practice, due to the complexity of the geometry of the processed model, it is mainly the software dedicated to a given device class that is used. In the context of the paper important is, that programs "cutting" three-dimensional objects mainly use the commands of simple linear motions. They do not use G2 and G3 commands that use circular motion. The cutting software treats each arc as a set of straight sections.

Table 1

Examples of GCODE language commands used in 3D printers

Command	Description	Sample
G0	Fast movement	G0 X12
G1	Work movement by linear interpolation	G1 X90.6 Y13.8 E22.4
G2	Circular motion in a clockwise direction	G2 X90.6 Y13.8 I5 J10 E22.4
G3	Movement around the circle counter-clockwise	G3 X40.6 Y11.7 I5 J10 E72.4
G28	Axis reset	G28

Source: based on HABRAT (2007).

Poisson Surface Reconstruction

There are two groups of surface reconstruction methods based on a points set: explicit methods, in which the surface must pass through all points of the set, and implicit ones in which the surface is approximated on the basis of on the points locations (NORLANDER 2017). However, due to the drawbacks of the explicit methods (which are usually based on the Delaunay algorithm) such as high sensitivity to data quality and high demand for computing power, there were developed implicit methods, such as MarchingCubes (LORENSEN, CLINE 1987) or Poisson Surface Reconstruction (KAZHDAN et al. 2006), that are most commonly used since they are more resistant and faster.

The Poisson Surface Reconstruction is based on calculating the so-called indicator function X (a scalar function), whose value is one (inside the surface) and zero (outside the surface). If this function is known, then the reconstructed surface may be obtained by extracting an appropriate iso-surface. In the Poisson method an oriented points set can be treated as a sampling of the gradient of the indicator function. In the consequence, the discrete points set may be used to define a continuous vector field $\vec{V}$ representing the gradient field of the indicator function. Solving the indicator function X then amounts to finding the scalar function whose gradient best matches $\vec{V}$. To reach this aim, the Poisson equation must be solved:

$$\Delta X = \nabla \cdot \vec{V} \tag{1}$$

where:

$\vec{V}$ – the smoothed normal field.

Results and Discussion

Solid models

The aim of the first stage of investigations is to create a set of models of three-dimensional objects, taking into account the most common geometric features of elements made on 3D printers. For testing, one thin-wall structure (casing – Fig. 2*a*), one full structure (gear – Fig. 2*b*) and one structure containing curved sections (screw – Fig. 2*c*) were prepared. The geometries were created in the SolidWorks program and then saved in the form of STL files. The dimensions of objects in the context of this study are irrelevant.

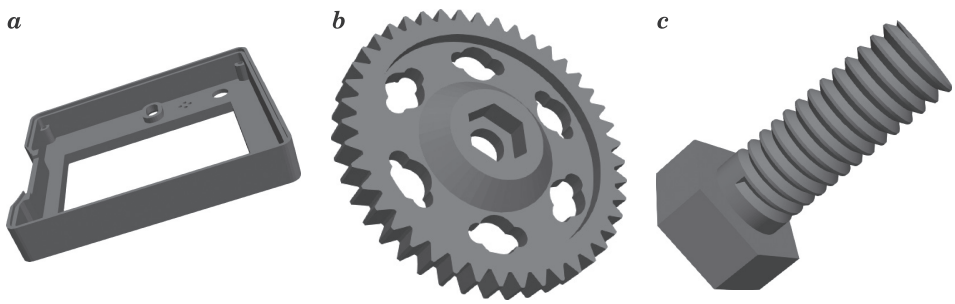

Fig. 2. 3D models used in investigations; *a* – casing, *b* – gear, *c* – screw

Generation of sample GCODE files

Having prepared the geometry of selected objects in the form of STL files, in the second stage of the investigations three GCODE files were created – one for each geometry. These files were prepared with the use of the MatterControl program (MatterControl Home Page 2019). This is a free Open Source application that is used to construct 3D objects for 3D printing. The preparation of the GCODE file requires a number of parameters characterizing a specific device as well as the properties of the 3D printing process itself, such as the layer height or wall thickness. A typical GCODE source file contains the following sections:

– header – consists of several lines of comments (always beginning with a semicolon) informing about the version of the software used, the wall thickness of the model, the width of the extruded path and the diameter of the beam of the material being fed;

– pre-processing data – consists of commands informing about the type and location of the centre of the coordinate system used and of commands used to prepare the print head and working platform (e.g. heating up to the set temperature);

– work area – consists of rows which specify the next positions of the print head and the current material feeding speeds;

– print completion area – consists of commands to be made after printing the model, such as axis homing, turning off the print head heaters and the work platform;

– footer – consists of lines informing about print parameters, such as material feeding speed, type and density of the model filling and many others.

```
; Generated with MatterSlice 1.0
; filamentDiameter = 1.75
; extrusionWidth = 0.4
; firstLayerExtrusionWidth = 0.52
; layerThickness = 0.2
; firstLayerThickness = 0.3
; automatic settings before start_gcode
G21 ; set units to millimeters
M107 ; fan off
T0 ; set the active extruder to 0
; settings from start_gcode
G28 X0;
G28 Y0;
G1 X82 Y82 F5000;
G28 Z0;
G1 Z5 F5000;
; automatic settings after start_gcode
T0 ; set the active extruder to 0
G90 ; use absolute coordinates
G92 E0 ; reset the expected extruder position
M82 ; use absolute distance for extrusion
; Layer count: 45
; Layer Change GCode
; LAYER:0
M400
M107
G0 F7800 X0 Y0 Z0.3
G0 X45.711 Y45.733
G0 X58.561 Y56.444
G0 X59.362 Y57.337
G0 X60.343 Y57.86
G0 X63.469 Y65.796
G0 X63.223 Y66.21
G0 X62.918 Y66.229
G0 X62.087 Y66.421
```

Fig. 3. Fragment of the GCODE language code for printing a model of a gear

Typically, for one specific printing device, the information necessary for the preparation and completion of printing is entered once (Tab. 2). This information is then duplicated for the subsequently generated GCODE files. In the context of the current article, it is important to emphasize that individual sections do not have any markers defining their scope. The beginnings and ends of the section

are determined by analysing the instructions of the following lines. An initial part of a source file taken from one of the examples described in the further part of the paper is shown in Figure 3. In this figure, the work area begins with the 27th line of code (highlighted).

Table 2

Parameters characterizing the generated GCODE files

Name	Value
Layer height	0.3 [mm]
Infill	20 [%]
Type of infill	grid an angle 45
Permiters	2
The number of bottom layers completely filled	4
The number of top layers completely filled	4

A characteristic feature of GCODE files is that full objects are usually printed in the form of a shell filled with a lattice structure (with different shapes of such structures). This saves the material and significantly speeds up the printing process. An example of a model of a gear with a truss type fill is shown in Figure 4 (mid-model view).

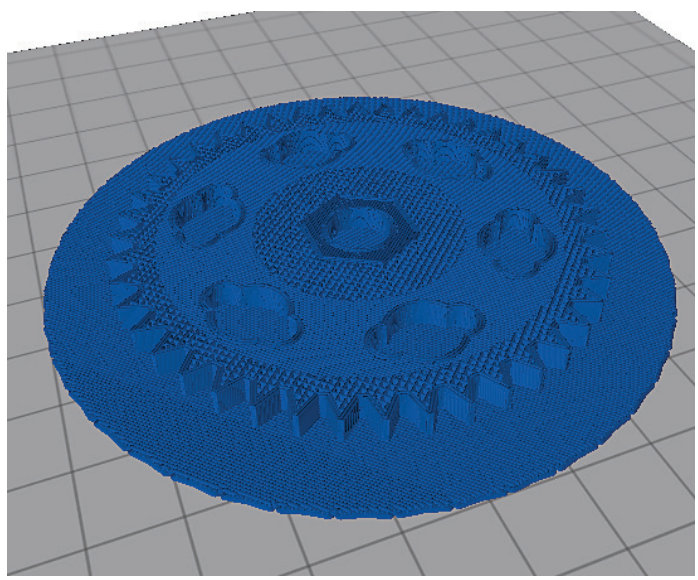

Fig. 4. View of the gear model in the MatterControl program

Geometry extraction

Currently available computer programs allow the visualization of GCODE files (jView 2020, NC Viewer 2020). However, they show usually not the geometry of the three-dimensional object but the trajectory of the printing head. For this reason they are not enough functional, if the User want re-select individual 3D printing parameters (e.g. specify the type and type of filling or change the height of the model layer).

In order to reproduce the geometry of an object for 3D printing based on a GCODE file, the coordinates of the subsequent positions of the print head must be known. Other parameters, such as filler temperature or feed speed, do not matter, but they can be useful for locating characteristic code fragments. The basis of the algorithm used in this investigation is to search for and then store the X, Y and Z coordinate values in the subsequent lines of code. To realize this, subsequent lines of the source code are read (as individual text variables), and then by means of text functions of a given programming language, the existence of specific sequences of characters in these lines is checked. The search starts with a line containing the "LAYER: 0" sequence (denoting the beginning of printing of the first layer) and ends with the line of the "M104 S0" sequence (which means switching off the heating of the print head, and consequently the end of the printing process). The numbers of these lines are denoted by variables n_{start} and n_{stop}, respectively. It is important to note that the Z coordinate of the first layer (denoted by Z0 symbol) may be sometimes defined before the n_{start} line. Therefore, it should be always checked if this is the case and remember the initial value of this coordinate.

Scanning a single line of the code, understood as a multi-character text variable, includes the following steps:

– checking if the coordinate mark (X, Y or Z) is present in the line;

– finding and saving the characters located between the coordinate mark and the nearest space or between the coordinate mark and the end of the line;

– converting characters into numbers and saving the result.

It is important to make sure that each line of the code is checked several times in order to find the current coordinate values X, Y and Z one by one. If the coordinate mark does not exist in the line being scanned, then the current coordinate value is taken as the previously read value. This means that the print head moves parallel to one of the Cartesian coordinate axes. In such cases, there is no need to duplicate the same coordinate, so that the files have a smaller volume. The values of read variables can be saved directly to a file or can be stored in indexed variables. The size of such variables can be determined on the basis of the knowledge of n_{start} and n_{stop}.

A Fortran (GNU Fortran Home Page 2019) code was written to decode GCODE files, using internal SCAN and INDEX text functions. The first function allows

to determine the position of a single character in a text string (e.g. character *X*), the second function determines the position of a particular character subsystem (e.g. the "LAYER: 0" sequence). The resulting data, i.e. the coordinates of all points found, were saved in the form of ASC and VTK files (The Visualization Toolkit 2019). The code that is intended to read the *X* coordinate value in a given line of the GCODE file has the following form:

```
!if the line in the GCODE file begins from G0 or G1:
if((index(line,'G0')/=0).or.(index(line,'G1')/=0))then
 !find position of X sign (0 means that this sign do not exists in this line):
posX=scan(line,'X')
 !if the X sign exists:
 if(posX>0)then
 !find the position of a space occurring after the X sign:
posNull=scan(line(PosX:),char(32))
 !save all signs from the X sign to a next space located in the same line:
lineX=line(posX:posX+posNull-1)
 !extract the numbers occurring after the sign X:
 write(tmp,fmt='(A)')lineX(2:)
 !assign the read out number to the current X coordinate:
 read(tmp,*)x(lp)
 !remember the last known value of the X coordinate:
xw=x(lp)
 !if the X sign do not exists:
 else
 !assign the previous value to the current X coordinate:
 x(lp)=xw
endif
endif
```

The meaning of variables is as follows: "line" – a character variable containing the current line of the GCODE file; "posX" – an integer variable containing the position of X sign in the variable "line"; "posNull" – an integer variable containing the position of a space in the variable "line" (here the space located after X sign); "lineX" – a character variable containing a substring of the variable "line" (here X sign together with numbers occurring after this sign); "lp" – counter of points in the model; "x(lp)" – a float variable containing the current value of the X coordinate; "xw" – a float variable containing the last remembered value of the *X* variable.

In addition to the three basic GCODE files, during the development of the algorithm, other variants of these files were also tested. The variants were obtained with different settings of the MatterControl program. Depending

on the settings, the movement of the print head can be described with instructions G0 or G1 (see Table 1). Another difference appears in the length and content of the GCODE file header or footer, in particular the method and location of the Z0 coordinate. The program has been written to take into account as many possible differences as possible.

In Figures 5*a*, 6*a* and 7*a* there are examples of visualization of subsequent positions of the print head obtained after decoding the selected GCODE files. Visualizations were made in the ParaView (ParaView Home Page 2019) with the use of the automatically generated VTK files. The overall shape of the object is visible, but some walls are clearly missing. This effect results from the fact that if the print head moves along a straight line (regardless of its length), only the coordinates of the beginning and end of this line are saved in the GCODE file. To improve the reproduction quality of the original geometry with a pointsset, it is preferable to insert intermediate points. In the developed program, in relation to straight lines, this stage consists of the following steps:

– length calculation of the section between the current (i) and previous ($i-1$) location of the print head:

$$l = \sqrt{(x_i - x_{i-1})^2 + (y_i - y_{i-1})^2 + (z_i - z_{i-1})^2};$$

– calculation of the number of intermediate points:

$$n_l = \mathrm{NINT}\left(\frac{l}{dl}\right),$$

where *dl* is the maximum spatial step defined by the user;

– calculation of increments of individual coordinates:

$$dx = \frac{x_i - x_{i-1}}{n_l}, dy = \frac{y_i - y_{i-1}}{n_l}, dz = \frac{z_i - z_{i-1}}{n_l}.$$

In the last step the coordinates of intermediate points are calculated:

$$x_j = x_{i-1} \cdot j \cdot dx\,,\ y_j = y_{i-1} \cdot j \cdot dy,\ z_j = z_{i-1} \cdot j \cdot dz\,,$$

where *j* denotes the sequence number of the intermediate point, whereby $j \in \langle 1, n_l \rangle$.

Before preparing the output files, the data should be also checked for any duplicate points. If they are found, such points should be removed.

The disadvantage of inserting intermediate points is a significant increase in the number of points representing the geometry of the object. For $dl = 0.5$ the total number of points for the casing, gear and screw increased from 52,926 to 186,910, from 64,447 to 233,981 and from 11,151 to 12,776, respectively. This is 3.532, 2.127 and 1.146 times more points, respectively. This condition

can lead to difficulties in visualizing such a large points set. The effect deepens with the decrease of *dl*. It should be added that difficulties in visualizing large sets of points (a long waiting time for a program to response) occurred only in the ParaView software. The MeshLab program (MeshLab Home Page 2019), described later in the article, worked much faster.

In Figures 5*b*, 6*b*, 7*b* the final results are visible. They were prepared in the ParaView software with the use of the "glyph" tool. This tool allows to draw a simple 3D object (arrow, cone, box, cylinder, line, sphere) in every point with a specified location. In the figures mentioned, cubes (Fig. 5 and 6) and spheres (Fig. 7) were used to prepare the visualisation. In such a way a set of points may be visualized as a sets of solids. Such a result may be saved, among others, in the STL file format. Unfortunately, such a file consists of many separate objects (cubes and spheres) and cannot be applied directly in the same way as the original STL file. All tries of merging these objects into one surface or solid body failed.

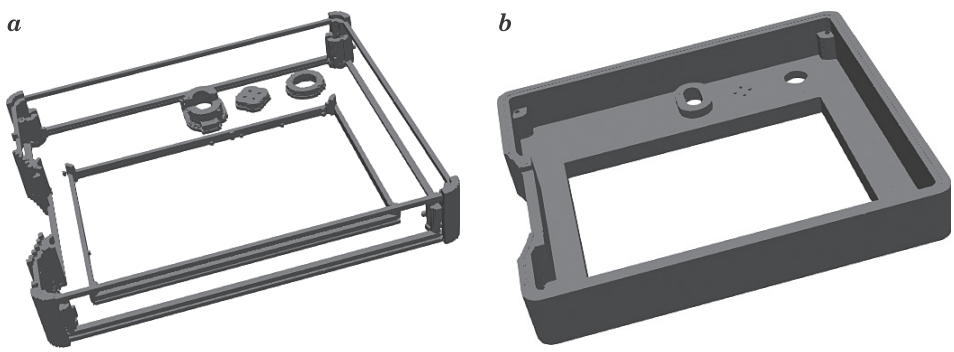

Fig. 5. Example of visualization of print head positions without interpolation (*a*) and with interpolation, at $d_l = 0.2$ (*b*)

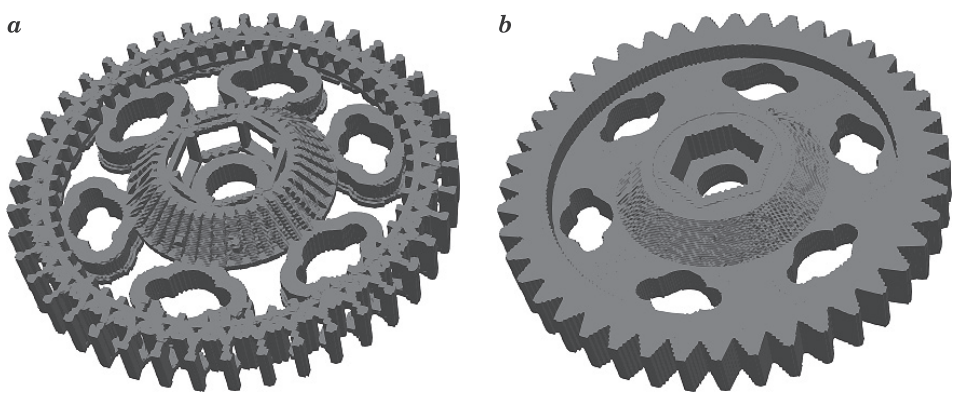

Fig. 6. Example of visualization of print head positions without interpolation (*a*) and with interpolation, at $d_l = 0.2$ (*b*)

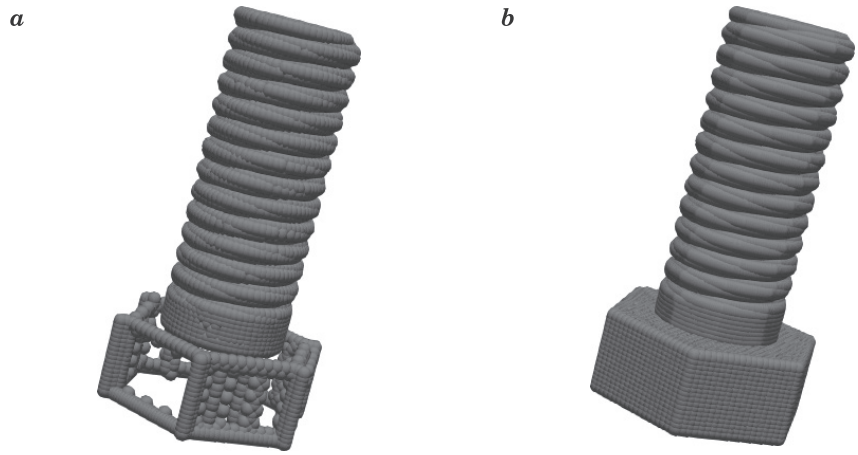

Fig.7. Example of visualization of print head positions without interpolation (*a*) and with interpolation, at $d_I = 0.5$ (*b*)

The results obtained from the extraction of geometry, in the version with interpolation of intermediate points, were also saved in the form of text files in the ASC format. This format consists of only three columns of numbers, containing the *X*, *Y* and *Z* coordinates of all the points of the set.

Poisson Surface Reconstruction

The previously mentioned MeshLab (MeshLab Home Page 2019) application was used to carry out the next stage of work. The choice of this particular application was dictated by the fact that it allows to load data in many different file formats, among others in the ACS format. What is more, the program can be used, for instance, to perform the earlier mentioned Poisson Surface Reconstruction.

In the case of dense points sets, such as those obtained in the previous stage, the local number of points should be reduced. It may be done by selecting an appropriate tool from the main menu: "Filters – Cleaning and Repairing – Merge Close Vertices". Now the normal vectors to the surface in all points of the current set may be calculated by selecting the following from the main menu: "Filters – Normal, Curvatures and Orientation – Compute normals for points sets". The last step is to select the Poisson Surface Reconstruction tool from the main menu. This is done as follows: "Filters – Remeshing, Simplification and Reconstruction – Screened Poisson Surface Reconstruction". It should be added that few constants have to be defined while using these tools. The best results were obtained for the parameters that were listed in Table 3.

Table 3

Surface reconstruction parameters in the MeshLab program

MeshLab Filter			Casing	Gear	Screw
Cleaning and Repairing	Merge Close Vertices	perc on	150	100	180
Normal, Curvatures and Orientation	Compute normals for points sets	Neighbour num	10	10	50
		Smooth Iteration	0	0	0
Remeshing, Simplification and Reconstruction	Screened Poisson Surface Reconstruction	Reconstruction Deepth	10	8	8
		Minimum Number of Samples	10	4	3
		Integration Weight	4	10	6

In Figure 8*a* there is the starting points set for the casing model, and to the Figure 8*b* the reconstructed 3D object is visible. Unfortunately, despite many attempts, it was not possible to reconstruct the surface in such a way that it would accurately represent the output objects. In particular, it was not possible to obtain STL files that could be later modified and reused in the printing process. Figures 9 and 10 show the reconstruction of the gear model and screw.

It is clearly visible, that the geometry visible in Figures 8, 9 and 10 do not correspond with the original 3D models (Fig. 2). It means, that the Poisson Surface Reconstruction is not a good method to obtain a file, which may be again used as the input file in printing process. The investigation should focus rather on the problem described in the previous section, consisting of merging many separate objects into one surface or solid body.

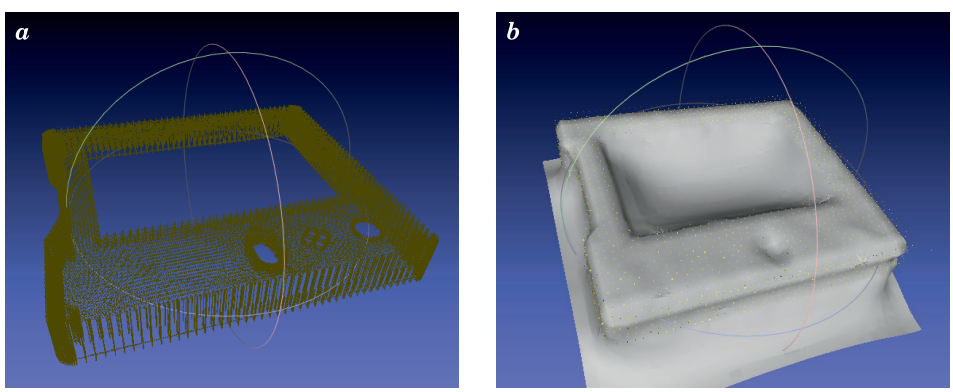

Fig. 8. Casingmodel; *a* – pointsset, *b* – reconstructed model

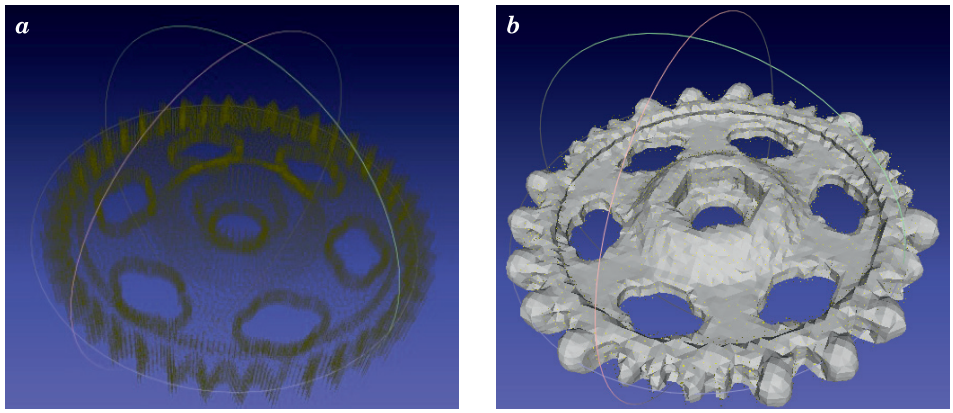

Fig. 9. Model of the gear in the form of the starting pointsset (*a*) and the reconstructed area (*b*)

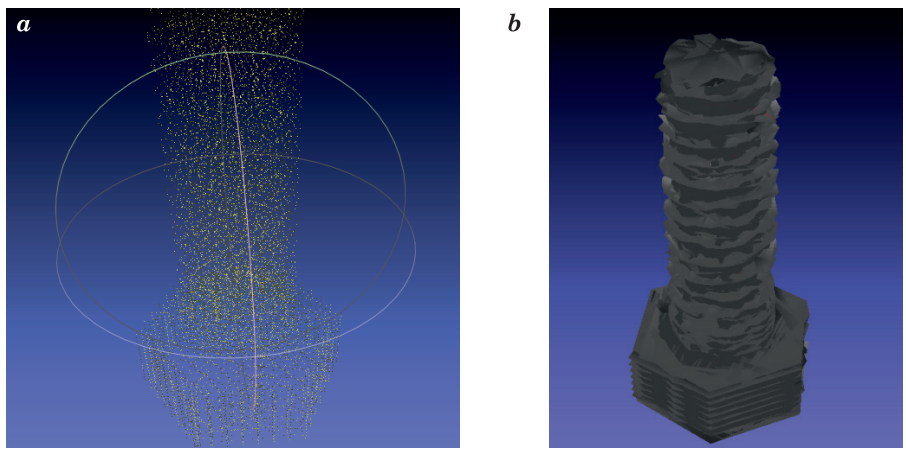

Fig. 10. Screw model; *a* – pointsset, *b* – reconstructed model

Summary

The main observations and final conclusions are as follows:

– It is possible to transform a geometry saved in a GCODE file to a points set. In turn, this points set may be visualised (and saved in the STL file format) by the use of appropriate software, e.g. ParaView.

– The movement of the print head must be interpolated to reconstruct filled structures.

– Duplicates of points in points sets should be detected and removed.

– The decoding process is hindered by the fact that from one geometry many differing GCODE files may be obtained (it depends on settings of the algorithm

converting the STL files to the GCODE files). This problem sometimes results in the situation when the points appear outside the original geometry. It is difficult to develop a universal algorithm to filter such points which could be applied to all possible variants of GCODE files.

– The quality of the reconstructed surface depends on the parameters introduced in the MeshLab program. There are no universal parameters that reproduce all models in the same way (each model has a different geometry and needs different parameters).

– On the current stage the algorithm described may be used only to view the geometry saved in a GCODE file. The main advantage is, that the source code of the developed software is very short and concise and may be easy modify. No access to the Internet is needed, too.

– Resulting files with coordinates of points belonging to a point cloud are usually very large in volume (in the order few hundred of MB). It causes that many software crashes during manipulation with such a files. This problem do not occurs in the developed software.

References

Baronio G., Harran S., Signoroni A. 2016. *A Critical Analysis of a Hand Orthosis Reverse Engineering and 3D Printing Process*. Applied Bionics and Biomechanics, 2016: 1-7, article ID 8347478.

Baumann F., Bugdayci H., Grunert J., Keller F., Roller D. 2016. *Influence of slicing tools on quality of 3D printed parts*. Computer-Aided Design & Applications, 13(1): 14-31.

Baumann F.W., Schuermann M., Odefey U., Pfeil M. 2017. *From GCODE to STL: Reconstruct Models from 3D Printing as a Service*. IOP Conf. Series: Materials Science and Engineering, 280: 012033.

Dúbravčík M., Kender Š. 2012. *Application of reverse engineering techniques in mechanics system services*. Procedia Engineering, 48: 96-104.

Eslami A.M. 2017. *Integrating Reverse Engineering and 3D Printing for the Manufacturing Process*. American Society for Engineering Education, Paper ID #18869.

GNU Fortran Home Page. 2018. https://gcc.gnu.org/fortran/ (access: 18.10.2018).

Godoi F.C., Prakash S., Bhandari B.R. 2016. *3D printing technologies applied for food design: Status and prospects*. Journal of Food Engineering, 179: 44-54.

Guerrero-de-Miera A., Espinosa M.M., Domínguez M. 2015. *Bricking: A new slicing method to reduce warping*. Procedia Engineering, 132: 126-131.

Habrat W. 2007. *Obsługa i programowanie obrabiarek CNC. Poradnik operatora*. Wydawnictwo KaBe, Krosno.

Hangge P., Pershad Y., Witting A.A., Albadawi H., Oklu R. 2018. *Three-dimensional (3D) printing and its applications for aortic diseases*. Cardiovascular Diagnosis and Therapy, 8: 19-25.

Hu J. 2017. *Study on STL-Based Slicing Process for 3d Printing*. Proceedings of the 28th Annual International, Solid Freeform Fabrication Symposium – An Additive Manufacturing Conference. Austin TX, August 7-9, 11 p.

ISO 6983-1:2009: Automation systems and integration – Numerical control of machines -- Program format and definitions of address words – Part 1: Data format for positioning, line motion and contouring control systems. https://www.iso.org/standard/34608.html (access: 18.10.2018).

jView. 2020. http://www.jtronics.de/software/jview-simple-g-code-viewer/ (access: 1.04.2020).
KAZHDAN M., BOLITHO M., HOPPE H. 2006. *Poisson surface reconstruction*. Proceedings of the 4th Eurographics Symposium on Geometry Processing, Sardinia, Italy, p. 1-10.
KRAMER T.R., PROCTOR F.M., MESSINA E. 2000. *The NIST RS274NGC Interpreter – Version 3*. NISTIR 6556, August 17, p. 121.
LORENSEN W.E., CLINE H.E. 1987. *Marching cubes: a high resolution 3D surface construction algorithm*. ACM SIGGRAPH Computer Graphics, 21(4): 163-169.
MATHUR R. 2016. *3D Printing in Architecture*. International Journal of Innovative Science, Engineering & Technology, 3(7): 583-591.
MatterControl Home Page. 2019. https://www.matterhackers.com/ (access: 10.04.2019).
MeshLab Home Page. 2019. http://www.meshlab.net/ (access: 10.04.2019).
NC Viewer. 2020. https://ncviewer.com/ (access: 11.04.2020).
NORLANDER R. 2017. *Make it Complete: Surface Reconstruction Aided by Geometric Primitives*. http://liu.diva-portal.org/smash/get/diva2:1153573/FULLTEXT01.pdf.
ParaView Home Page. 2019. https://www.paraview.org/ (access: 10.04.2019).
PARRA-CABRERA C., ACHILLE C., KUHN S., AMELOOT R. 2018. *3D printing in chemical engineering and catalytic technology: structured catalysts, mixers and reactors*. Chemical Society Reviews, 1.
PITAYACHAVAL P., SANKLONG N., THONGRAK A. 2018. *A Review of 3D Food Printing Technology*. MATEC Web of Conferences, 213: 01012.
SHAHI B.S. 2016. *Advanced Manufacturing Techniques (3D Printing)*. International Journal of Mechanical And Production Engineering, 4(4): 16-23.
SHATORNAYA A.M., CHISLOVA M.M., DROZDETSKAYA M.A., PTUHINA I.S. 2017. *Efficiency of 3D printers in Civil Engineering*. Construction of Unique Buildings and Structures, 9(60): 22-30.
SZEBÉNYI G., CZIGÁNY T., MAGYAR B., KARGER-KOCSIS J. 2017. *3D printing-assisted interphase engineering of polymer composites: Concept and feasibility*. eXPRESS Polymer Letters, 11(7): 525-530.
TAPPA K, JAMMALAMADAKA U., BALLARD D.H., BRUNO T, ISRAEL M.R., VEMULA H., MEACHAM J.M., MILLS D.K., WOODARD P.K., WEISMAN J.A. 2017. *Medication eluting devices for the field of OBGYN (MEDOBGYN): 3D printed biodegradable hormone eluting constructs, a proof of concept study*. PLoSONE, 12(8): e0182929.
TAY Y.W.D., PANDA B., PAUL S.C., MOHAMED N.A.N., TAN M.J., LEONG K.F. 2017. *3D printing trends in building and construction industry: a review*. Virtual and Physical Prototyping, 12(3), 261-176.
TOPÇU O., TAŞCIOĞLU Y., ÜNVER H.Ö. 2011. *A Method for Slicing CAD Models in Binary STL Format*. 6th International Advanced Technologies Symposium (IATS'11), 16-18 May 2011, Elazığ, Turkey.
VTK – The Visualization Toolkit. https://www.vtk.org/ (access: 10.04.2019).
WANG W., CHAO H., TONG J., YANG Z., TONG X., LI H., LIU X., LIUY L. 2014. *Saliency-Preserving Slicing Optimization for Effective 3D Printing*. COMPUTER GRAPHICS forum, 33(5): 1-12.
XU Y., WU X., GUO X., KONG B., ZHANG M., QIAN X., MI S., SUN W. 2016. *The Boom in 3D-Printed Sensor Technology*. Sensors, 17: 37.

Technical Sciences, 2020, 23(2), 131–142

UNIWERSYTET WARMIŃSKO-MAZURSKI W OLSZTYNIE

Quarterly peer-reviewed scientific journal
ISSN 1505-4675
e-ISSN 2083-4527
TECHNICAL SCIENCES
Homepage: www.uwm.edu.pl/techsci/

DOI: https://doi.org/10.31648/ts.5394

AN ANALYSIS OF A CYLINDRICAL CYCLONE SEPARATOR USED IN AIRCRAFT TURBINE ENGINES

***Tomasz Szwarc*[1], *Włodzimierz Wróblewski*[2], *Tomasz Borzęcki*[3]**

[1] ORCID: 0000-0002-0391-3353
Avio Polska sp. z o.o.
Bielsko-Biała

[2]ORCID: 0000-0002-3617-3515
Department of Power Engineering and Turbomachinery
Silesian University of Technology

[3] ORCID: 0000-0002-4226-7921
Avio Polska sp. z o.o.
Bielsko-Biała

Received 5 April 2020, accepted 2 July 2020, available online 7 July 2020.

K e y w o r d s: Multi-phase flows, air-oil separator, gas turbine, cyclone, volume of fluid method.

A b s t r a c t

Cyclone separators are commonly used in the oil system of aircraft gas turbine engines to separate air from oil. The major advantages of cyclone separators are simple structure and high reliability that eliminate the need for frequent inspections. The efficiency of a cyclone separator has a decisive impact on oil quality, which directly affects the efficiency of the oil system. The new generation of engines requires more compact separator designs to reduce weight and minimize project costs while maintaining (and often increasing) an engine's efficiency and reliability. To meet these requirements and optimize the separator structure, the flow of the air-oil mixture has to be modeled in the design process. The aim of this study was to present a numerical simulation of an aircraft turbine separator with the use of the volume of the fluid model.

Correspondence: Tomasz Szwarc, Avio Polska sp. z o. o. ul. Grażyńskiego 141, 43-300 Bielsko-Biała, e-mail: tomasz.szwarc@avioaero.it

Introduction

A cyclone separator is a component installed inside the main engine oil tank (Fig. 1). The major advantage of a cyclone separator is its simple structure which does not require maintenance or frequent inspections. A cyclone separator separates air from oil. The air-oil mixture is generated during the lubrication process inside engines, bearings, sumps and gearbox cavities. A separator's efficiency has a decisive impact on oil quality, and it directly affects the efficiency of the oil system. Increased air content in oil decreases pressure in the system and induces higher-pressure fluctuations, which in turn affects improper lubrication and cooling of engine components (bearings, gears, splines, accessories). Aircraft cyclone separators have to meet many more requirements than typical industrial cyclone separators. Varied operating conditions during flight missions cause changes in parameters such as the air/oil ratio, oil tank level, pressure, attitude and position. High swirling flow inside the separator is frequently encountered, and it is not stable. Unstable distribution of the flow field determines separation performance.

This paper analyzes a numerical model of an air-oil separator under a single operating condition. The flow field in the separator is complex, and swirling and anisotropy phenomena are sometimes taken into consideration in the relevant analyses. According to some authors (CHANG 2016, DELGADILLO 2005, ESCUE 2010, GAO 2012, RUDOLF 2013, WANG 2015), the Reynolds Stress Model (RSM) or the Large Eddy Simulation (LES) technique should be applied, but these advanced models are not suitable for developing optimization algorithms in future investigations. The above models are time-consuming and quite challenging in terms of the required calculation hardware. In the industrial approach, two equation models are more commonly used (SZWARC 2019). The RNG k-ε model with a swirling option was applied in this study. The model can recreate the flow characteristics of a cyclone separator, which can be useful for designing and optimizing this engine component (WANG 2010). The impact of different turbulence models on the solution will be studied in the future. In the presented preliminary analysis, turbulence was modeled with the two equation RNG k-ε model that speeds up calculations (WANG 2010) (two equations vs. seven equations in the RSM). Two-phase flow was simulated with the volume of the fluid model. This model accounts for the free surface effect (HIRT 1981) in the oil tank, which also considerably influences the separator's performance (KRISTOFFERSEN 2017). Gas-liquid separators (e.g. ARPANDI 1996, ERDAL 1998, KRISTOFFERSEN 2017) and other aircraft engineering applications (e.g. EASTWICK 2006, FILIPPONE 2010) have been widely studied and discussed, but there is a general scarcity of research into cyclone separators in an aircraft engine oil system. The typical cases reported in the literature involve cyclone separators for the oil and gas industry which have a different geometry or air/oil ratio and are difficult

to compare with aircraft applications. Other publications describe cyclone separators with a similar geometry to that analyzed in this paper (CHANG 2016, RUDOLF 2013), but those devices are used in the mineral industry with different fluid types or fluid and solid mixtures.

The aim of this study was to analyze a numerical model of two-phase fluid flow. The main goal was to develop a numerical model for implementation in the optimization procedure. The results were used to formulate recommendations for designers of air-oil separators.

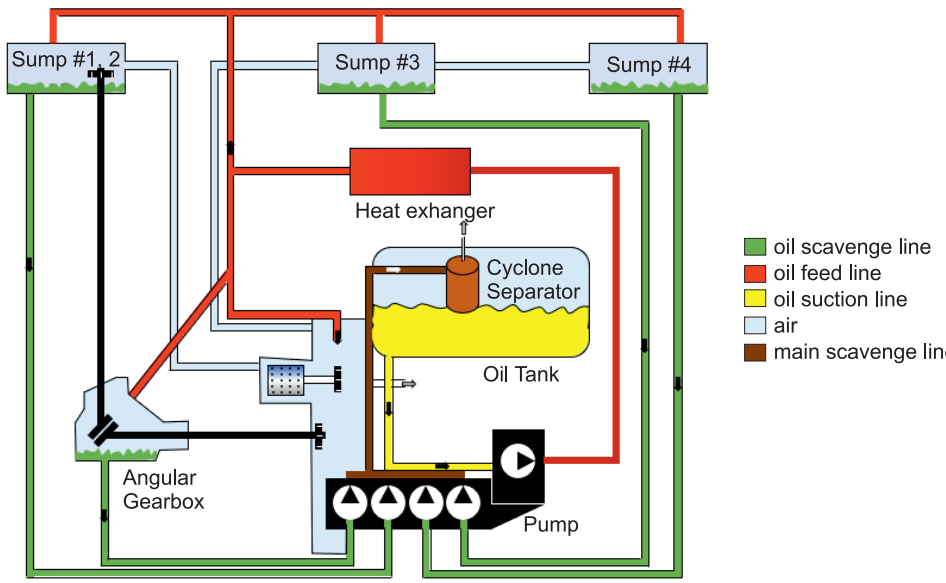

Fig. 1. Simplified scheme of an aircraft oil system

Oil lubricates and cools the components of a gas turbine engine, including bearings, gears, spline joints and dynamic seals. In the lubrication process, oil is aerated in sumps and gearboxes. The force of gravity drives oil to the lower parts of the engine where it is taken up by the scavenge pump and directed to the oil tank. The efficiency of the oil separator has a decisive impact on oil quality. A decrease in its parameters affects the operation of lubrication and cooling circuits. The optimal two-phase model has to be selected in analyses of computational fluid dynamics (CFD). The choice of the appropriate mathematical model depends on the type of flow at the separator inlet. This is a crucial requirement for simulating separation processes. A preliminary selection can be made based on two-phase flow maps (SZWARC 2019).

Numerical model

Geometry and boundary conditions

The geometry of the calculation domain was created based on the geometry of the test bench where a separator was installed in a cylindrical tank shown in Figure 2. The air-oil mixture flowed into the tank tangentially, and a swirl was generated inside the separator. Oil was directed towards the walls, and it flowed down into the tank. The separator had two outlets: one in the upper part and one at the bottom. Air was extracted from the separator through the upper outlet, and the presumably clear oil flowed through the bottom outlet. At the inlet, the mass flow rates of both air and oil were applied as boundary conditions. Uniform velocity with normal direction to the inflow cross-section was assumed. The mixture had constant temperature. Pressure conditions were specified at the outlets.

The experimental data were used to develop the simulation model. The test bench supports measurements of the inlet mass flow rate of each fraction at the inlet and the outlet, whereas pressure and temperature are measured only at selected points. Oil quality defined by Equation 1 was measured at the outlet

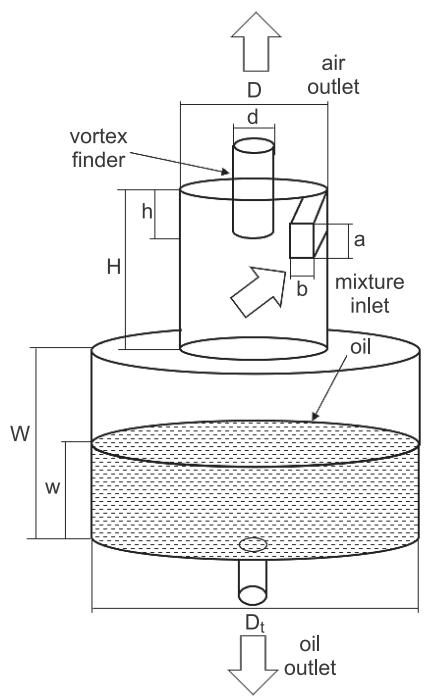

Fig. 2. A separator with the test tank

line by checking the volume fraction of each phase. Standard aviation oil for gas turbine engines was applied in the simulations. The volumetric air/oil ratio was 1.3 at the inlet. Numerical schemes for the analysis were selected based on the results reported by (WANG 2015). A coupled scheme with a pseudo transient option was selected as the solution algorithm for pressure-velocity coupling. For the preliminary numerical analysis, first-order upwind schemes were set for turbulent kinematic energy and the dissipation rate.

The boundary conditions at the outlets which enabled the determination of the prevailing conditions in the test stand were identified. The aim of the calculations was to determine separator performance which was described by two coefficients. The first coefficient denoted the amount of gas flowing through the oil outlet, whereas the second coefficient indicated the amount of oil flowing through the air outlet. These values were measured during the experiment. The oil quality coefficient (OQ) was defined as the volume fraction of oil at the oil outlet:

$$OQ = \left(\frac{\dot{V}_o}{\dot{V}_a + \dot{V}_o}\right)_{\text{oil outlet}} \tag{1}$$

Separation efficiency η_s was defined as the ratio of the difference between the volume rate of oil at the inlet and the volume flow rate at the outlet to the volume rate of oil at the inlet:

$$\eta_s = \frac{\dot{V}_{\text{o,inlet}} - \dot{V}_{\text{o,vent}}}{\dot{V}_{\text{o,inlet}}} \tag{2}$$

The determination of the optimal boundary conditions is a major challenge in the simulation process. Since air and oil masses were measured and mixed before entering the separator, the mass flow rate with a homogeneous distribution of the second phase was selected.

Pressure values were determined at both oil and air outlets. These boundary conditions are set to control the separation process. Other possible types of boundary conditions which are based on mass flow could not be applied at the outlets because the mass flow rates should be determined in a computational analysis. The dimensions of the test bench are presented in the Table 1.

Table 1

Dimensions of a cyclone with a tangential inlet

Dimensions	Cyclone height (H)	Vortex finder height (h)	Cyclone diameter (D)	Vortex finder diameter (d)	Inlet tube height (a)	Inlet tube width (b)	Tank height (W)	Tank diam. (D_t)
Parameter value (a)	3.2	1.4	3.6	1.3	1	1.6	12	3

Mathematical model of two-phase flow

The separation phenomena in an air-oil mixture are simulated with the Volume of the Fluid (*VoF*) model. This model supports tracking of the air-oil interface. The *VoF* is used to model the flow of two immiscible fluids. The following continuity equation is solved:

$$\frac{\partial}{\partial t}(\rho) + \nabla \cdot (\rho \vec{v}) = 0 \tag{3}$$

where:

$\vec{v}$ – the velocity vector,

ρ – the mixture density calculated from:

$$\rho = \alpha_a \rho_a + (1 - \alpha_a)\rho_o \tag{4}$$

where:

ρ_a – air density,

ρ_o – is oil density,

α_a – is the volume fraction of air which, in this case, represents the second phase.

The interface between the phases is tracked with a continuity equation for the volume fraction of air:

$$\frac{\partial}{\partial t}(\alpha_a \rho_a) + \nabla \cdot (\alpha_a \rho_a \vec{v}_a) = \dot{m}_{oa} - \dot{m}_{ao} \tag{5}$$

where:

$\dot{m}_{oa}$, $\dot{m}_{ao}$ are the mass flow rates from oil to air and air to oil, respectively.

The volume fraction equation is not solved for the oil phase (primary). The oil-phase volume fraction is computed based on the following constraint:

$$\alpha_a + \alpha_o = 1 \tag{6}$$

In this case, the volume fraction equation is solved with an implicit formula. A single momentum equation is solved for the entire domain, and the resulting velocity field is shared by the phases. The momentum equation 7 is dependent on the volume fractions of all phases, including mixture density ρ and mixture viscosity μ (UBBINK 1997):

$$\frac{\partial}{\partial t}(\rho \vec{v}) + \nabla \cdot (\rho \vec{v} \vec{v}) = -\nabla p + \nabla \cdot \left[\mu_{eff}(\nabla \vec{v} + \nabla \vec{v}^T)\right] + \rho \vec{g} + \vec{F} \tag{7}$$

where:

$\mu_{eff} = \mu + \mu_t$ – dynamic effective viscosity,

$\vec{g}$ – gravitational acceleration,

p – pressure,

$\vec{F}$ – the surface tension source term.

Turbulence

The RNG k–ε model is derived from the instantaneous Navier–Stokes equations using a mathematical technique known as "renormalization group" (RNG) methods. This technique is based on the standard k-ε model with some refinements. An additional term in the ε equation improves accuracy for rapidly strained flows. As a result, the effect of swirl on turbulence is taken into account, which improves the accuracy of swirling flows. The RNG theory provides an analytical formula for turbulent Prandtl numbers, whereas the standard k-ε model uses user-specified, constant values (YAKHOT 1986).

The following equations for turbulence kinetic energy k and dissipation rate of turbulent kinetic energy are solved:

$$\frac{\partial}{\partial t}(\rho k) + \frac{\partial}{\partial x_i}(\rho k U_i) = \frac{\partial}{\partial x_j}\left(\alpha_k \mu_t \frac{\partial k}{\partial x_j}\right) + G_k + G_b - \rho\varepsilon - Y_M + S_k \tag{8}$$

$$\frac{\partial}{\partial t}(\rho \varepsilon) + \frac{\partial}{\partial x_i}(\rho \varepsilon U_i) = \frac{\partial}{\partial x_j}\left(\alpha_\varepsilon \mu_t \frac{\partial \varepsilon}{\partial x_j}\right) + C_{1\varepsilon}\frac{\varepsilon}{k}G_k - C_{2\varepsilon}\rho\frac{\varepsilon^2}{k} - R_\varepsilon \tag{9}$$

where:

α_k and α_ε – the inverse effective Prandtl numbers for k and ε,

$C_{1\varepsilon}$ and $C_{2\varepsilon}$ – constant values of 1.42 and 1.68.

The scale elimination procedure in the RNG theory produces a differential equation for turbulent viscosity. Effective viscosity μ_t for the limit of very large Reynolds numbers is given by:

$$\mu_t = \rho C_\mu \frac{k^2}{\varepsilon} \tag{10}$$

where the value of C_μ = 0.0837 is derived with the RNG theory. Interestingly, the value of C_μ = is very close to the empirically determined value of 0.09 in the standard k-ε model (YAKHOT 1986).

Mesh

Separator geometry was divided into a tetra mesh generated with the Ansys Workbench tool 19.2. 3D geometry was meshed using a different number of elements, ranging from 512,000 to 1,527,000 tetra cells. The mesh was refined mainly in the regions close to the wall, and a moderate refinement was introduced in the central part of the separator domain. The quality of all 3D computational meshes with a different number of elements was checked before the simulation (see Tab. 2). Figures 3 and 4 show selected mesh overview.

Table 2

Mesh quality

Key factor	Requirement	Mean mesh quality
Aspect ratio	5:1	5.34
Orthogonal quality	>0.01 (best cell closer to 1)	0.96
Skew	below 0.95	0.82

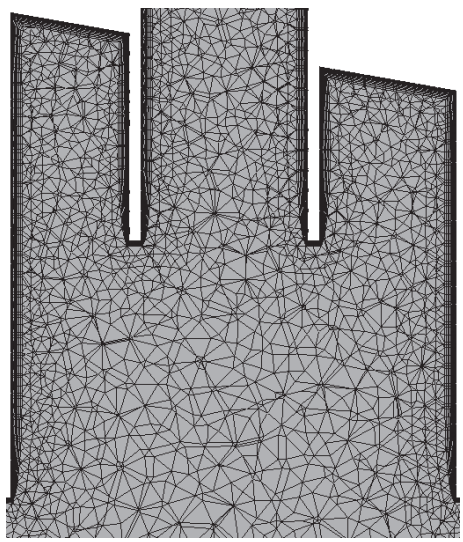

Fig. 3. Mesh at the cross-section of the separator

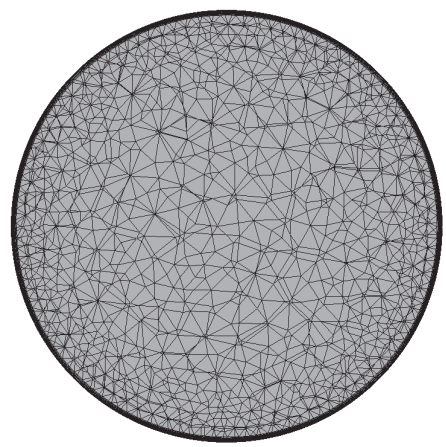

Fig. 4. Mesh at the bottom outlet of the separator

An analysis of the results of the first coarse mesh revealed satisfactory *OQ* values, but very low stability of the solution. A mesh independence analysis was performed to determine the impact of the size of the numerical grid. Two parameters were considered to guarantee the stability of the analysis: air and oil mass imbalance. An imbalance is defined as the sum of mass flows (inlet mass flow – outlet mass flows). The amplitude of the air mass flow rate at the outlet, oil quality and oil volume in the domain were selected to determine the influence of the mesh on the analyzed parameters. The results are presented in Figure 5. An increase in mesh density did not exert a significant influence on oil quality (the maximum difference was 13%). The oil level inside the domain remained stable. An improvement was observed in the parameters related to the stability of analysis. Considering *OQ* as the only goal of analysis, the mesh independence analysis demonstrated that changes in mesh refinement were relatively small. Lower density would significantly contribute to the optimization process.

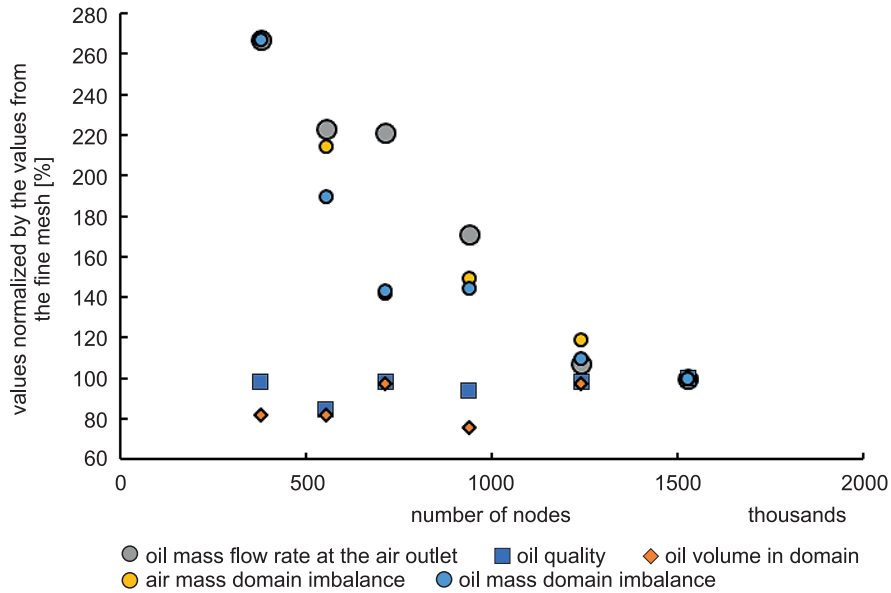

Fig. 5. Normalized solution parameters vs. the number of nodes

When the appropriate mesh type and density have been selected, the separator's geometry is optimized in the next step. Therefore, the selected mesh with 124k tetra cells guarantees the acceptable accuracy of the results and reasonable calculation time. This is an important consideration because a single case takes 1-2 weeks to compute with a computer cluster.

Calculation results

The aim of this study was to propose a numerical approach to an analysis of a cyclone separator. Oil was the primary phase, and air was the secondary phase. The analytical process became complicated already at the stage of formulating the initial conditions. The definition of initial values was a very important step in the calculations. Incorrect initial values lead to convergence problems or solver crash. Incorrect inlet pressure creates reverse flow at both outlets, which affects solver convergence and leads to mass imbalance problems. Inlet pressure was set based on the experimentally determined pressure drop in the separator. The preliminary simulation involved a very coarse mesh to determine the optimal working conditions. The analysis was initialized with an empty tank which was filled until the achievement of a stable oil level. The solver crashed when the simulation was initialized with a filled tank (Figs. 6, 7, 8, 9).

The location of the free surface in the oil tank is very sensitive to boundary conditions. This is an important factor which directly affects the formation of flow structures in the separator and, consequently, the separator's efficiency as predicted by (KRISTOFFERSEN 2017). This is a characteristic feature of open separators where the shape of the tank and oil level can impact performance. The main flow swirl in the cylinder causes oil separation, and oil is deposited on the separator wall. The main flow consisted of two phases. In the first phase, flow was parallel to the separator outlet, and in the second phase, flow occurred down the cylinder, creating a helical shape of streamlines (7 and 9). First-phase flow led to the accumulation of oil in the top corner of the separator, which is unlikely to occur due to recirculation with the incoming mixture. The second oil stream entering the tank influenced the oil free-surface.

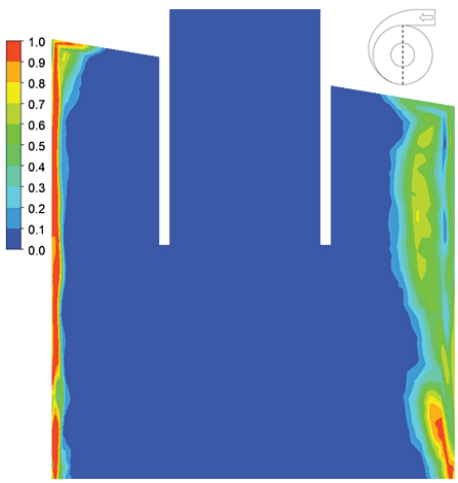

Fig. 6. Contour of the oil volume faction

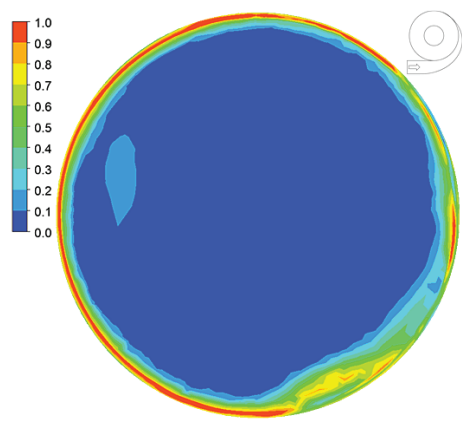

Fig. 7. Contour of the oil volume faction (bottom outlet of the separator)

The formation of oil film on the left wall is visible in Figure 6. The geometry of the inlet to the separation zone has a key impact on separation phenomena because it can rupture the formed film (Fig. 7). The axis of the vortex finder tube is not coincident with the outer diameter of the separator, which affects the formation of the inner swirl that flows directly to the vortex finder tube. The influence of the key geometrical features on flow structure will be investigated in the future after the numerical model has been validated.

The velocity distributions in the separator are visualized in Figure 8 and 9. The presented values were normalized by the values of average velocity at the cyclone inlet. Areas of both very low speed in the center of the separator (0-0.3) and high speed close to the walls (3-3.3) were observed.

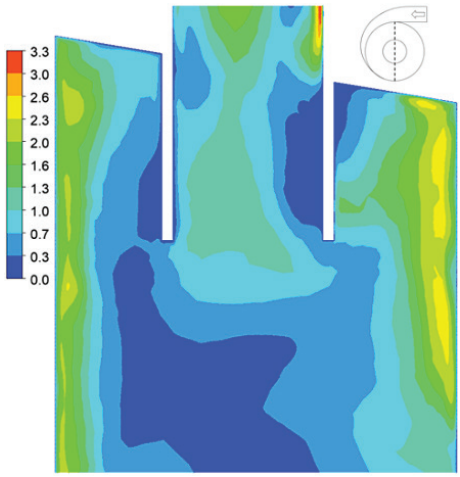

Fig. 8. Velocity contour

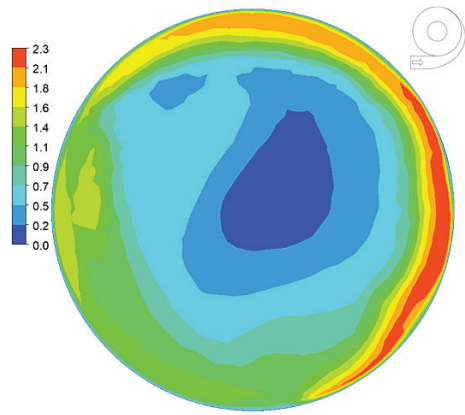

Fig. 9. Velocity contour(bottom outlet of the separator)

Table 3

Comparison of simulation results with test bench results

Parameter	Simulation results	Difference to test results
Normalized oil quality [%]	93.8	6.2
Normalized separation efficiency [%]	99.95	0.05

The experimentally determined values of oil quality OQ and separation efficiency η_s were compared with the results of numerical simulations. The difference in normalized oil quality reached 6.2% and in separation efficiency – 0.05% (Tab. 3). The resulting accuracy is satisfactory.

Conclusions

A cyclone separator was analyzed with the use of the presented calculation scheme. The *VoF* model was characterized by acceptable accuracy, and it offered a consensus between accuracy, robustness and modeling time. The selected boundary conditions stabilized oil volume inside the separator. The calculated pressure decrease was comparable with the experimentally determined pressure drop. The RNG k-ε model revealed a swirl structure inside the core of the separator. As expected, the results of the calculations indicate that oil level in the tank influences flow formation inside the separator. The separator inlet impacts the formation of the oil fraction close to the wall as well as its interaction with the free surface of the oil inside the tank. The observed changes in flow

parameters indicate that flow field was unsteady inside the separator. The above was confirmed by the mass flow rate of oil shown in Figure 5. Preliminary results demonstrated satisfactory alignment between the modeled results and the experimentally derived values. The results of the calculations for different experimental conditions will be analyzed in the future.

References

ARPANDI I., JOSHI A.R., SHOHAM O., SHIRAZI S., KOUBA G.E. 1996. *Hydrodynamics of two-phase flow in gas-liquid cylindrical cyclone separators*. Society of Petroleum Engineers, 1: 427–436, doi: 10.2118/30683-PA.

CHANG P., HU T., WANG L., CHANG S, WANG T., WANG Y. 2016. *Numerical simulation on structure optimization of liquid-gas cylindrical cyclone separator*. International Journal of Chemical Engineering, 3187631, doi: 10.1155/2016/3187631.

DELGADILLO J.A., RAJAMANI R.K. 2005. *A comparative study of three turbulence-closure models for the hydrocyclone problem*. International Journal of Mineral Processing, 77(1): 217–230, doi: 10.1016/j.minpro.2005.06.007.

EASTWICK C.N, SIMMONS K., WANG Y. 2006. *Study of aero-engine oil-air separators*. Journal of Power and Energy, 220(7): 707-717, doi.org/10.1243/09576509JPE116

ERDAL F.M., SHIRAZI S.A., MANTILLA I., SHOHAM O. 1998. *CFD Study of bubble carry-under in gas-liquid cylindrical cyclone separators*. Society of Petroleum Engineers, SPE-49309-M, doi: 10.2118/49309-MS.

ESCUE A., CUI J. 2010. *Comparison of turbulence models in simulating swirling pipe flows*. Applied Mathematical Modelling, 34(10): 2840–2849, doi: 10.1016/j.apm.2009.12.018.

FILIPPONE A., BOJDO N. 2010. *Turboshaft engine air particle separation*. Progress in Aerospace Sciences, 46(5-6): 224, 245, doi.org/10.1016/j.paerosci.2010.02.001.

GAO X., ZHAO Y., YANG X., CHANG Y., PENG X. 2012. *The research on the performance of oil-gas cyclone separators in oil injected compressor systems with considering the collision and breakup of oil droplets*. International Compressor Engineering Conference, p. 2119.

HIRT C.W., NICHOLS B.D. 1981. *Volume of Fluid (VOF) Method for the Dynamics of Free Boundaries*. Journal of Computational Physics, 39: 201–255, doi: 10.1016/0021-9991(81)90145-5.

KRISTOFFERSEN T., HOLDEN C., SKOGESTAD S., EGELAND O. 2017. *Control-Oriented Modelling of Gas-Liquid Cylindrical Cyclones*. American Control Conference, p. 2829–2836, doi: 10.23919/ACC.2017.7963380.

UBBINK O. 1997. *Numerical prediction of two fluid systems with sharp interfaces (Phd)*. Imperial College London, hdl.handle.net/10044/1/8604.

RUDOLF P. 2013. *Simulation of multiphase flow in hydrocyclone*. EPJ Web of Conferences, 45: 01101, doi: 10.1051/epjconf/20134501101.

SZWARC T., WRÓBLEWSKI W., BORZĘCKI T. 2019. *Numerical simulation of cyclone used in aircraft turbine engine*. Modelling in Engineering, 40: 74.

WANG J., MAO Y., LIU M. 2010. *Numerical simulation of strongly swirling flow in cyclone separator by using an advanced RNG k-ε model*. Shiyou Xuebao, Shiyou Jiagong/Acta Petrolei Sinica (Petroleum Processing Section), 26: 8-13.

WANG L., GAO X., FENG J.M., PENG X.Y. 2015. *Research on the two-phase flow and separation mechanism in the oil–gas cyclone separator*. IOP Conf. Series: Materials Science and Engineering, 90: 012075, doi: 10.1088/1757-899X/90/1/012075.

YAKHOT V., ORSZAG S.A. 1986. *Renormalization Group Analysis of Turbulence*. I. *Basic Theory*. Journal of Scientific Computing, 1(1), doi: 10.1007/BF01061452.

Technical Sciences, 2020, 23(2), 143–156

UNIWERSYTET WARMIŃSKO-MAZURSKI W OLSZTYNIE

Quarterly peer-reviewed scientific journal
ISSN 1505-4675
e-ISSN 2083-4527
TECHNICAL SCIENCES
Homepage: www.uwm.edu.pl/techsci/

DOI: https://doi.org/10.31648/ts.5881

A DESIGN CONCEPT OF A DEVICE FOR MEASURING AIR FLOW RESISTANCE IN VEHICLE FILTERS

Adrian Misztuk

ORCID: 0000-0001-6456-3716
Student at the Faculty of Technical Sciences
University of Warmia and Mazury in Olsztyn

Received 08 August 2020, accepted 15 September 2020, available online 30 September 2020.

K e y w o r d s: internal combustion engine, filter, impurities, air flow resistance.

A b s t r a c t

Internal combustion engines have to be supplied with adequate amounts of fuel and air. The required amount of fuel and air is determined by the engine controller to guarantee that the fuel reaching the cylinder is burned effectively and that the composition of exhaust gas meets standard requirements. The air supplied to an internal combustion engine has to be adequately filtered because impurities reaching the engine can accelerate the wear of engine components. The air intake system features a filtering partition which captures impurities and prevents them from reaching the engine. However, the filtering process decreases the rate at which cylinders are filled with fresh air, which can compromise engine performance. Therefore, effective solutions are needed to ensure that the flow of filtered air does not significantly decrease the volumetric efficiency of cylinders.

This study presents a design concept of a device for measuring pressure in the air intake system in front of and behind the filtering partition. The proposed device can be useful for measuring filter wear. A prototype of the proposed device was built and tested on several air filters. To eliminate throttle valve impacts, the device was tested in a compression ignition engine. The results of the conducted tests demonstrated that the device correctly measured air flow. The conducted measurements also revealed that the presence of impurities in the air filter induced differences in pressure in the air intake system in front of and behind the filtering partition. The maximum air flow resistance in a clogged filter could be even 100% higher than in a brand new filter.

Correspondence: Adrian Misztuk, Wydział Nauk Technicznych, Uniwersytet Warmińsko-Mazurski, ul. Michała Oczapowskiego 11, 10-719 Olsztyn, e-mail: misztuk96@gmail.com

Introduction

Internal combustion engines are immensely popular around the world, and they are used main to power motor vehicles and machines. Long engine life and reliability are very important parameters because they minimize repair and servicing costs. The operating fluids in a vehicle should be characterized by adequate purity to meet the requirements of both engine designers and users. Vehicle fluids are purified by filtration. Internal combustion engines are equipped with three basic types of filters: the air filter, the oil filter, and the fuel filter. Depending on their structural characteristics, engines can also be equipped with other types of filters.

The purity of the air drawn in by the engine significantly affects the engine's life, performance and operating parameters such as the maximum power and torque. The quality and purity of operating fluids, including fuel and engine oil, are not regulated by universal standards, which is why impurities should be effectively filtered out during vehicle operation. Air is contaminated with impurities of both anthropogenic (industry, fuel combustion in power plants) and natural origin (such as volcanic eruptions) (CHŁOPEK, JAKUBOWSKI 2009). The presence of hard particulate matter in air can lead to the gradual degradation and loss of engine components due to mechanical friction. Particles with a diameter equivalent to the thickness of lubricant oil film which is formed at the point of contact between engine components pose the greatest threat (DZIUBAK 2016). Atmospheric particulate matter is composed mainly of hard particles that are deposited between interacting surfaces inside the engine (CHŁOPEK, JAKUBOWSKI 2010, CHŁOPEK 2012, DZIUBAK 2003, 2006, DZIUBAK, BORCHET 2017). Other pollutants, including organic particulate matter, can also compromise engine performance.

Air-borne impurities have to be filtered out before they reach the engine. However, every filter adds resistance to the flow of air and decreases the rate at which cylinders are filled with air. Various air filtering solutions for internal combustion engines have been proposed over the years. The optimal solution should be characterized by high filtering efficiency, low air flow resistance and a long service life. Every filtering partition adds resistance to the air drawn in by the engine. The higher the generated resistance, the smaller the quantity of air reaching the engine's combustion chamber. Flow resistance is determined by the difference in air pressure in front of and behind the filter. The difference in air pressure on both sides of the filter can be measured to calculate flow resistance.

Types of air filters in internal combustion engines

The optimal air filter in an internal combustion engine should be characterized by high filtering efficiency (above 99%), the lowest possible air resistance, and a long service life. The filter should be reliable, small and light-weight (DZIUBAK,

SZWEDKOWICZ 2013). The flow resistance of an air filter directly influences the volumetric efficiency of cylinders.

According to Polish Standard PN-B-76004:1996, the dust for filter efficiency tests should have the following composition:

– 72% of Arizona desert sand (mostly silica) with an estimated density of 2.7 g/cm^3, where the majority of particles have a diameter of around 7.7 µm;

– 23% of soot;

– 5% of cotton linter.

Various air filters that differ in parameters and structure have been designed over the years. Mesh filters are composed of fine metal strips, metal rings or labyrinth strips enclosed by wire mesh. These filters have small dimensions, and they can be applied in motorcycles and low-power industrial engines (KORDZIŃSKI, ŚRODULSKI 1968). Another type of air filters are foam filters where air passes through a thin layer of liquid oil or thick oil foam. Foam filters are more efficient than mesh filters, but they are also characterized by higher flow resistance. Particulate matter is trapped in oil which has to be regularly replaced. Foam filters are large, and they are used mainly in heavy-duty machines. Dry filters containing absorbent paper are most popular. Machines that operate in a dusty environment are equipped with cyclone filters which are also known as centrifugal separation filters. Cyclone filters are characterized by low flow resistance. They can be coupled with dry paper filters and used as coarse filters in the first stage of the filtration process, which considerably prolongs the service life of the entire filtering system.

Dry air filters

In dry air filters, air flows through a porous filtering layer which constitutes a structural partition. Air-borne impurities are trapped by fine fibers of the filtering material. The cartridges in dry air filters consist of absorbent paper or heavy polyester felt. Woven fabric made of natural material or polyester is rarely used. Filter cartridges (Fig. 1) remove impurities from air without the involvement of liquids to facilitate the process. The temperature under the hood of a car can reach 120°C; therefore, air filters have to be flame retardant. Phenolic resins are sprayed on the surface of dry filter cartridges to offer additional protection against heat. Most dry air filters contain cellulose fibers impregnated with resin (HUTTEN 2016). The average density of a cellulose fiber filter ranges from 110 g/m^2 in light panel filters to 210 g/m^2 in two-layered composite filters. The engines of heavy-duty machines do not require highly efficient air filters, and filtering materials for this type of equipment are characterized by lower density in the range of 90-160 g/m^2.

Modern filtering fibers have a gradient structure, where the packing density of fibers increases in the direction of air flow (Fig. 2) (DZIUBAK, SZWEDKOWICZ 2014).

Fig. 1. Examples of dry paper filters

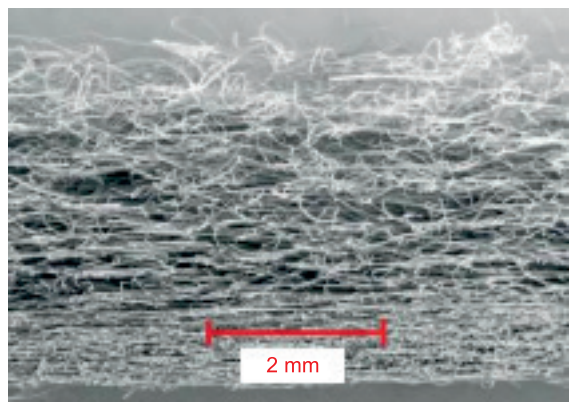

Fig. 2. Filtering material with a gradient structure and increasing fiber packing density
Source: based on DZIUBAK, SZWEDKOWICZ (2014).

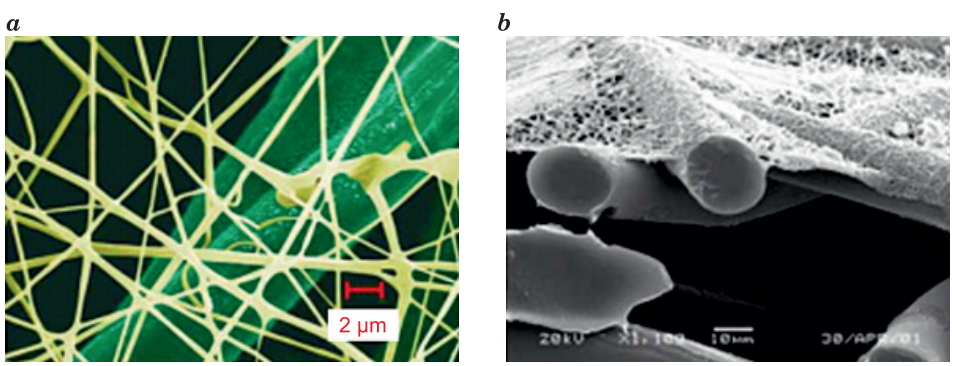

Fig. 3. Nanomesh layer applied to cellulose fibers: *a* – top view, *b* – cross-section. Nanofibers have a diameter of around 250 nm, and cellulose fibers have a diameter of around 10 µm
Source: based on DZIUBAK, SZWEDKOWICZ (2014).

Polymer nanofibers manufactured by the electrospinning technology are a novel filtrating medium. Electrospun fibers have a diameter of 1-2,000 nm. Nanofibers are formed in an nanomesh with a thickness of 1-5 μm. A nanomesh is composed of very densely packed fibers, and it can capture particles with a diameter of less than 5 μm; therefore, the generated flow resistance is minimal (DZIUBAK, SZWEDKOWICZ 2014). However, nanomeshes have very low mechanical resistance, and they cannot be applied independently as filtering materials. A thin nanomesh layer is applied to conventional filtering materials such as absorbent filter paper or filter fabric.

Cyclone filters

A cyclone filter relies on the principle of inertia to remove particulate matter from air. A cyclone filter does not contain a filtering partition or liquid to capture impurities. Air is fed into the centrifuge chamber where a spiral vortex is created. The force of inertia acts on dust particles which are thrown against the walls of the separating chamber. A cyclone filter which removes impurities through centrifugal separation is presented in Figure 4.

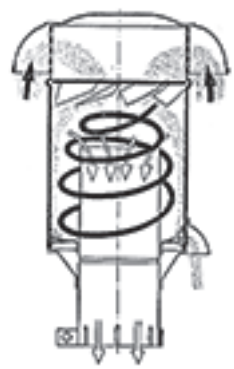

Fig. 4. A cyclone filter where impurities are removed through centrifugal separation. The direction of air flow is marked with arrows
Source: based on KORDZIŃSKI, ŚRODULSKI (1968).

Research objective

Air filters in internal combustion engines have to be regularly replaced. In some cases, the replaced filter is still fit for use, which generates additional and unnecessary costs. For environmental reasons, filters should be replaced only when they are clogged. Spent filters cannot be reused and they generate

additional waste, which has an adverse impact on the environment. An air filter should be replaced when air flow resistance exceeds the threshold value specified by the manufacturer. Air flow inside the filter and the degree of filter wear could be measured with a dedicated device to determine whether the cartridge should be replaced. Such a device could be used in automotive garages and repair shops to generate environmental benefits.

The aim of this study was to design and build a device for measuring air flow resistance in an engine air filter. The device measures air pressure in front of and behind the filter. The designed device was tested by measuring air flow resistance generated by various types of engine air filters.

Design assumptions for a device measuring air flow resistance in engine air filters

A dedicated device for measuring air flow resistance in an engine air filter was designed. Air flow resistance is determined by measuring the drop in air pressure on both sides of the filtering partition. Based on the adopted requirements, the proposed device should:

– consist of low-cost and widely available components,
– measure air pressure in front of and behind the air filter,
– be easy to use,
– be light-weight and portable,
– be compatible with various devices that generate air flow,
– operate without a power supply cable (powered by battery or PC via a USB port).

The designed device consists of a unit that measures the resistance of air flowing through the filtering partition and a unit that generates air flow. Air flow resistance was determined by measuring air pressure in front of and behind the filter. Air flow was generated by an internal combustion engine. The pressure in front of and behind the air filter was measured by sensors. A block diagram of the designed device is presented in Figure 5.

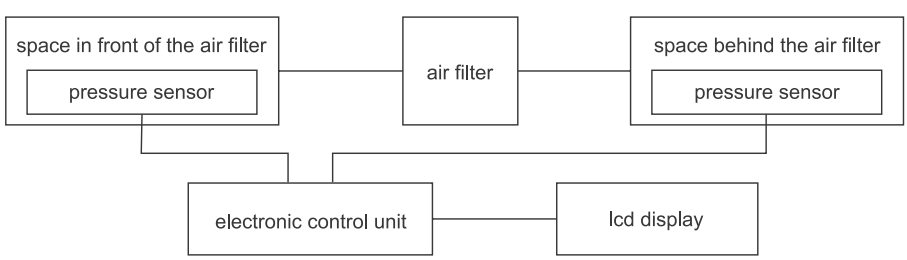

Fig. 5. Block diagram of the designed device for measuring air flow resistance generated by an engine air filter

The device was equipped with plastic housing where the tested air filter was mounted. Static pressure sensors were installed inside the rigid housing. The device was connected to an internal combustion engine via a PVC pipe with an internal diameter of 60 mm. The structure of the proposed device supported testing and rapid replacement of various air filters, both brand new and used. The shape of the tested filter had to be compatible with the assembly site to guarantee tight connections between the spaces in front of and behind the filtering partition. For the device to operate with various devices that induce air flow, the connecting pipes should have compatible diameters and the device has to be supplied with power, for example from a laptop. Air flow resistance generated by the tested filter was measured in the following steps:

– the device for measuring air flow resistance was connected to the device that generates air flow;
– the tested air filter was mounted in the housing;
– the measuring device was supplied with power;
– both devices were activated;
– air pressure was read from the LCD display.

Pressure values were recorded and used to calculate air flow resistance with the use of the following formula:

$$P - Z - R,$$

where:

P – pressure in front of the filtering partition,
Z – pressure behind the filtering partition,
R – pressure drop.

The device was equipped with the Arduino MEGA electronic control unit which is highly popular and widely available in retail. This controller has the required number of ports for connecting the device, and it is compatible with the applied pressure sensors. The Arduino MEGA controller communicated with pressure sensors and the LCD display via the I^2C interface with 4 pins: serial data line (SDL), serial clock line (SCL), positive power supply (VCC) and power ground (GND). Each device communicating with the I^2C bus should have a different address. The designed device was equipped with two pressure sensors with different addresses: BMP 180 with address 0×67, and BMP 280 with address 0×66. Two pressure sensors were used instead of a single differential pressure due to lower cost. When operated at a temperature of 0-65°C, sensor BMP 180 has a pressure measuring range of 950-1,050 hPa with an accuracy of ±1 hPa, and sensor BMP 280 has a pressure measuring range of 300-1,100 hPa with an accuracy of ±1 hPa (Bosch datasheet). Sensor BMP 180 has a sampling rate of up to 120 Hz, and sensor BMP 280 – up to 157 Hz. Sensor data were displayed on an LCD display with 4×20 characters. The circuit diagram of the designed device is presented in Figure 6.

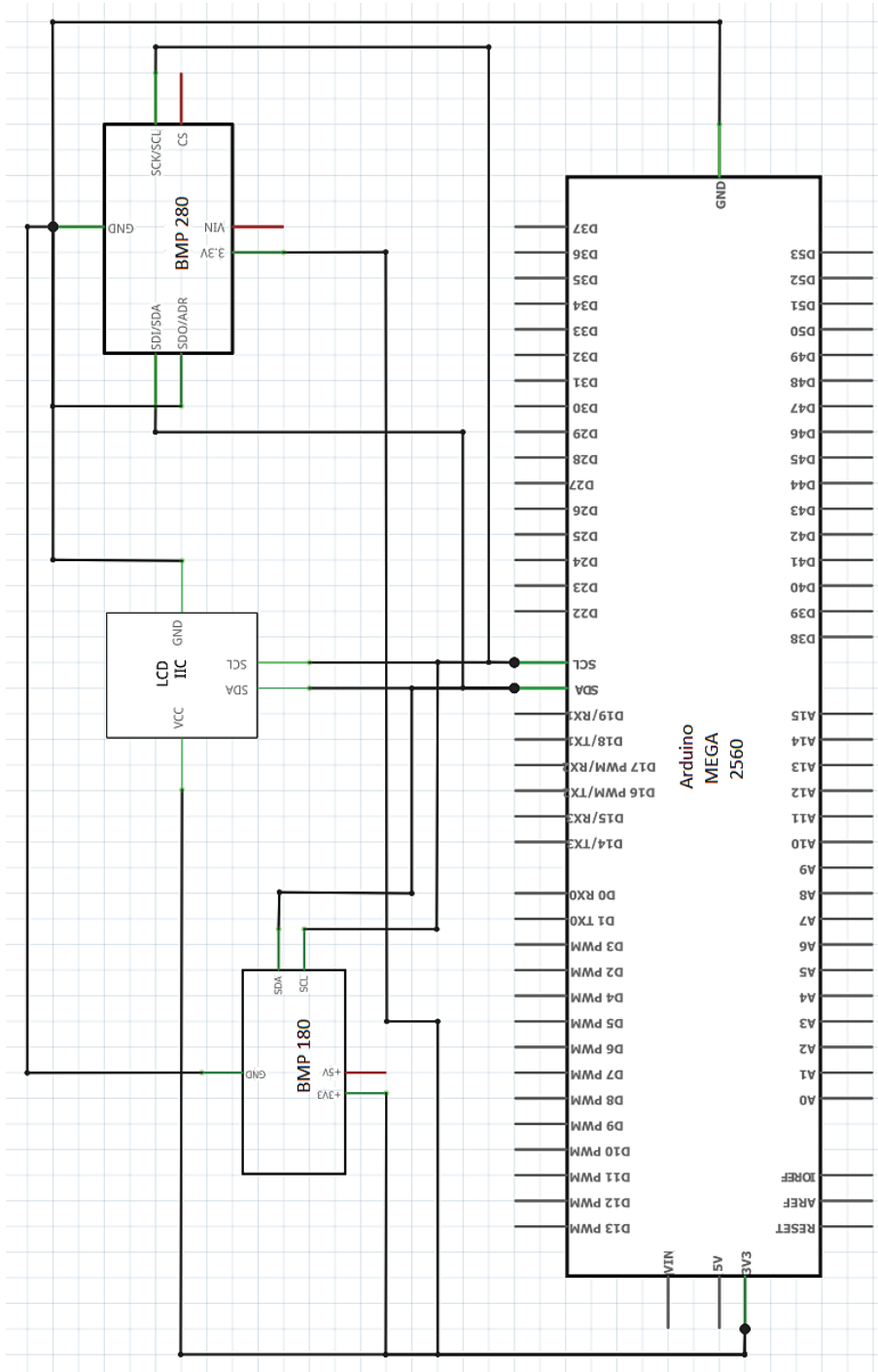

Fig. 6. Circuit diagram of the designed device

Measurements of air flow resistance in various types of air filters and discussion of the results

The operation of the proposed device was tested by measuring air flow resistance added by various types of air filters. Air flow was generated by a Volvo compression turbocharged compression ignition engine. The engine was mounted in a vehicle with a mileage of around 460,000 km. The technical specification of the engine is presented in Table 1.

Table 1

Technical specification of a turbocharged compression ignition engine

Displacement	2.401 cm^3
Fuel	Diesel oil
Maximum power	163 KM (120 kW) at 4,000 rpm
Maximum torque	340 Nm at 1,750 rpm
Compression	turbocharged
Engine layout	DOHC
Number of cylinders	5
Cylinder configuration	inline
Number of valves	20
Compression ratio	18.0 : 1
Injection	common rail direct injection
Ignition	compression ignition

The proposed measuring device before connection to the engine is presented in Figure 7.

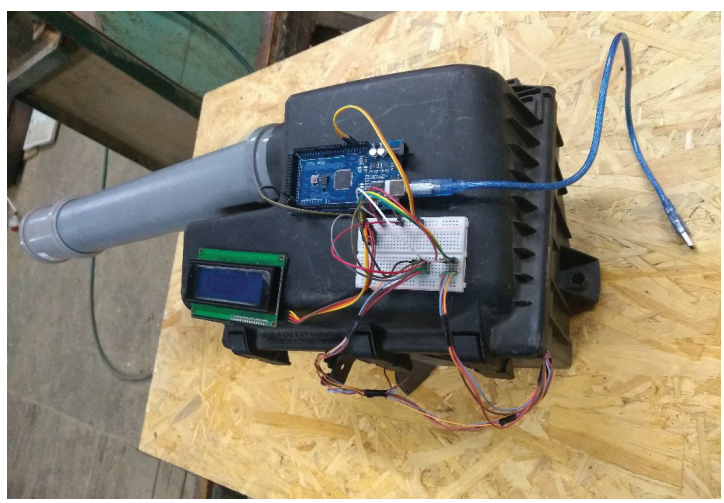

Fig. 7. The proposed device before connection to the engine

Four air filters with suitable dimensions for mounting inside the housing of the developed device were used in air flow resistance tests:

– brand-new high-performance Pipercross air filter for motor sports (Fig. 8),
– brand-new standard Mann-Filter air filter (Fig. 9),
– used standard air filter with a mileage of 10,000 km (Fig. 10),
– used standard air filter with a mileage of 20,000 km (Fig. 11).

The tested air filters are presented in Figures 8-11.

Fig. 8. Brand-new high-performance Pipercross air filter

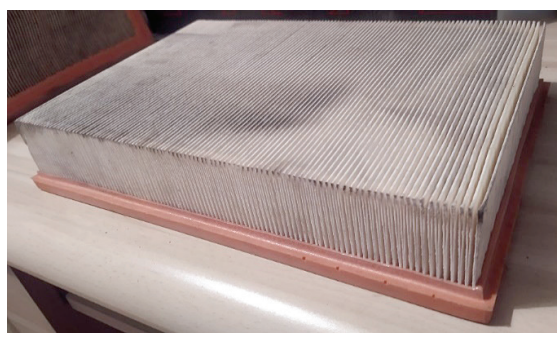

Fig.9. Brand-new standard Mann-Filter air filter

Fig. 10. Used standard air filter with a mileage of 10,000 km

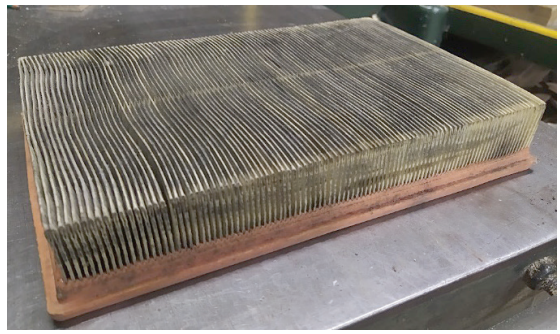

Fig. 11. Used standard air filter with a mileage of 20,000 km

Experiment and measurement results

The developed device for measuring air flow resistance was tightly connected to the engine's air intake system before the air flow meter with the use of tubes with an internal diameter of 60 mm. The measuring device was powered from a laptop via a USB port. The measuring device connected to a compression ignition engine is presented in Figure 12.

Fig. 12. Measuring device connected to a compression ignition engine

The measurements were conducted indoors at a temperature of around 25-30°C. During measurements, the rotational speed of the engine was maintained at the desired level with the accelerator pedal in the vehicle, and air pressure at the inlet and outlet of the air filter was read and recorded.

The rotational speed of the engine was read to the nearest 100 rpm. The operation of the measuring device was validated based on the results of a single series of measurements because the test stand did not support further measurements under repeatability conditions.

The differences in air pressure in front of and behind the air filter and error bars representing errors at the measurement points are presented in Figure 13.

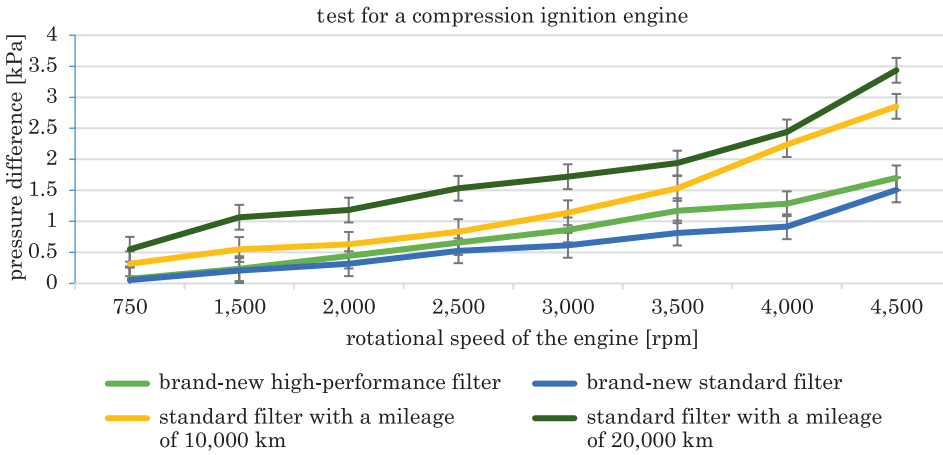

Fig. 13. Difference in the pressure of air flowing through the air filter

Pressure values were converted to kilopascals [kPa]. Since only a single series of measurements was conducted, the maximum error had to be calculated and taken into account based on the technical specification of the pressure sensors. The maximum measurement error was estimated at ±0.2 kPa. Measurement results were registered with the use of formula (BIELSKI, CIURYŁO 2001):

$$i = (\{x\} \pm \{\Delta x\}),$$

where:

i – measurement result,
x – measured value,
Δx – maximum error.

Discussion

The filtering partition adds resistance to the flow of incoming air, which leads to changes in air pressure in the air duct, measured directly in front of and behind the filtering partition. The proposed device was used to determine

the relationship between the degree of filter wear and the resulting drop in air pressure. Air pressure in the inlet duct decreased relative to atmospheric pressure with an increase in the rotational speed of the engine. As demonstrated by the diagram in Figure 13, the pressure drop generated by all of the tested filters was exacerbated by a rise in engine speed. This is because the rate at which air is sucked into the engine increases, whereas the surface area of the filtering partition remains unchanged.

When pressure measurements are conducted at low engine speed, the average air pressure may be difficult to determine because pressure values fluctuate rapidly, but within a limited range of values, in front of and behind the filtering partition. The above could be attributed to the fact that drawn air does not flow with uniform velocity in the direction of the cylinders. Cylinders, opening and closing valves, and the specific shape of the inlet duct create a pressure wave and cause air to bounce back and forth across the intake manifold. These phenomena are particularly visible at low rotational speeds of the engine.

The results shown in Figure 13 present the resistance generated by the tested filters. The standard filter, both brand-new and with a mileage of 10,000 km, created the smallest resistance. In the standard filter, air pressure decreased due to the accumulation of particulate matter over time, which led to a minor decrease in dust-holding capacity, but increased filtering efficiency. The high-performance filter for motor sports produced interesting results. Theoretically, this filter should add least resistance to air flow. However, the results of the study indicate that the high-performance filter induced a greater drop in air pressure than a brand-new standard filter. Air flow resistance was highest in the standard filter with a mileage of 20,000 km. In this filter, the greatest difference in air pressure on both sides of the air filter was around 3.5 (±0.2) kPa at engine speed of 4,500 rpm. The most worn-out filter was considerably clogged with dust, and it put up the greatest resistance to the flow of incoming air. The smallest difference in air pressure was observed in the brand-new standard filter where the maximum resistance reached 1.5 (±0.2) kPa at engine speed of 4,500 rpm.

The results of the conducted tests demonstrated that the proposed device meets expectations and correctly measures changes in air pressure. Tests involving the designed device should be conducted indoors to minimize the impact of weather phenomena (rain, wind) and sudden changes in temperature.

Conclusions

This study addresses the problem of air impurities in internal combustion engines. Various types of air filters were described. A device for measuring air flow resistance in filters was designed and built based on the adopted

requirements. The device was tested on various air filters in a compression ignition engine. The results revealed that the proposed device meets expectations and correctly measures air pressure in front of and behind an air filter in a compression ignition engine. An analysis of test results confirmed the presence of a correlation between various types of filters and filter wear. A standard air filter with a mileage of 20,000 km added the greatest resistance to air flow. At engine speed of 800 rpm, air flow resistance was very high at 0.5 (±0.2) kPa. The operation of an idling engine was disrupted and rough when the most worn filter was installed. The remaining filters did not generate such problems. The results of this study indicate that high-performance air filters for motor sports are not always characterized by lower air flow resistance than standard filters. The proposed device and the described research methodology can be used to measure air flow resistance generated by air filters in motor vehicles.

References

BIELSKI A., CIURYŁO R. 2001. *Podstawy metod opracowania pomiarów*. UMK, Toruń, p. 32-37.

BMP180 Digital pressure sensor. 2013. Datasheet, Document revision 2.5., Bosch. https://cdn-shop.adafruit.com/datasheets/BST-BMP180-DS000-09.pdf.

BMP280 Digital Pressure Sensor, Datasheet. 2015. Document revision 1.14, Bosch. https://cdn-shop.adafruit.com/datasheets/BST-BMP280-DS001-11.pdf.

CHŁOPEK Z. 2012. *Testing of hazards to the environment caused by particulate matter during use of vehicles*. Eksploatacja i Niezawodność, 2: 160-170.

CHŁOPEK Z., JAKUBOWSKI A. 2009. *Badania emisji cząstek stałych z układu hamulcowego pojazdu samochodowe*go Eksploatacja i Niezawodność, 4: 45-52.

CHŁOPEK Z., JAKUBOWSKI A. 2010. *The examination of the reduction of particulate matter emission from motor vehicle braking system*. Eksploatacja i Niezawodność, 4: 29-36.

DZIUBAK T. 2003. *Metodyka badań charakterystyk papierów filtracyjnych do filtru powietrza pojazdu eksploatowanego w warunkach dużego zapylenia powietrza*. Zagadnienia Eksploatacji Maszyn PAN, 4(136): 101-117.

DZIUBAK T. 2006. *Problemy filtracji powietrza zasysanego do spalinowych silników pojazdów mechanicznych*. Biuletyn WAT, 60(3): 77-95.

DZIUBAK T. 2016. *Zanieczyszczenia płynów eksploatacyjnych i ich wpływ na zużycie elementów silnika spalinowego pojazdu mechanicznego*. Archiwum Motoryzacji, 72(2): 43-72.

DZIUBAK T., BORCHET M. 2017. *Badanie właściwości włókninowego wkładu filtracyjnego powietrza wlotowego silnika samochodu osobowego*. Biuletyn WAT, 2: 148.

DZIUBAK T., SZWEDKOWICZ S. 2013. *Badania eksperymentalne cyklonów przelotowych filtrów powietrza silników spalinowych*. Biuletyn WAT, 62(2): 201-217.

DZIUBAK T., SZWEDKOWICZ S. 2014. *Analiza porównawcza papierów i włóknin stosowanych do filtracji powietrza wlotowego silników pojazdów mechanicznych*. Logistyka, 3: 1582-1591.

HUTTEN I.M. 2016. *Handbook of nonwoven filter media*. Butterworth-Heinemann, Oxford.

KORDZIŃSKI C., ŚRODULSKI T. 1968. *Układy dolotowe silników spalinowych*. WKiŁ, Warszawa.

Technical Sciences, 2020, 23(2), 157–174

UNIWERSYTET WARMIŃSKO-MAZURSKI W OLSZTYNIE

Quarterly peer-reviewed scientific journal
ISSN 1505-4675
e-ISSN 2083-4527
TECHNICAL SCIENCES
Homepage: www.uwm.edu.pl/techsci/

DOI: https://doi.org/10.31648/ts.5689

EFFECTS OF SONICATION AND FREEZING ON THE COLOR, MECHANICAL AND THERMOPHYSICAL PROPERTIES OF OSMO-MICROWAVE-VACUUM DRIED CRANBERRIES

Izabela Staniszewska[1], *Szymon Staszynski*, *Magdalena Zielinska*[2]

[1] ORCID: 0000-0001-7868-3794
[2] ORCID: 0000-0001-7127-4891
Department of Systems Engineering
University of Warmia and Mazury in Olsztyn

Received 16 July 2020, accepted 4 September 2020, available online 2 December 2020.

K e y w o r d s: cranberries, osmotic dehydration, ultrasound, freezing, microwave-vacuum drying.

A b s t r a c t

The aim of this study was to determine the effects of sonication (S), convective freezing (F), convective freezing preceded by sonication (SF) as well as cryogenic freezing (N) on the osmo-microwave-vacuum drying kinetics, energy usage and properties of dried cranberries such as moisture content, moisture diffusion, water activity, density, porosity, thermal conductivity, thermal diffusivity, volumetric heat capacity, lightness, redness, yellowness, total differences in color, saturation and hue, hardness, cohesiveness, springiness and chewiness. Osmo-microwave-vacuum drying of cranberries took from 13.5 to 16.0 min. All initial treatments increased the moisture diffusivity and thus reduced the drying time. The most energy effective method was osmo-microwave-vacuum drying preceded by sonication (S) of fruits. Osmo-microwave-drying of cranberries subjected to convective freezing preceded by sonication (SF) resulted in the highest lightness (32.5±0.5), redness (33.9±0.7) and yellowness (11.3±0.5) of fruits, as well as the lowest cohesion (the lowest resistant to stress associated with manufacturing, packaging, storage, and delivery). The lowest hardness, i.e. 12.3±0.4 N and the highest cohesiveness and springiness, i.e. 0.38±0.02 and 0.74±0.03 of dried fruits, were noted for berries subjected to initial cryogenic freezing (N). Cryogenic

Correspondence: Izabela Staniszewska, Katedra Inżynierii Systemów, Uniwersytet Warmińsko-Mazurski, Heweliusza 14, 10-718 Olsztyn, Poland, phone: + 48 89 523 49 72, e-mail: izabela.staniszewska@uwm.edu.pl

freezing (N) combined with osmo-microwave-vacuum drying resulted in the largest color changes of fruits and the highest thermal conductivity. Sonicated and convectively frozen (SF) fruits were characterized by the highest thermal diffusivity. Sonication (S), convective freezing (F) and their combination (SF) significantly reduced the volumetric heat capacity of cranberry fruits.

Introduction

Cranberry fruit is a rich source of bioactive compounds with antioxidant properties (ZIELINSKA et al. 2017). High moisture content, seasonality, production scale, as well as consumer preferences cause that they are often preserved by drying (ZIELINSKA, MARKOWSKI 2018). Recently, they have become of interest to the food producers as they may constitute valuable ingredients to cookies, cakes, cereals, sauces and salads due to the presence of anthocyanins and their antioxidant activity (BEAUDRY et al. 2003).

As the natural waxy layer on the surface of cranberry fruits acts as a barrier to heat and mass transfer, convective drying of cranberries is time-consuming and generates high demands for energy and operational costs. In addition, high temperature may decrease the content of thermolabile compounds and their antioxidant properties. Osmotic dehydration, which consists of immersion of fruits into a concentrated sugar solution, for example, may significantly slow down the rate of moisture removal during convective drying of cranberries (GRABOWSKI et al. 2002). Microwave-assisted drying of cranberries may provide an alternative to convective drying (WRAY, RAMASWAMY 2013, 2015, STANISZEWSKA et al. 2019, 2020, ZIELINSKA et al. 2018a, 2018b, 2019, ZIELINSKA, ZIELINSKA 2019). Microwave dielectric heating results from the ability of a given reagent to absorb the energy assigned to microwave radiation and its conversion into thermal energy. This heating, caused by the electrical component of electromagnetic radiation, occurs through the rotation of dipole molecules and ionic conductivity (NOWAK, KOWALSKA 2007). The vacuum lowers the boiling point of water. The temperature inside the dried particles is higher than that on the surface of the product. It may lead to an increase in the partial pressure that drives the evaporating water to the outer layer. The gradient between a vapor pressure in the center of the material and its surface results in high drying rates (ZHENG et al. 2003). The advantages of microwave-vacuum drying include short drying time, explosion puffing of fruits and vegetables and high quality of the final product (ZIELINSKA et al. 2019, ZIELINSKA, ZIELINSKA 2019).

Due to the natural waxy layer on the fruit surface, cranberries require special treatment to increase the permeability of the surface layer to heat and moisture transfer (NOWAK et al. 2019). Convective freezing of the material before drying may increase the efficiency of drying due to the reduction of skin thickness and then reduction of the mechanical resistance of the surface layer (ZIELINSKA

et al. 2015). Since the amount of water that migrates from the cells to intercellular space is minimal, cryogenic freezing reduces damage to the tissue structure (ZIELINSKA et al. 2019). Sonication also performed at a frequency between 18 and 100 kHz and intensity higher than 1 W/cm^2 can be used to influence food products containing water by inducing microcavitation in their structure, which may result in the so-called sponge effect, i.e. the creation of microchannels that improve heat and mass transfer between the cells and their environment (STANISZEWSKA et al. 2019). Berries can also be subjected to osmotic dehydration before drying (SIUCINSKA et al. 2016a, 2016b). Osmotic dehydration allows for removing water from raw material. When properly conducted, i.e. with the use of an appropriate osmotic substance, immersion time, temperature and the ratio of the mass of the solution to the mass of the material, it also allows maintaining the nutritional and sensory values of the preserved food (CORREA et al. 2016, KOWALSKA et al. 2016, ZIELINSKA, MARKOWSKI 2018). Osmotic dehydration significantly affects the structure of the dehydrated product, because the dehydrated cells can shrink and may even be destroyed by treating them with osmotic solutions of high concentrations. The advantages of osmotic dehydration include a reduction of enzymatic browning, nonenzymatic browning, inhibition of polyphenol oxidase activity, retention of volatile components, reduction of the product's water activity (and thus inhibition of microbial growth), enrichment of the material with nutrients from the osmotic solution, extension of product shelf life, improvement of the quality food products such as organoleptic properties, etc. (CZAJKOWSKA et al. 2016). However, this process is time-consuming and dehydrated material still needs to finish drying.

There is a scarce knowledge on the effect of sonication and freezing on the osmo-microwave-vacuum drying kinetics and quality of waxy fruits, particularly cranberries. Therefore, the objective of this study was to investigate the effects of sonication (S), convective freezing (F), convective freezing preceded by sonication (SF) and cryogenic freezing (N) on the osmo-microwave--vacuum (OM) drying kinetics, energy usage as well as color, mechanical and thermophysical properties of cranberries. To compare, raw fruits (R) without any treatment were also subjected to osmo-microwave-vacuum (OM) drying. Among the properties of dried cranberries, moisture content, moisture diffusion, water activity, density, porosity, thermal conductivity, thermal diffusivity, volumetric heat capacity, lightness, redness, yellowness, total differences in color, saturation and hue, hardness, cohesiveness, springiness and chewiness were analyzed. The results of this study can help producers and suppliers of dried berries as well as manufacturers of equipment used to process cranberry fruits.

Materials and methods

Material and initial treatments

Fresh cranberries (*Vaccinium macrocarpon* L.) were obtained from a local farm (Lublin region, Poland). Fresh fruits were free from any diseases and discoloration. They were similar in freshness and size. Raw cranberries were packed in plastic containers and stored in a refrigerator (2±2°C) for up to two weeks. The initial moisture content of fresh fruits was about 7.49±0.02 kg H_2O/kg DM. Whole cranberries of a mass of 0.250±0.003 kg were subjected to different initial treatments: sonication (S), convective freezing (F), convective freezing preceded by sonication (SF) as well as cryogenic freezing (N). Pre-treated fruits were subjected to osmo-microwave-vacuum drying (OM). The control sample was composed of non-treated, raw (R) cranberries.

Sonication (S) at a frequency of 25±5 kHz and ultrasound power of 600 W was conducted for 10 minutes in a water bath filled with 1 dm^3 of distilled water using an ultrasonic disruptor Scientz-650E (Ningbo Scientz Biotechnology Co. Ltd., Zhejiang, China).

Convective freezing (F) was conducted in Liebherr GR 4932 freezer (Liebherr-Hausgeräte GmbH, Ochsenhausen, Germany) for 24 h at a temperature of −18°C. Approximately 3 h before dehydration, frozen cranberries were thawed on a tray at room temperature to reach equilibrium temperature (21±1°C).

Cryogenic freezing (N) was conducted in a styrofoam container filled with liquid nitrogen for 1 min. The boiling point of liquid used for the freezing experiment was −196°C. Cryogenic freezing was considered to be completed when the evaporation of liquid nitrogen was no longer observed. After cryogenic freezing (N), cranberries were removed from the container and left for 3 h to reach ambient temperature.

All of the initial treatments were conducted in triplicate.

Dehydration process

Pre-treated whole cranberries were subjected to osmo-microwave-vacuum drying (OM). Osmotic dehydration of whole cranberries was conducted in a bath (EMAG Emmi 20 HC, EMAG AG, Moerfelden-Walldorf, Germany) filled with a sucrose solution. The concentration of sucrose solution was 65°Brx. Raw (non-treated) and pre-treated cranberries were dehydrated at room temperature (20°C) and atmospheric pressure for 6 h. The sample to solution ratio was 1:4. After completion of the osmotic dehydration, samples were rinsed and blotted with tissue paper. Osmotic dehydration experiments were conducted in triplicate.

After osmotic dehydration, the fruits were dried in a microwave-vacuum dryer (PROMIS TECH, Wroclaw, Poland) at a microwave power of 300 W and absolute pressure of 5±1 kPa. The mass of the sample used in each drying experiment was 0.200±0.003 kg. Microwave-vacuum drying was stopped when the surface temperature of fruits increased to 80°C. The microwave-vacuum dryer (Promis Tech, Wroclaw, Poland) was equipped with a pyrometer to measure the surface temperature of cranberries. The drying experiments were conducted in duplicate.

The moisture content (MC) of cranberries was measured by a DZ ZBC II vacuum drying oven (Chemland, Stargard Szczeciński, Poland) according to the standard (AOAC, 2002). The oven temperature was set at 70°C (13.3 kPa) and the heating time was 24 h. The result was the mean of two replications. Water activity (a_w) was measured using the Aquaspector AQS-31-TC (NAGY, Gaufelden, Germany). The result was the mean of two replications.

The coefficient of moisture diffusion was determined from the equation (1) assuming constant values of the effective moisture diffusion coefficient and fruit shape as well as considering initial (2) and boundary conditions (3) (ZIELINSKA, MARKOWSKI 2018):

$$\frac{u(\tau) - u_r}{u_0 - u_r} = \frac{6}{\pi^2} \cdot \sum_{n=1}^{\infty} \frac{1}{n^2} \exp\left(-n^2 \cdot n^2 \cdot \frac{D_{eff} \cdot \tau}{R^2}\right) \tag{1}$$

$$u(t = 0, x, y, z) = u_0 \tag{2}$$

$$t > 0 \rightarrow u(t, x, y, z) = u_r \tag{3}$$

where:

$u(\tau)$ – indicates the moisture content at a particular drying time τ [kg H_2O/kg DM],
u_r – indicates the equilibrium moisture content [kg H_2O/kg DM],
u_0 – indicates the initial moisture content [kg H_2O/kg DM],
n – indicates the number of measurements [–],
D_{eff} – indicates the effective moisture diffusivity [m^2/s],
τ – indicates drying time [s],
R – indicates the radius of a sphere [m].

The energy consumption during drying was measured using the energy meter (MPR-53/EPM-07, model MPR-53S, ENTES Elektronik Cihazlar Imalatve Ticaret A.S., Istanbul, Turkey). The specific moisture extraction rate (SMER) was expressed as follows (SCHMIDT et al. 1998):

$$\text{SMER} = \frac{M_{mr}}{E_{\text{input}}} \tag{4}$$

where:

M_{mr} – indicates the mass of moisture removed from the dried material [kg H_2O],

E_{input} – indicates the energy input [kWh].

Quality assessment

Color was measured with a spectrophotometer (Hunterlab MiniScan XE Plus, Reston, VA, USA) under standard illuminant D65, 10° observer and 8° diaphragm. The spectrophotometer cooperated with the MultiScan v.11.06 software. The color of fruits was expressed in CIE $L^*a^*b^*$ space, where the achromatic component L^*, as well as two chromatic components a^*, and b^* denoted lightness, redness and yellowness, respectively. The color of cranberries was measured directly on the fruit surface. The total changes in color (ΔE^*), saturation (ΔC^*) and hue (ΔH^*) during processing were calculated according to the formulas presented in the literature (ZIELINSKA, MARKOWSKI 2012). The results were averaged over 32 measurements.

The overall appearance was evaluated based on the macrographs of the fruit surface. The macrographs were obtained using a digital camera (Sony DSC-HX50, Sony Corporation, Tokyo, Japan).

Texture profile analysis was performed using a TA-HD plus texture analyzer (Stable Micro Systems, Godalming, UK). Mechanical properties of fruits were automatically computed using Texture Exponent Stable Micro Systems v.6.1.11 texture-analyzing software. Hardness was defined as the maximum force measured during the first compression. Cohesiveness was defined as the ratio of the area during the second compression of the sample to the area of the first sample compression. Springiness was defined as the ratio of time from the start of the second area up to the second probe reversal over time between the start of the first area and the first probe reversal. Chewiness was defined as the product of hardness, cohesiveness and springiness (CHONG et al. 2014). The results were averaged over 15 measurements.

Particle density (ρ_p) was measured using the hydrostatic method and calculated using the following formula (RAHMAN 1995):

$$\rho_p = \frac{m_p}{m_p - m_w} \cdot \rho_w \tag{5}$$

where:

ρ_p – indicates particle density [kg/m^3],

ρ_w – indicates water density [kg/m^3],

m_w – indicates the mass of sample immersed in water [kg],

m_p – indicates the mass of sample in the air [kg].

The true density of cranberries was measured with a pycnometer. Cranberries were dried at 70°C (13.3 kPa) for 24 h in the vacuum drying oven DZ ZBC II (Chemland, Stargard Szczeciński, Poland) according to the standard (AOAC, 2002) and ground in a laboratory mill. A sample mass of approximately 0.002 kg was used in each experiment. The mass of the sample was measured using an electronic balance (RADWAG, WPS 4000/C/2, Radom, Poland). Non-water miscible liquid (xylene) and a calibrated glass pycnometer with an estimated volume of 50 ml (LG-3838-3658, Chemland Ltd., Poland) were used. The density of xylene was determined at 864 ± 1 kg/m^3. The true density of fruits (6) and volumetric shrinkage (7) were calculated according to the formulas presented in the literature (ZIELINSKA et al., 2015):

$$\rho_T = \frac{864 \cdot (W_3 - W_1)}{W_2 + (W_3 - W_1) - W_4} \tag{6}$$

where:

ρ_T – indicates true density [kg/m^3],
W_1 – indicates the mass of an empty pycnometer [kg],
W_2 – indicates the mass of the pycnometer filled with the non-solvent [kg],
W_3 – indicates the total mass of the pycnometer and the sample [kg],
W_4 – indicates the total mass of the pycnometer, the non-solvent and the sample [kg].

The volumetric shrinkage (S_V) was calculated according to the following formula (ZIELINSKA et al. 2015):

$$S_V = \left(1 - \frac{V_{(\tau)}}{V_0}\right) \cdot 100\% \tag{7}$$

where:

S_V – indicates volumetric shrinkage [%],
V_0 – indicates the initial volume of the sample [m^3],
$V_{(\tau)}$ – indicates the volume of the sample at a particular drying time τ [m^3].

Apparent porosity (ε_{ap}) was calculated from the following formula (NOWAK et al. 2019):

$$\varepsilon_{ap} = \left(1 - \frac{\rho_p}{\rho_T}\right) \cdot 100\% \tag{8}$$

where:

ε_{ap} – indicates apparent porosity [%],
ρ_p – indicates particle density [kg/m^3],
ρ_T – indicates true density [kg/m^3].

Thermal conductivity (λ), thermal diffusivity (α) and volumetric heat capacity (C_V) of cranberries were determined using a thermal analyzer (KD2 Pro meter, Decagon Devices, Pullman, USA) with a dual-needle SH-1 sensor. The dual-needle

sensor was inserted into the fruits (ZIELINSKA et al. 2018a). The measurements were performed in five replicates.

The calculations were done using STATISTICA 12.0 software (StatSoft Inc., Tulsa, OK, USA). One-way ANOVA analysis (Duncan's test) was performed for samples with a normal distribution ($p \leq 0.05$). The analysis of variance for independent samples (Kruskal-Wallis's test) was carried out for samples without a normal distribution ($p \leq 0.05$).

Results and discussion

Osmo-microwave-vacuum drying of cranberries took from 13.5 to 16.0 min (Fig. 1). The longest drying time was recorded for non-treated samples (R). Osmo--microwave-vacuum drying of raw (non-treated) cranberries was longer by 33% than microwave-vacuum drying of whole fruits, while osmo-microwave-vacuum drying of fruits subjected to S, F and SF treatment was shorter by 7%, 4% and 3% than microwave-vacuum drying of whole fruits (STANISZEWSKA et al. 2019). There were no significant differences between the drying times of microwave--vacuum and osmo-microwave-vacuum cryogenically frozen fruits (STANISZEWSKA et al. 2019). The initial moisture content (MC_I) of osmotically dehydrated fruits that were not subjected to any additional treatment was 7.61±0.02 kg H_2O/kg DM. The use of N, S, F and SF treatments reduced MC_I of fruits by 28%, 9%, 3% and 3%, respectively (Fig. 1). The highest moisture losses were observed during osmotic dehydration of cryogenically frozen berries. They could be attributed to the considerable skin ruptures. However, initial cryogenic freezing (N) reduced osmo-microwave-vacuum drying time only by 9%. Sonication (S) and convective freezing (F) intensified the moisture removal during drying and resulted in the shortest osmo-microwave-vacuum drying time, i.e. 13.5 min. The reason could be severe damage to the cranberry's microstructure during convective freezing (F) and rupture of the berry fruit surface due to high-frequency ultrasound (S) treatment (STOJANOVIC, SILVA 2007, ZIELINSKA et al. 2018a).

In the present study, the specific moisture evaporation rate of drying (SMER) ranged from 2.98±0.02 to 4.54±0.02 kg H_2O/kWh (Fig. 1). SMER of osmo--microwave-vacuum drying of non-treated fruits (R) was 4.40±0.02 kg H_2O/kWh. SMER of osmo-microwave-vacuum drying of initially sonicated (S) fruits was significantly higher than that of osmo-microwave-vacuum drying of raw (R) fruits dried without any initial treatment. It indicates that for the same energy input sonication allowed to evaporate a greater amount of moisture than from non-treated berries. The changes in SMER values are related to the changes in the local temperature of the whole cranberries during microwave-vacuum drying (STANISZEWSKA et al. 2019). The results indicated the lowest changes in the local temperature of the material during osmo-microwave-vacuum

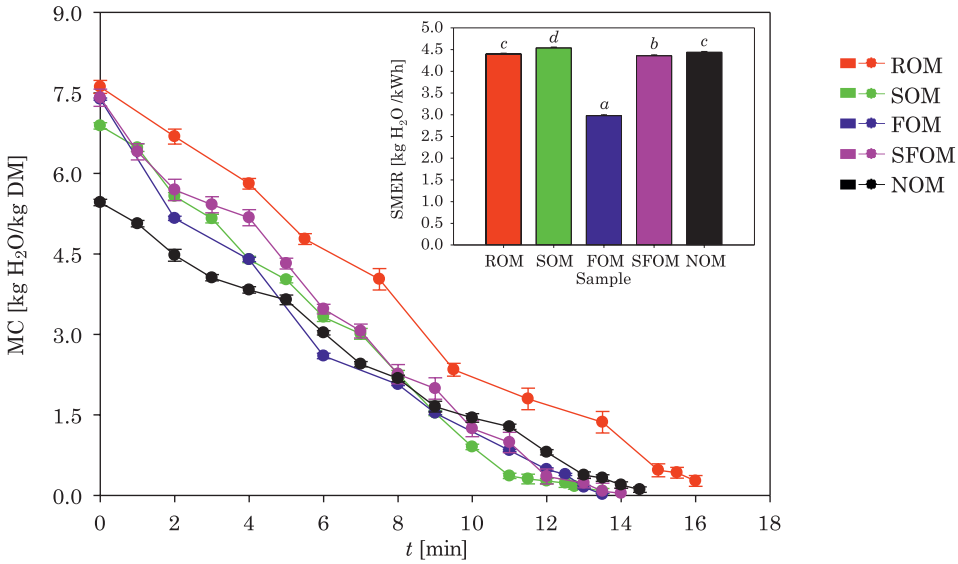

abcd – the same letters in columns mean no statistical differences between samples ($p \leq 0.05$); Symbols: MC – moisture content [kg H_2O/kg DM], t – time [min], SMER – specific moisture evaporation rate during microwave-vacuum drying at a microwave power of 300 W [kg H_2O/kWh], R – raw (non-treated), S – sonication, F – convective freezing, SF – sonication combined with convective freezing, N – cryogenic freezing, OM – osmo-microwave-vacuum drying

Fig. 1. Changes in moisture contents vs. drying times and specific moisture evaporation rates during osmo-microwave-vacuum drying of non-treated and pre-treated cranberries

drying of sonicated (S) fruits. On the other hand, osmo-microwave-vacuum drying of convectively frozen (F) berries was characterized by the highest energy consumption used for moisture evaporation. SMER of osmo-microwave--vacuum drying of berries subjected to initial freezing (F) was significantly lower (by 32%) than SMER of osmo-microwave-vacuum drying of fruits without any initial treatment (R). The study on the effectiveness of initial treatments on the improvement of SMER of osmo-microwave-vacuum drying showed the best results for sonication (S). There were no significant differences between SMER of osmo-microwave-vacuum drying of cryogenically frozen (N) and non-treated (R) fruits. Convective freezing preceded by sonication (SF) and convective freezing alone (F) decreased SMER of osmo-microwave-vacuum drying and thus reduced the energy efficiency of drying compared to osmo-microwave-vacuum drying of fruits without any initial treatment (Fig. 1). However, SMER of microwave--vacuum drying of convectively frozen (F) cranberries was 54% higher than SMER of osmo-microwave-vacuum drying of cranberry fruits (STANISZEWSKA et al. 2019). This indicated that microwave-vacuum drying of convectively frozen (F) fruits was much more energy-efficient than osmo-microwave-vacuum drying. Osmo--microwave-vacuum drying of raw (R), sonicated (S), sonicated and convectively

frozen (SF) as well as cryogenically frozen (N) cranberries was more effective than microwave-vacuum drying of fruits (STANISZEWSKA et al. 2019).

The effective moisture diffusivity (D_{eff}) of whole cranberries was significantly influenced by the pre-treatments (Tab. 1). The values of D_{eff} of osmo-microwave--vacuum dried cranberries ranged from 2.83±0.02 to 5.09±0.02 × 10^{-9} m^2/s. Convective freezing (F), sonication (S), their combination (SF) as well as cryogenic freezing (N) increased the moisture diffusivity of fruits and shortened the drying time. The highest D_{eff} value was noted for samples subjected to convective freezing (F) (Tab. 1). Among different pre-treatments, cryogenic freezing (N) resulted in the lowest increase in D_{eff} values of dried fruits. The reason can be the freeze--cracking of cranberry fruits when subjected to a very high freezing rate and/or a very low freezing temperature (ZIELINSKA et al. 2019).

Osmo-microwave-vacuum drying produced berries of water activity (a_w) lower than the critical value ($a_w \leq 0.6$), which limit the growth of microorganisms (YOGENDRARAJAH et al. 2015) (Tab. 1).

Particle density (ρ_p) of berry fruits decreased significantly during osmo--microwave-vacuum drying, while their particle porosity (ε_{ap}) increased (Tab. 1). The reason for this can be a "puffing effect", which resulted in the concentration of dry matter components and an increase in the number of pores (FIGIEL 2009). Osmo-microwave-vacuum dried samples subjected to convective freezing (F) and sonication combined with convective freezing (SF) were characterized by the highest porosity, i.e. 89%±1%. Osmo-microwave-vacuum dried samples subjected to initial cryogenic freezing (N) were characterized by the lowest porosity, i.e. 81%±5%, and the highest density, i.e. 263%±68 kg/m^3. However, convective freezing (F) and convective freezing combined with sonication (SF) resulted in significantly lower (19% and 21%, respectively) density of osmo-microwave--vacuum dried cranberries than that dried without any initial treatment (R). The results are consistent with published data (NOWAK et al. 2019). Most probably, the formation of ice crystals during slow mechanical freezing and further thawing of fruits resulted in a significant change in the fruit structure, with severe cell damage, water loss, density decrease and porosity increase (NOWAK et al. 2019). There was no significant effect of the pre-treatments on the volumetric shrinkage of osmo-microwave-vacuum dried cranberries (Tab. 1).

Osmo-microwave-vacuum drying significantly decreased thermal conductivity (λ) and volumetric heat capacity (C_V), as well as significantly increased thermal diffusivity (a) of cranberry fruits (Tab. 1). Lower values of thermal conductivity (λ) of dried cranberries resulted from a significant decrease in moisture content and a significant increase in porosity of fruits (thermal conductivity and volumetric heat capacity of water are much higher than other food constituents, such as proteins, fat, carbohydrates) (ZIELINSKA et al. 2018a). The values of λ, α and C_V of osmo--microwave-vacuum dried cranberries subjected to initial treatments ranged from 0.061±0.006 to 0.083±0.002 W/mK, from 1.23±0.04 to 1.60±0.08 × 10^{-7} m^2/s

Table 1

Thermophysical properties of raw (non-treated) and pre-treated cranberries subjected to osmo-microwave-vacuum drying

Sample	MC [kg H_2O/kg DM]	$D_{eff} \times 10^9$ [m^2/s]	a_w [-]	ρ_p [kg/m^3]	ε_{ap} [%]	S_v [%]	λ [W/mK]	$\alpha \times 10^7$ [m^2/s]	C_V [MJ/m^3K]
R*	7.49 ± 0.02^a	-	0.965 ± 0.002^d	672 ± 7^d	52 ± 1^a	-	0.248 ± 0.003^d	1.06 ± 0.01^d	2.351 ± 0.040^c
ROM	7.61 ± 0.12^a	2.83 ± 0.02^a	0.277 ± 0.004^b	188 ± 17^b	87 ± 1^{bc}	45 ± 4^a	0.071 ± 0.003^{ab}	1.21 ± 0.03^c	0.589 ± 0.018^b
SOM	6.89 ± 0.06^c	4.10 ± 0.02^d	0.282 ± 0.001^b	190 ± 1^b	86 ± 2^{bc}	51 ± 7^a	0.061 ± 0.006^a	1.23 ± 0.04^c	0.495 ± 0.039^a
FOM	7.39 ± 0.02^b	5.09 ± 0.02^e	0.280 ± 0.006^b	149 ± 18^a	89 ± 1^c	47 ± 4^a	0.069 ± 0.006^{ab}	1.42 ± 0.04^b	0.482 ± 0.034^a
SFOM	7.41 ± 0.16^a	3.68 ± 0.02^c	0.264 ± 0.004^a	152 ± 10^a	89 ± 1^c	51 ± 4^a	0.078 ± 0.002^c	1.60 ± 0.08^a	0.492 ± 0.022^a
NOM	5.46 ± 0.06^d	3.06 ± 0.01^b	0.312 ± 0.001^c	263 ± 68^c	81 ± 5^b	56 ± 4^a	0.083 ± 0.002^c	1.39 ± 0.03^b	0.602 ± 0.017^b

Table contains mean values ± standard errors;
^{abcd} – the same letters in columns indicate no statistical differences between samples ($p \leq 0.05$);
* – data obtained from the outside source (ZIELINSKA et al. 2018a);
symbols: MC – moisture content [kg H_2O/kg DM], D_{eff} – coefficient of effective moisture diffusivity [m^2/s], a_w – water activity [-], ρ_p – particle density [kg/m^3], ε_{ap} – particle porosity [%], S_v – volumetric shrinkage [%], λ – thermal conductivity [W/mK], α – thermal diffusivity [m^2/s], C_V – volumetric heat capacity [MJ/m^3K], R – raw (non-treated), S – sonication, F – convective freezing, SF – sonication combined with convective freezing, N – cryogenic freezing, OM – osmo-microwave-vacuum drying

and from 0.482±0.034 to 0.602±0.017 MJ/m^{3}K, respectively. Osmo-microwave--vacuum drying of fruits combined with cryogenic freezing (N) resulted in 20% higher values of thermal conductivity than osmo-microwave-vacuum drying of berries without any initial treatment (Tab. 1). Osmo-microwave-vacuum drying combined with sonication and convective freezing (SF) produced berries of the highest thermal diffusivity i.e. 1.60±0.08 × 10^{-7} m^2/s. Osmo-microwave--vacuum drying preceded by S, F or SF treatments resulted in significantly lower (up to 18%) values of volumetric heat capacity of fruits than osmo-microwave--vacuum drying of berries without any initial treatment (Tab. 1).

The color of dried cranberries was significantly affected by drying and pretreatment methods (Figs. 2*a* and 2*b*). Osmo-microwave-vacuum drying of non--treated berries caused a decrease in lightness (L^*), redness (a^*) and yellowness (b^*) of fruits by 16%, 17% and 51%, respectively (Fig. 2*a*). Osmo-microwave-vacuum drying preceded by any initial treatment used in this study resulted in lighter, more red and more yellow fruits than osmo-microwave-vacuum drying without any initial treatment. Convective freezing, both alone (F) and in combination with sonication (SF), significantly increased a^* and b^* of osmo-microwave-vacuum dried fruits (Figs. 3*a*, 3*d* and 3*e*). As the color of cranberries is determined mostly by the content of monomeric anthocyanins (mainly peonidin-3-O-galactoside and cyanidin-3-O galactoside) and yellow flavonoids, it is expected that osmo--microwave-vacuum drying of convectively frozen fruits, both alone (F) and in combination with sonication (SF), will result in a high antioxidant activity of fruits (ZIELINSKA et al. 2018b). The lowest total changes in color (ΔE^*) and hue (ΔH^*) were observed during osmo-microwave-vacuum drying of fruits subjected to convective freezing preceded by sonication (SF) and they were 2.6±0.9 and 3.5±0.8, respectively (Fig. 2*b*). Osmo-microwave-vacuum drying of fruits subjected to convective freezing preceded by sonication (SF) produced berries of the highest L^* (32.5±0.5), a^* (33.9±0.7), and b^* (11.3±0.5) values. The values of L^*, a^*, and b^* of fruits subjected to convective freezing preceded by sonication (SF) were even higher than that achieved by raw (non-treated) berries (31.1± 0.3, 22.5±0.6 and 8.4±0.4) (Fig. 2*a*). The reason for this may be that ice crystals formed during convective freezing (F) destroyed the structure of the fruits and resulted in a greater release of berry juice, which could have influenced color intensification (ZIELINSKA, ZIELINSKA 2019).

However, the lowest total color change (ΔE^*) indicated that osmo-microwave--vacuum drying of cranberries subjected to initial SF treatment produced berries of the most similar color to the raw (R) fruits (Figs. 3*a* and 3*e*). The lowest L^*, a^*, and b^* parameters were achieved by non-treated cranberries subjected to osmo-microwave-vacuum drying (ROM) (Fig. 2*a*). Samples subjected to cryogenic freezing (N) were characterized by the highest values of ΔE^* and ΔH^*, i.e. 14.9±0.7 and 15.6±1.4, respectively (Fig. 2*b*). The results indicate that cryogenic freezing (N) combined with osmo-microwave-vacuum drying resulted in the greatest changes in sample color (Fig. 3*a* and 3*f*).

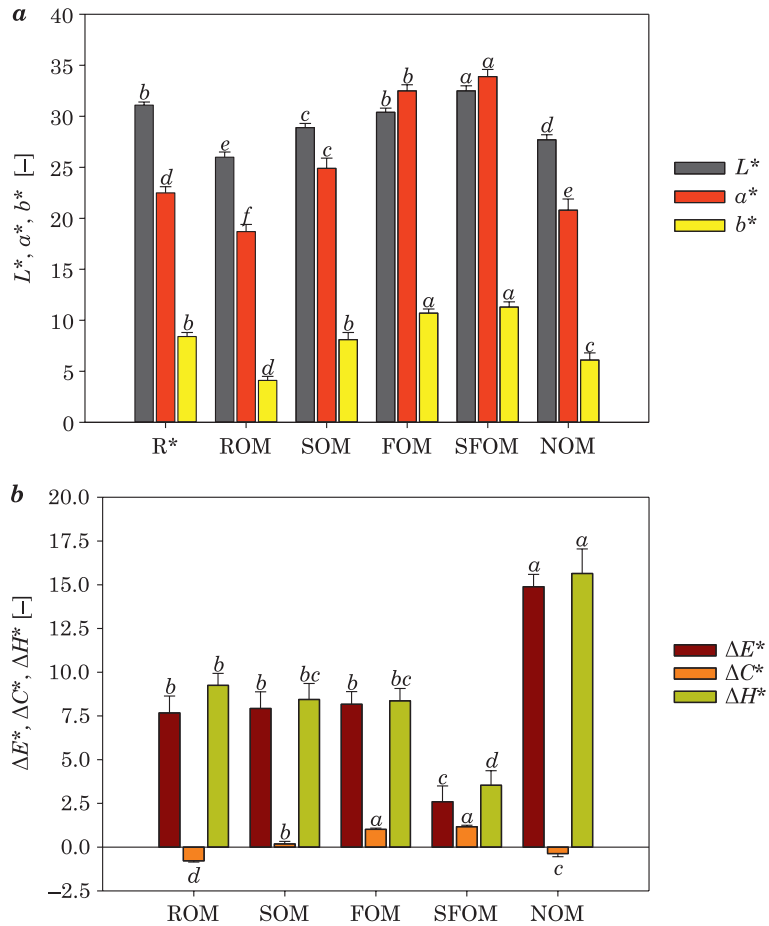

abcd – the same letters in columns mean no statistical differences between samples ($p \leq 0.05$);
* – data obtained from the outside source (ZIELINSKA, ZIELINSKA 2019);
Symbols: L^* – lightness [-], a^* – redness [-], b^* – yellowness [-], ΔE^* – total color difference [-], ΔC^* – total saturation difference [-], ΔH^* – total hue difference [-], R – raw (non-treated), S – sonication, F – convective freezing, SF – sonication combined with convective freezing, N – cryogenic freezing, OM – osmo-microwave-vacuum drying

Fig. 2. Color parameters and total differences in color, saturation and hue between raw (non-treated) and pre-treated cranberries subjected to osmo-microwave-vacuum drying: *a* – lightness, redness and yellowness, *b* – total color difference, total saturation difference and total hue difference

The values of hardness (H), chewiness (Ch), cohesiveness (C) and springiness (Sp) of cranberries subjected to different pre-treatments and osmo-microwave--vacuum drying are shown in Figures 4*a* and 4*b*. Hardness (H), chewiness (Ch), cohesiveness (C) and springiness (Sp) of raw (R) non-dried fruits were 63.7±2.5 N, 10.2±0.8 N, 0.23±0.01 and 0.71±0.01, respectively (ZIELINSKA et al. 2019).

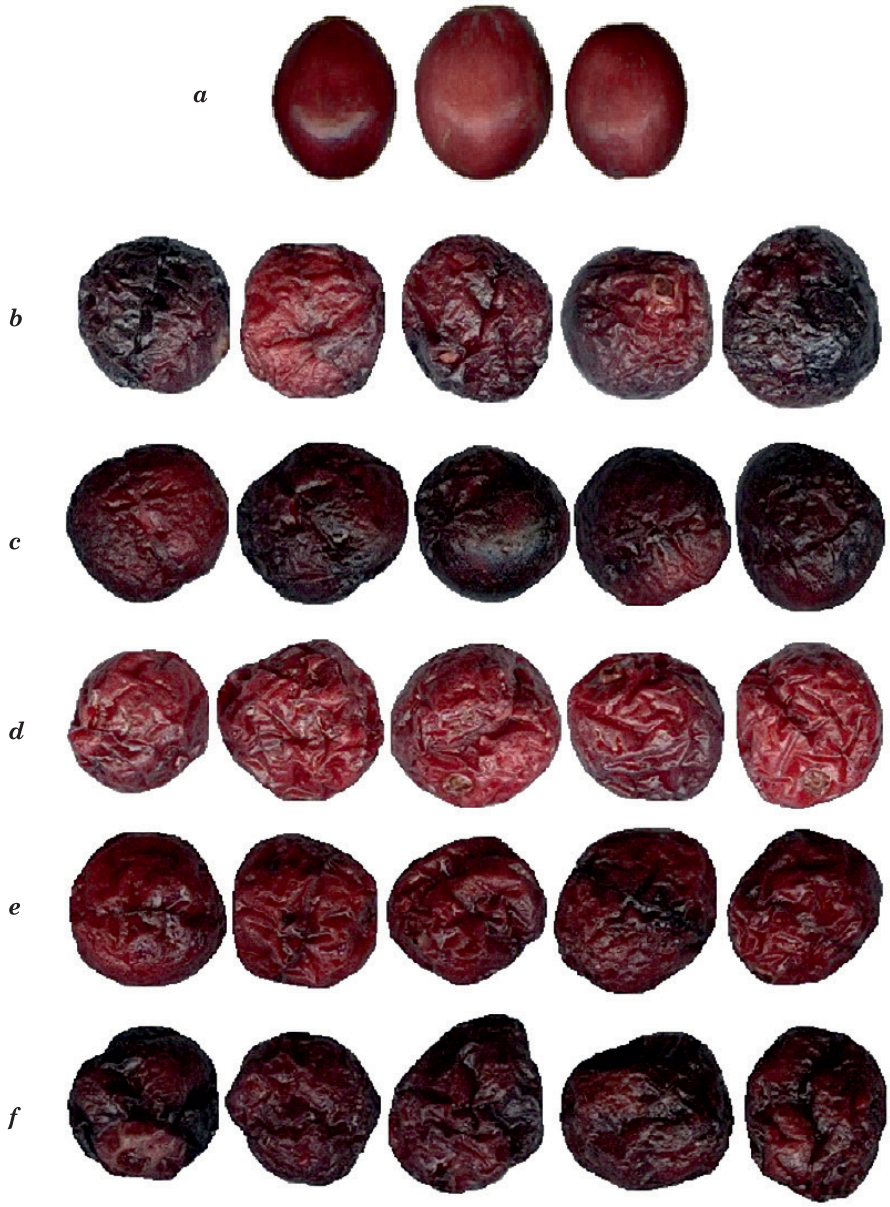

Fig. 3. The overall appearance of: *a* – raw cranberries (R), *b* – raw (non-treated) fruits subjected to osmo-microwave-vacuum drying (ROM), *c* – fruits subjected to sonication and osmo-microwave-vacuum drying (SOM), *d* – fruits subjected to convective freezing and osmo-microwave-vacuum drying (FOM), *e* – fruits subjected to sonication combined with convective freezing and osmo-microwave-vacuum drying (SFOM), *f* – fruits subjected to cryogenic freezing and osmo-microwave-vacuum drying (NOM)

Osmo-microwave-vacuum drying of non-treated fruits significantly decreased their hardness and increased their cohesiveness by 47% and 39%, respectively. Osmo-microwave-vacuum drying did not affect the chewiness or springiness of fruits.

Hardness, chewiness, cohesiveness and springiness of dried cranberries ranged from 12.3±0.4 to 33.9±0.3 N, from 3.2±0.4 to 8.1±0.8 N, from 0.19±0.01 to 0.38±0.02 and from 0.62±0.02 to 0.74±0.03, respectively (Fig. 4).

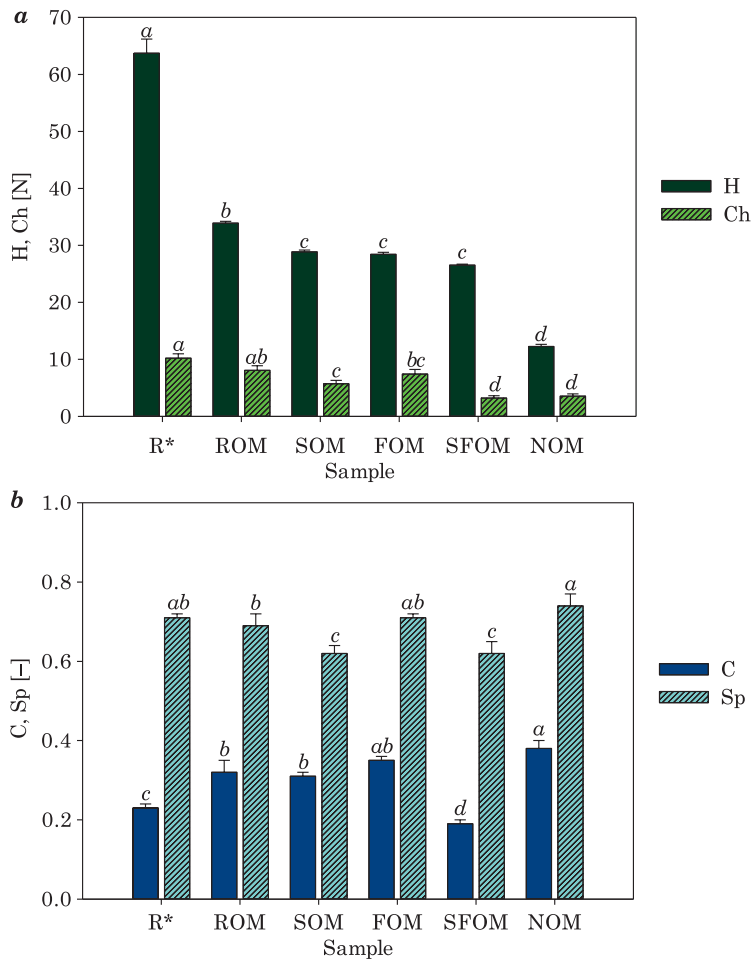

abcd – the same letters in columns indicate no statistical differences between samples ($p \leq 0.05$);
* – data obtained from the outside source (ZIELINSKA et al. 2019);
Symbols: H – hardness [N], Ch – chewiness [N], C – cohesiveness [-], Sp – springiness [-], R – raw (non-treated), S – sonication, F – convective freezing, SF – sonication combined with convective freezing, N – cryogenic freezing, OM – osmo-microwave-vacuum drying

Fig. 4. The values of: *a* – hardness and chewiness, *b* – cohesiveness and springiness of raw (non-treated) and pre-treated cranberries subjected to osmo-microwave-vacuum drying

All of the initial treatments significantly reduced the hardness and chewiness of osmo-microwave-vacuum dried cranberries. Cryogenic freezing (N) combined with osmo-microwave-vacuum drying of whole cranberries produced dried fruits with the highest springiness (Sp) and the lowest chewiness (Ch). This can be applied to produce soft dried fruits eaten together with cereals. Sonication combined with convective freezing (SF) and osmo-microwave-vacuum drying produced cranberries of the lowest chewiness (Ch), cohesiveness (C) and springiness (Sp). This proves that SF treatment, combined with osmo-microwave-vacuum drying can be applied to produce dried healthy crispy snacks. On the other hand, sonication combined with convective freezing (SF) resulted in a significantly lower (0.19±0.01) cohesiveness (C) of dried fruits than convective freezing (F) alone (0.35±0.01) (Fig. 4*b*). The results show that products of high cohesiveness are more attractive and they have more desired sensory properties than fruits of low cohesiveness. Convective freezing (F) combined with osmo-microwave-vacuum drying can thus be recommended for the production of berries with high resistance to stress associated with manufacturing, packaging, storage and delivery.

Summary

All of the initial treatments used in the present study significantly affected the drying curves, times and energy usage as well as the color, mechanical and thermophysical properties of osmo-microwave-vacuum dried cranberries. Osmo-microwave-vacuum drying of cranberries took from 13.5 to 16.0 min. All pre-treatments increased the moisture diffusivity of fruits and thus reduced the drying time. Convective freezing (F) and sonication (S) resulted in the greatest increase in the moisture diffusivity of dried fruits and, thus, the shortest drying time, i.e. 13.5 min. Pre-treatments significantly influenced energy consumption during osmo-microwave-vacuum drying. Sonication (S) resulted in the lowest energy input required for moisture evaporation during osmo-microwave-vacuum drying of berries. Despite the same drying time, osmo-microwave-vacuum drying of cranberries subjected to sonication (S) was much more energy-efficient than that subjected to convective freezing (F). Nevertheless, convective freezing (F) and convective freezing combined with sonication (SF) gave good results in terms of the color of dried fruits. Convective freezing in combination with sonication (SF) significantly reduced total color changes (ΔE^*) during drying. It then improved the color of dried cranberries and produced berries with the highest lightness, redness and yellowness. Their color was most similar to the color of fresh fruits. Sonication combined with convective freezing (SF) and osmo--microwave-vacuum drying also allowed to produce cranberries with the lowest chewiness, cohesiveness and springiness and, thus, can be recommended for

the production of dried crispy snacks. However, SF berries will be less resistant to stress associated with manufacturing, packaging, storage and delivery than non-treated (R), sonicated (S), convective frozen (F) and cryogenic frozen (N) fruits with higher cohesion values. Cranberries subjected to sonication (S), convective freezing (F) and convective freezing combined with sonication (SF) were characterized by lower volumetric heat capacity than berries dried without any initial treatment. In addition, sonication combined with convective freezing (SF) and osmo-microwave-vacuum drying produced berries with the highest thermal diffusivity. Among different initial treatments, cryogenic freezing (N) combined with osmo-microwave-vacuum drying allowed producing dried fruits with the highest values of density and thermal conductivity. It also produced berries of good quality in terms of mechanical properties, i.e. high springiness and low chewiness. However, it resulted in the biggest changes in the color of dried fruits.

Acknowledgements

This study was supported by the Polish National Science Center (grant No. 2015/17/B/NZ9/03601, title: *The effect of unconventional pretreatment methods on the kinetics of hybrid dehydration and physical and chemical properties of cranberries Vaccinum macrocarpon)* and the University of Warmia and Mazury in Olsztyn (grant No. 16.610.001-300).

References

BEAUDRY C., RAGHAVAN G.S.V., RENNIE T.J. 2003. *Microwave finish drying of osmotically dehydrated cranberries*. Drying Technology, 21(9): 1797-1810.

CHONG CH.H., FIGIEL A., CHUNG L.L., WOJDYLO A. 2014. *Combined Drying of Apple Cubes by Using of Heat Pump, Vacuum-Microwave, and Intermittent Techniques*. Food Bioprocess Technology, 7: 975-989.

CORREA J.L.G., DANTAS V.A., DE MENDONCA K.S., JUSTUS A. 2016. *Optimization of pulsed vacuum osmotic dehydration of sliced tomato*. In: *Drying and Energy Technologies*. Eds. J. Delgado, A. Barbosa de Lima. Advanced Structured Materials, 63. Springer, Cham.

CZAJKOWSKA K., KOWALSKA H., CICHOWSKA J., WOJNOWSKI M. 2016. *Osmotic dehydration of apple in chokeberry juice concentrate*. Postępy Techniki Przetwórstwa Spożywczego, 2: 5-11.

FIGIEL A. 2009. *Drying kinetics and quality of vacuum-microwave dehydrated garlic cloves and slices*. Journal of Food Engineering, 94: 98-104.

GRABOWSKI S., MARCOTTE M., POIRIER M., KUDRA T. 2002. *Drying characteristics of osmotically pretreated cranberries – energy and quality aspects*. Drying Technology, 20(10): 1989-2004.

KOWALSKA H., CZAJKOWSKA K., CICHOWSKA J., SKARŻYNSKA K. 2016. *Zastosowanie odwadniania osmotycznego w produkcji żywności mało przetworzonej*. Postępy Techniki Przetwórstwa Spożywczego, 1: 87-99.

NOWAK I., KOWALSKA S. 2007. *Application of microwaves in chemistry*. Analityka: Nauka i Praktyka, 4: 4-10.

NOWAK K.W., ZIELINSKA M., WASZKIELIS K.M. 2019. *The effect of ultrasound and freezing/thawing treatment on the physical properties of blueberries*. Food Science and Biotechnology, 28: 741-749.

RAHMAN S. 1995. *Food Properties Handbook*. CRC Press Inc, Boca Raton.

SCHMIDT E.L., KLOCKER K., FLACKE N., STEIMLE F. 1998. *Applying the transcritical CO_2 process to a drying heat pump*. International Journal of Refrigeration, 21(3): 202-211.

SIUCINSKA K., KONOPACKA D., MIESZCZAKOWSKA-FRAC M., POLUBOK A. 2016a. *The effects of ultrasound on quality and nutritional aspects of dried sour cherries during shelf-life*. LWT – Food Science and Technology, 68: 168-173.

SIUCINSKA K., MIESZCZAKOWSKA-FRAC M., POLUBOK A., KONOPACKA D. 2016b. *Effects of ultrasound assistance on dehydration processes and bioactive component retention of osmo-dried sour cherries*. Journal of Food Science, 81(7): C1654-C1661.

STANISZEWSKA I., DZADZ L., XIAO H.W., ZIELINSKA M. 2020. *Evaluation of storage stability of dried cranberry powders based on the moisture sorption isotherms and glass transition temperature*. Drying Technology, doi: 10.1080/07373937.2020.1771362.

STANISZEWSKA I., STASZYNSKI S., ZIELINSKA M. 2019. *Application of sonication and freezing as initial treatments before microwave-vacuum drying of cranberries*. Technical Sciences, 22(2): 151-167.

STOJANOVIC J., SILVA J.L. 2007. *Influence of osmotic concentration, continuous high frequency ultrasound and dehydration on antioxidants, colour and chemical properties of rabbiteye blueberries*. Food Chemistry, 101: 898-906.

WRAY D., RAMASWAMY H.S. 2013. *Microwave-osmotic dehydration of cranberries under continuous flow medium spray conditions*. International Journal of Microwave Science and Technology, 2013: 1-11.

WRAY D., RAMASWAMY H.S. 2015. *Development of a microwave–vacuum-based dehydration technique for fresh and microwave–osmotic (MWODS) pretreated whole cranberries (Vaccinium macrocarpon)*. Drying Technology, 33(7): 796-807.

YOGENDRARAJAH P., SAMAPUNDO S., DEVLIEGHERE F., SAEGER S., MEULENAER B. 2015. *Moisture sorption isotherms and thermodynamic properties of whole black peppercorns (Piper nigrum L.)*. LWT – Food Science and Technology, 64(1): 177-188.

ZHENG Y., WANG C.Y., WANG S.Y., ZHENG W. 2003. *Effect of high-oxygen atmospheres on blueberry phenolics, anthocyanins, and antioxidant capacity*. Journal of Agricultural and Food Chemistry, 51: 7162-7169.

ZIELINSKA M., MARKOWSKI M. 2012. *Color Characteristics of Carrots: Effect of Drying and Rehydration*. International Journal of Food Properties, 15: 450-466.

ZIELINSKA M., MARKOWSKI M. 2018. *Effect of microwave-vacuum, ultrasonication, and freezing on mass transfer kinetics and diffusivity during osmotic dehydration of cranberries*. Drying Technology, 36(10): 1158-1169.

ZIELINSKA M., MARKOWSKI M., ZIELINSKA D. 2019. *The effect of freezing on the hot air and microwave vacuum drying kinetics and texture of whole cranberries*. Drying Technology, 37(13): 1714-1730.

ZIELINSKA M., ROPELEWSKA E., MARKOWSKI M. 2017. *Thermophysical properties of raw, hot-air and microwave-vacuum dried cranberry fruits (Vaccinium macrocarpon)*. LWT - Food Science and Technology, 85: 204-211.

ZIELINSKA M., ROPOLEWSKA E., ZAPOTOCZNY P. 2018a. *Effects of freezing and hot air drying on the physical, morphological and thermal properties of cranberries (Vaccinium macrocarpon)*. Food and Bioproducts Processing, 110: 40-49.

ZIELINSKA M., SADOWSKI P., BLASZCZAK W. 2015. *Freezing/thawing and microwave assisted drying of blueberries (Vaccinium corymbosum L.)*. LWT - Food Science and Technology, 62(1, 2): 555-563.

ZIELINSKA M., ZIELINSKA D. 2019. *Effects of freezing, convective and microwave-vacuum drying on the content of bioactive compounds and color of cranberries*. LWT - Food Science and Technology, 104: 202-209.

ZIELINSKA M., ZIELINSKA D., MARKOWSKI M. 2018b. *The effect of microwave-vacuum pretreatment on the drying kinetics, color and the content of bioactive compounds in osmo-microwave-vacuum dried cranberries (Vaccinium macrocarpon)*. Food and Bioprocess Technology, 11: 585-602.

Technical Sciences, 2020, 23(2), 175–184

UNIWERSYTET WARMIŃSKO-MAZURSKI W OLSZTYNIE

Quarterly peer-reviewed scientific journal
ISSN 1505-4675
e-ISSN 2083-4527
TECHNICAL SCIENCES
Homepage: www.uwm.edu.pl/techsci/

DOI: https://doi.org/10.31648/ts.6119

ANALYSIS OF THE INFLUENCE OF UV LIGHT EXPOSURE TIME ON HARDNESS AND DENSITY PROPERTIES OF SLA MODELS

***Bartosz Pszczółkowski*[1], *Łukasz Dzadz*[2]**

[1]ORCID: 0000-0002-7985-9488
Department of Materials and Machines Technology
Faculty of Technical Sciences
University of Warmia and Mazury in Olsztyn

[2]ORCID: 0000-0002-5338-5931
Department of Systems Engineering
Faculty of Technical Sciences
University of Warmia and Mazury in Olsztyn

Received 16 November 2020, accepted 8 December 2020, available online 9 December 2020.

K e y w o r d s: SLA, light-curing resin, hardness, density, UV.

A b s t r a c t

The article analysis the effect of exposure to ultraviolet light on the hardening process of the model made in the SLA technology. Research samples were created with the SLA additive technique using a 10s exposure time. In this experiment, the change in item hardness and density over a 96-hour period was analysed. Light exposure time for details of an item made in SLA technology results in an increase in hardness. At the same time are observed, changes in density and stabilization of both parameters with increasing exposure time to UV light.

Correspondence: Łukasz Dzadz, Katedra Inżynierii Systemów, Wydział Nauk Technicznych, Uniwersytet Warmińsko-Mazurski, ul. Heweliusza 14, 10-718 Olsztyn, e-mail: lukasz.dzadz@uwm.edu.pl.

Introduction

Continuous progress and demand for manufacturing unique or short-series items have led to the development of incremental manufacturing techniques. These technologies consist of producing an item by applying one layer after another and bonding them to create the whole model. One of these methods is 3D stereolithographic printing technology or "SLA" for short. This is a new technology that is being used increasingly extensively. It was developed in the early 1980s by Hideo Kodama, a Japanese researcher, who invented it and created the first model based on stereolithography. For this purpose, he used ultraviolet light to cure photosensitive polymers (Bartolo, Gibson 2011, *The Ultimate Guide*… 2017). Since then, there have been rapid developments in the field of positioning and control. This allowed for improvements in this method and the creation of 3D printers for printing models from light-curing polymers.

Stereolithography (SLA) is becoming an increasingly popular low-budget additive manufacturing technology. It has gained particular recognition among artists and engineers as it provides excellent dimensional accuracy and good overall quality of the item compared to its direct and most popular competitor, fused deposition modelling (FDM) (Redwood et al. 2017, Schmidleithner, Kalaskar 2018). Despite the early invention of the first 3D printers (Hull 1998), SLA was not as successful as FDM printers, due to the high cost of consumables, their low availability and durability. At present, multiple problems have been solved and many manufacturers have a wide offer of SLA printing resins for various applications. As a result, models produced with this technology are being increasingly used for mechanical applications due to competitive prices (Cosmi, Dal Maso 2020, Małek et al. 2019).

In SLA technology, an item is produced by bonding successive layers by selective curing of the liquid photopolymerising resin with an actuator in the form of an oriented light wave. The generated light polymerizes a specific network of points forming a model. The liquid material fills a fixed container whose size depends on the working area of the printer. The bottom of the container is formed by a film with a low absorption coefficient. The first layer of the model is fixed to a moving working platform moving in the Z-axis in the direction opposite to gravity. During the whole process, the model is partially immersed in liquid resin at a depth of several millimetres. The immersion is limited by the size of the tank and the amount of resin needed for the process.

Once an individual layer is cured, the printing platform is lifted, which allows the next layer to be peeled off the transparent bottom and fill the space between the light actuator and the already formed layer of the growing model. This process is time-consuming and causes the formation of adhesion forces which may damage the part, hence the need for careful choice of model manufacturing orientation and modelling the support to allow for proper model growth (Liravi

et al. 2015, MELCHELS et al. 2010, PAN et al. 2017, WANG et al. 2018). Greater mechanical strength is achieved by curing by treating the manufactured part with light with a wavelength initiating the photopolymerisation at the end of the printing process (SUN et al. 2008, ZGURIS 2016). The main advantages of stereolithography-based production in comparison with other low-budget 3D printing technologies, e.g. FDM, include high dimensional accuracy, low roughness of the model surface, higher printing speed and isotropic material behaviour (COSMI, DAL MASO 2020).

In addition, the resins used in the manufacturing process are characterised by a wide range of visible light permeability, which enables their use in optics. The finished models can be subjected to additional mechanical processing.

As in most additive technologies, and also in SLA, the models may become distorted during manufacturing, which is, however, insignificant for most types of resins and occurs almost exclusively in the final phase of lighting the finished model (FUH et al. 1997, JACOBS 1992). Some applications preparing a model for SLA manufacturing can predict and compensate for this uniform contraction of the polymerised material (HUANG et al. 2015). Moreover, SLA parts are not porous but waterproof. This guarantees much more control over the internal geometry, mass properties and general characteristics of the printed materials (GIBSON et al. 2010). According to some studies, the physical properties of SLA parts are anisotropic (CHANTARAPANICH et al. 2013, DULIEU-BARTON, FULTON 2000) while more recent studies have confirmed the complete isotropy of the physical properties of these parts (DIZON et al. 2018, DULIEU-BARTON, FULTON 2000, *White paper*… 2018, HAGUE et al. 2004).

The aim of the study is to assess the effect of the exposure time to UV light on the hardness and density of models made in the SLA technology. Determining the influence of the exposure time to UV radiation on the hardness and density of the detail informs about its readiness for use.

Materials and methods

The samples used for the tests were cubes with an edge of 10 mm (Fig. 1). They were made in SLA technology from light-cured resin cross-linking in the light wave range of approx. 405 nm. The exposure time for a single layer was 10 s and its thickness was 50 μm. The ambient temperature during printing was 22°C. The samples were prepared using an Anycubic Photon S Sla printer (Anycubic).

After printing, the samples were treated with light of 400 nm wavelength in a darkened chamber. The lighting time was 1, 4, 8, 12, 24, 48, 64, 72, 96 hours, respectively. The ambient temperature was 22°C. After each irradiation session, the density and hardness of details were measured.

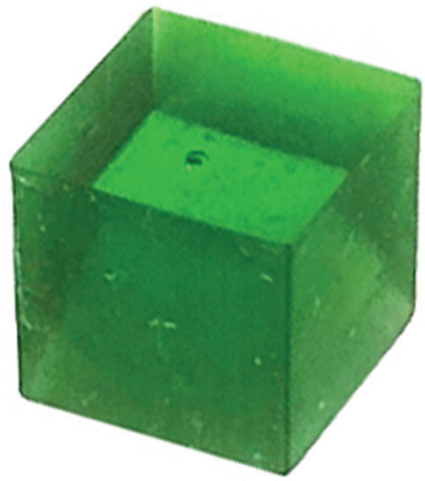

Fig 1. Sample model

The hardness of manufactured parts was measured on the Brinell scale using the "Innovatest Nexus 703A" hardness-meter with an HB 358 N main load value. The measurement was carried out in 10 repetitions.

The density measurement was carried out with the HumiPyc™ Model 1 gas pycnometer (InstruQuest Inc. Scientific Instruments R&D, USA). Helium of purity class 5.0 was used as the measurement gas. Measurements were made at 22 ±0.1°C and 220 kPa. Samples were placed in the measuring chamber where their temperature was stabilised for about 10 minutes. Measurement was made with an accuracy of 0.00001 g/cm^3. Weight was measured using RADWAG AS 62 analytical scales with an accuracy of 0.00001 g. Volume and weight measurements were repeated five times.

Statistica 13.1 software (StatSoft Inc., Tulsa, Oklahoma, USA) was used for statistical analysis of the results. a non-parametric Kruskal-Wallis test was used to assess the differences between the results obtained during the study (at significance level $p = 0.05$).

Results and discussion

Figure 2 shows the hardness of the manufactured parts as a function of the irradiation time. It can be seen that the hardness of the polymer increases as a function of changes in irradiation time. The conducted statistical analysis showed that there are significant statistical differences in parts' hardness depending on the irradiation time (Tab. 1). The p values for irradiation times at which statistically significant differences in hardness were found are marked

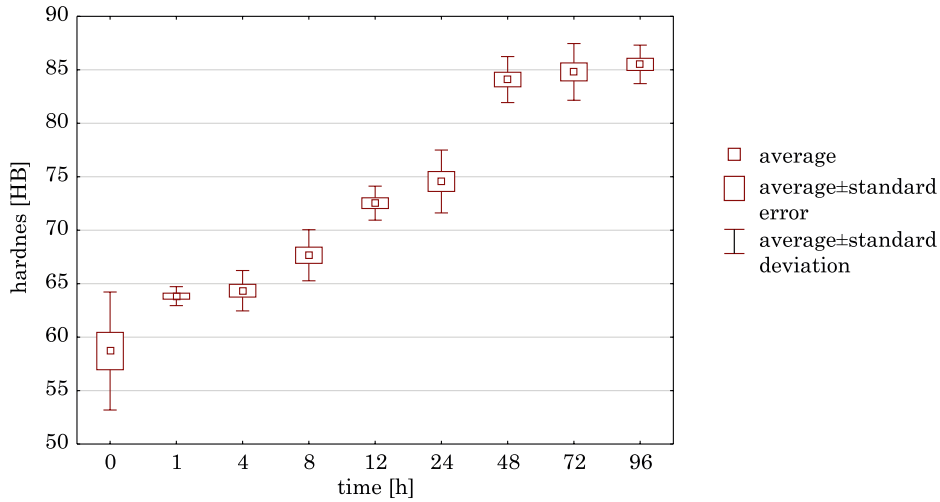

Fig. 2. Changes in element hardness as a function of irradiation time

Table 1

p value for multiple (bilateral) comparisons; Hardness (Sheet1) Independent variable (grouping): Time Kruskal-Wallis test: H (8, *N* = 90) = 81.22954 *p* = .0000

Exposure time [h] ↓→	0	1	4	8	12	24	48	72	96
0		1.000000	1.000000	1.000000	0.037613	0.008962	0.000002	0.000001	0.000000
1	1.000000		1.000000	1.000000	0.387086	0.119764	0.000088	0.000044	0.000008
4	1.000000	1.000000		1.000000	0.684564	0.227735	0.000237	0.000121	0.000023
8	1.000000	1.000000	1.000000		1.000000	1.000000	0.043082	0.026011	0.007449
12	0.037613	0.387086	0.684564	1.000000		1.000000	1.000000	0.767199	0.305621
24	0.008962	0.119764	0.227735	1.000000	1.000000		1.000000	1.000000	0.887518
48	0.000002	0.000088	0.000237	0.043082	1.000000	1.000000		1.000000	1.000000
72	0.000001	0.000044	0.000121	0.026011	0.767199	1.000000	1.000000		1.000000
96	0.000000	0.000008	0.000023	0.007449	0.305621	0.887518	1.000000	1.000000	

in red. No statistically significant differences in hardness were found between irradiation times in the range from 0 to 8 hours. A similar trend was observed for irradiation times from 12 to 96 h.

The change of parts hardness in the initial irradiation phase could be affected by polymerisation shrinkage, accompanying stress and incomplete conversion of double bonds (DAVIDSON, DE GEE 1984, DAVIDSON, FEILZER 1997). The increasing material hardness may also be related to the continuous cross--linking of the material under the influence of UV light. The degree of polymerisation in cross-linked polymer systems plays a potentially important role

in determining the final physical and mechanical properties of the material. (SOH, YAP 2004). During the first 48 hours of irradiation, the hardness increases and then stabilizes at 84.8 ±0.75 HB, which may be indicative of the end of the cross-linking process. It is worth noting that the initial average material hardness is 58.7 HB with a large standard deviation of about 5.2 HB. a lower cross-linking degree accompanied by higher polydispersity of the material may result in lower hardness, low wear resistance, reduced colour intensity, reduced stability, increased water absorption rate and higher solubility in organic media (FAN et al. 1987, PEARSON, LONGMAN 1989, SHORTALL et al. 1995, VARGAS et al. 1998, VENHOVEN et al. 1993).

Figure 3 shows changes in the density of details as a function of irradiation time. There were no statistically significant differences between the hardness of details for particular irradiation times. In the initial phase, the increase in the sample density may be related to polymerisation shrinkage of the material as a result of initial irradiation. It is accompanied by stress and incomplete conversion of double bonds (DAVIDSON, DE GEE 1984, DAVIDSON, FEILZER 1997). In the period between the 8th and 24th hours of irradiation, a decrease in density was observed, which is the result of the branching of chains already formed during the crosslinking process. The branching of chains can result in a reduction in the packing of carbon atoms in the polymer structure and an increase in the average distances between atoms. This may cause a decrease in the density of the material after eight hours of exposure. However, if the density increases after 24 hours of exposure, several different mechanisms may take place. The resulting branched chains with active terminal groups may undergo such processes as chain closing, recombination, radical transfer and

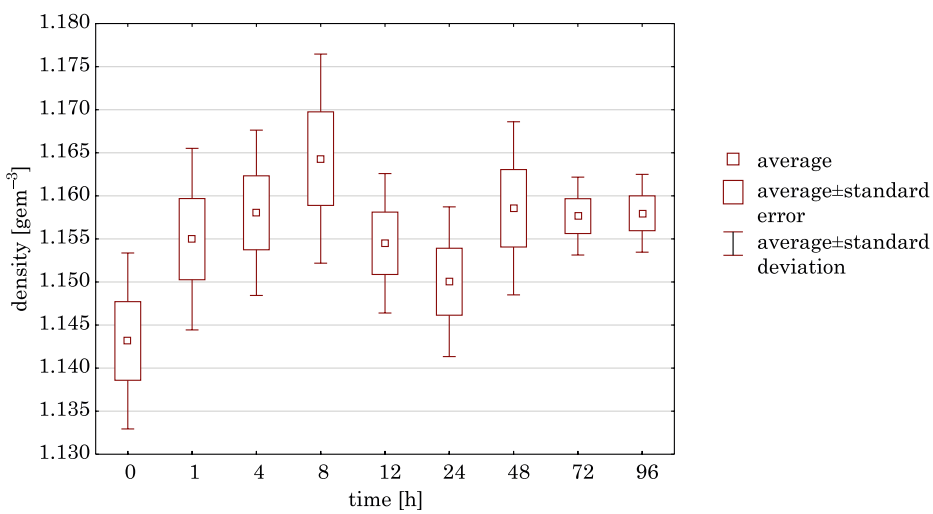

Fig. 3. Changes in element density as a function of irradiation time

linking to another chain. Especially the latter process may cause another increase in density observed after 24 hours of irradiation. The correlated increase in material hardness also supports the hypothesis that such a mechanism occurs. However, none of the above-mentioned processes can be excluded. It is also probable that a radical polymerisation reaction with chain transfer occurs (BOCIONG et al. 2018, CRAMER, BOWMAN 2001, PODGÓRSKI et al. 2015).

Comparison of the trends of changes in hardness and density of the analysed models allows for unequivocally stating that they assume a consistent conservative trend in particular measurement intervals (Fig. 2 and Fig. 3). The point of refraction between the 8^{th} and 12^{th} hour of irradiation provides an exception, where the density decreases from 1.1643 $g \cdot cm^{-3}$ to 1.1544 $g \cdot cm^{-3}$ with further stabilisation of the change tendency observable in subsequent time intervals. During irradiation, the hardness increases by about 24.5 HB and the density by 0.0148 $g \cdot cm^{-3}$ in relation to measurements in samples before irradiation.

It is worth mentioning that hardness is directly related to increasing material density. The values of both parameters assume a growth trend in the initial eight curing hours which may be caused by material shrinkage. At this stage, both parameters depend, among others, on the mutual distance of double bonds (CZECH, MINCIEL 2015, DAVIDSON, DE GEE 1984, DAVIDSON, FEILZER 1997). In his research on curable light polymers, LE XUAN (1993) confirmed the relationship between the time of exposure to UV radiation and the increase in hardness which was attributed to the increase in the crosslinking density of the polymer (LE XUAN, DECKER 1993).

Polymerisation of methacrylate monomers in composite resins creates a strongly cross-linked structure. However, the monomer conversion is never completed and always contains significant amounts of lateral double bonds (FERRACANE et al. 1997). These suspended double bonds can influence the crosslinking density in composites by reacting with propagating radicals to form crosslinking in primary or secondary cycles. a transverse bond is formed when a radical reacts with a double side bond on another kinetic chain. a primary cycle is created when a radical reacts with a double bond hanging on its own kinetic chain. a secondary cycle is formed when a radical reacts with a double bond hanging from another kinetic chain with which it is already cross-linked. Primary cyclisation reactions form microgels and introduce some heterogeneity in the polymer network with loosely cross-linked areas and more strongly cross-linked areas of the microgel coexisting next to one another (ANSETH, BOWMAN 1994, BOOTS, PANDEY 1984). This is confirmed by the behaviour of the samples in the initial irradiation period, which is evidenced by a linear increase in the hardness parameter of the irradiated material. Such cyclisation would promote an increased local conversion because it does not reduce the mobility of the system as much as cross-linking. However, cyclisation may also lead to a reduction in effective cross-linking density, as cycles do not have a significant impact

on the overall crosslinked structure. Reducing the effective crosslinking density of the cured resin would lead to a reduction in its mechanical strength, resistance to solvents and glass transition temperature (ANSETH, BOWMAN 1994, BOOTS, PANDEY 1984), which is responsible for changes in material density during the entire curing process and indirectly translates into hardness.

Conclusions

This study confirmed that material hardness increases with an increase in irradiation time. No statistically significant influence of the irradiation time on the density of manufactured parts was observed. The observed trends indicate that the hardness and density values stabilize after 48 hours. It thus seems reasonable to accept 48 hours of irradiation time with a 400 nm wavelength light as a criterion for element strength stability.

It should be noted that elements manufactured using SLA technology are subject to shrinkage, which may result in the deformation of the elements. However, its extent is very limited, which is confirmed by only a slight change in the density of the parts and the lack of a statistically significant influence of the irradiation time on density. It should also be noted that the exposure time has a positive effect on hardness and density homogeneity in individual elements, as evidenced by the decreasing standard deviation.

ACKNOWLEDGEMENT

This study was partially supported by the University of Warmia and Mazury in Olsztyn (grant No. 16.610.001-300).

References

ANSETH K.S., BOWMAN C.N. 1994. *Kinetic Gelation model predictions of crosslinked polymer network microstructure*. Chemical Engineering Science, 49(14): 2207–2217, doi:10.1016/0009-2509(94)E0055-U.

BARTOLO P.J., GIBSON I. 2011. *Stereolithography: materials, processes and applications*. Springer Science & Business Media, doi: 10.1007/978-0-387-92904-0.

REDWOOD B., SCÖFFER F., GARRET B. 2017. *The 3D Printing Handbook: Technologies, design and applications*. 3D Hubs B.V., Amsterdam.

BOCIONG K., KRASOWSKI M., SZCZESIO A., ANYSZKA R., KALICKA K. 2018. *Modyfikacja światłoutwardzalnego kompozytu stomatologicznego wybranymi poliedrycznymi oligomerycznymi silseskwioksanami*. Polimery, 7–8: 515–523.

BOOTS H.M.J., PANDEY R.B. 1984. *Qualitative percolation study of free-radical cross-linking polymerization*. Polymer Bulletin, 11(5): 415–420, doi: 10.1007/BF00265480.

Chantarapanich N., Puttawibul P., Sitthiseripratip K., Sucharitpwatskul S., Chanta-weroad S. 2013. *Study of the mechanical properties of photo-cured epoxy resin fabricated by stereolithography process*. Songklanakarin Journal of Science and Technology, 35(1): 91–98.

Cosmi F., Dal Maso A. 2020. *A mechanical characterization of SLA 3D-printed specimens for low-budget applications*. Materials Today: Proceedings, doi: 10.1016/j.matpr.2020.04.602.

Cramer N.B., Bowman C.N. 2001. *Kinetics of thiol-ene and thiol-acrylate photopolymerizations with real-time Fourier transform infrared*. Journal of Polymer Science, Part A, Polymer Chemistry, 39(19): 3311–3319, doi: 10.1002/pola.1314.

Czech Z., Minciel E. 2015. *Światłoutwardzalne kompozyty zawierające akrylowane żywice wielofunkcyjne: skrócony przegląd literaturowy*. Aparatura Badawcza i Dydaktyczna, 20: 270–275.

Davidson C.L., de Gee A.J. 1984. *Relaxation of Polymerization Contraction Stresses by Flow in Dental Composites*. Journal of Dental Research, 63(2): 146–148, doi: 10.1177/00220345840630021001.

Davidson C.L., Feilzer A.J. 1997. *Polymerization shrinkage and polymerization shrinkage stress in polymer-based restoratives*. Journal of Dentistry, 25(6): 435–440, doi: 10.1016/S0300-5712(96)00063-2.

Dizon J.R.C., Espera A.H., Chen Q., Advincula R.C. 2018. *Mechanical characterization of 3D-printed polymers*. Additive Manufacturing, 20: 44–67, doi: 10.1016/j.addma.2017.12.002.

Dulieu-Barton J.M., Fulton M.C. 2000. *Mechanical properties of a typical stereolithography resin*. Strain, 36(2): 81–87, doi: 10.1111/j.1475-1305.2000.tb01177.x.

Fan P.L., Wozniak W.T., Reyes W.D., Stanford J.W. 1987. *Irradiance of visible light-curing units and voltage variation effects*. Journal of the American Dental Association, 115(3): 442–445, doi: 10.14219/jada.archive.1987.0252.

Ferracane J.L., Mitchem J.C., Condon J.R., Todd R. 1997. *Wear and marginal breakdown of composites with various degrees of cure*. Journal of Dental Research, 76(8): 1508–1516, doi: 10.1177/00220345970760081401.

White Paper - Validating Isotropy in SLA 3D Printing. 2018. Formlabs, Somerville.

The Ultimate Guide to Stereolithography (SLA) 3D Printing. 2017. Formlabs Inc. March, 1–23, https://formlabs.com/blog/ultimate-guide-to-stereolithography-sla-3d-printing/.

Fuh J.Y.H., Chooo Y.S., Lu L., Nee A.Y.C., Wong Y.S., Wang W.L., Miyazawa T., Ho S.H. 1997. *Post-cure shrinkage of photo-sensitive material used in laser lithography process*. Journal of Materials Processing Technology, 63(1–3): 887–891, doi: 10.1016/S0924-0136(96)02744-6.

Hague R., Mansour S., Saleh N., Harris R. 2004. *Materials analysis of stereolithography resins for use in Rapid Manufacturing*. Journal of Materials Science, 39(7): 2457–2464, doi: 10.1023/B:JMSC.0000020010.73768.4a.

Huang Q., Zhang J., Sabbaghi A., Dasgupta T. 2015. *Optimal offline compensation of shape shrinkage for three-dimensional printing processes*. IIE Transactions (Institute of Industrial Engineers), 47(5): 431–441, doi: 10.1080/0740817X.2014.955599.

Hull C.W. 1998. *Method for production of three-dimensional objects by stereolithography*. Patent No. 5,762,856, https://patents.google.com/patent/US5444220A/en.

Gibson I., Rosen D.W., Stucker B. 2010. *Additive Manufacturing Technologies Rapid Prototyping to Direct Digital Manufacturing*. CIRP Encyclopedia of Production Engineering. Springer, doi: 10.1007/978-3-662-53120-4_16866.

Jacobs P.F. 1992. *Rapid prototyping & manufacturing – Fundamentals of stereolithography*. Journal of Manufacturing Systems, 12(5), doi: 10.1016/0278-6125(93)90311-g.

Le Xuan H., Decker C. 1993. *Photocrosslinking of acrylated natural rubber*. Journal of Polymer Science, Part A, Polymer Chemistry, 31(3): 769–780, doi: 10.1002/pola.1993.080310323.

Liravi F., Das S., Zhou C. 2015. *Separation force analysis and prediction based on cohesive element model for constrained-surface Stereolithography processes*. CAD Computer Aided Design, 69: 134–142, doi: 10.1016/j.cad.2015.05.002.

Małek E., Miedzińska D., Popławski A., Szymczyk W. 2019. *Application of 3D printing technology for mechanical properties study of the photopolymer resin used to print porous structures*. Technical Sciences, 2(22): 183–194, doi: 10.31648/ts.4584.

MELCHELS F.P.W., FEIJEN J., GRIJPMA D.W. 2010. *A review on stereolithography and its applications in biomedical engineering*. Biomaterials, 31(24): 6121–6130, doi: 10.1016/j.biomaterials.2010.04.050.

PAN Y., HE H., XU J., FEINERMAN A. 2017. *Study of separation force in constrained surface projection stereolithography*. Rapid Prototyping Journal, 23(2): 353–361, doi: 10.1108/RPJ-12-2015-0188.

PEARSON G.J., LONGMAN C.M. 1989. *Water sorption and solubility of resin-based materials following inadequate polymerization by a visible-light curing system*. Journal of Oral Rehabilitation, 16(1): 57–61, doi: 10.1111/j.1365-2842.1989.tb01317.x.

PODGÓRSKI M., BECKA E., CLAUDINO M., FLORES A., SHAH P.K., STANSBURY J.W., BOWMAN C.N. 2015. *Ester-free thiol-ene dental restoratives*. Part B. *Composite development*. Dental Materials, 31(11): 1263–1270, doi: 10.1016/j.dental.2015.08.147.

SCHMIDLEITHNER C., KALASKAR D.M. 2018. *Stereolithography*. 3D Printing. InTech, doi: 10.5772/intechopen.78147.

SHORTALL A.C., WILSON H.J., HARRINGTON E. 1995. *Depth of cure of radiation - activated composite restoratives - Influence of shade and opacity*. Journal of Oral Rehabilitation, 22(5): 337–342, doi: 10.1111/j.1365-2842.1995.tb00782.x.

SOH M.S., YAP A.U.J. 2004. *Influence of curing modes on crosslink density in polymer structures*. Journal of Dentistry, 32(4): 321–326, doi: 10.1016/j.jdent.2004.01.012.

SUN Q., RIZVI G.M., BELLEHUMEUR C.T., GU P. 2008. *Effect of processing conditions on the bonding quality of FDM polymer filaments*. Rapid Prototyping Journal, 14(2): 72–80, doi: 10.1108/13552540810862028.

VARGAS M.A., COBB D.S., SCHMIT J.L. 1998. *Polymerization of composite resins: Argon laser vs conventional light*. Operative Dentistry, 23(2): 87–93, https://europepmc.org/article/med/9573794.

VENHOVEN B.A.M., DE GEE A.J., DAVIDSON C.L. 1993. *Polymerization contraction and conversion of light-curing BisGMA-based methacrylate resins*. Biomaterials, 14(11): 871–875, doi: 10.1016/0142-9612(93)90010-Y.

WANG J., DAS S., RAI R., ZHOU C. 2018. *Data-driven simulation for fast prediction of pull-up process in bottom-up stereo-lithography*. CAD Computer Aided Design, 99: 29–42, doi: 10.1016/j.cad.2018.02.002.

ZGURIS Z. 2016. *How Mechanical Properties of Stereolithography 3D Prints are Affected by UV Curing*. Formlabs White Paper, formlabs.com, https://archive-media.formlabs.com/upload/How-Mechanical-Properties-of-SLA-3D-Prints-Are-Affected-by-UV-Curing.pdf.

Technical Sciences, 2020, 23(2), 185–198

UNIWERSYTET WARMIŃSKO-MAZURSKI W OLSZTYNIE

Quarterly peer-reviewed scientific journal
ISSN 1505-4675
e-ISSN 2083-4527
TECHNICAL SCIENCES
Homepage: www.uwm.edu.pl/techsci/

DOI: https://doi.org/10.31648/ts.5695

A CONTROLLER FOR BRUSHLESS DIRECT CURRENT ELECTRIC MOTORS PART 1: ELECTRICAL AND ELECTRONIC DESIGN

Zenon Syroka

ORCID: 0000-0003-3318-8495
Technical Science Department
University of Warmia & Mazury

Received 24 July 2020, accepted 1 December 2020, available online 3 December 2020.

Keywords: Digital control, motor controller, electric and hybrid vehicles, brushless motors, microcontroller.

Abstract

A universal controller for brushless direct current (BLDC) motors was designed in the presented article. The system is controlled from the user console where operating parameters are set by the user. Signals are transmitted by cables to microcontrollers which drive and monitor electric motors. Microprocessors communicate via a data bus. The controller contains the user console module and the motor control module. The user console module generates commands, and motors are controlled and monitored by the control module. Motor control modules operate independently, and each brushless motor has a dedicated control module. Brushless motors can be controlled in bipolar or unipolar mode. The control method is selected by the operator. The user console and motor controllers communicate via the I²C bus.

Introduction

The article consists of two parts. The first part describes the electronic and electrical design of the motor controller, and the second part presents the applied software. The described controller for brushless motors has been designed and patented by Z. SYROKA and K. KRAJEWSKI (patent No. P431380, filing date: 4 October 2019).

Correspondence: Zenon Syroka, Katedra Elektrotechniki, Energetyki, Elektroniki i Automatyki, Wydział Nauk Technicznych, Uniwersytet Warmińsko-Mazurski, ul. Oczapowskiego 11, 10-719 Olsztyn, e-mail: zenon.syroka@uwm.edu.pl, syrokaz@onet.eu.

Industrial machines, vehicles, power tools and household appliances have motor drive elements that power mechanical components. The popularity of electric cars has been increasing in the 21st century. Batteries and motors are the key components of electric vehicles. Batteries are positioned at the bottom of the chassis to lower the vehicle's center of gravity. The motor is located in the front or at the back of the vehicle (Tesla Model S). The motors in electric cars are powered by direct (DC) or alternating current (AC). Brushless motors are one type of DC motors. Rapid advances in electrical and power engineering have introduced novel components to brushless motors, including thyristors, diodes and MOSFET transistors. Electronic subassemblies can turn power supply on and off hundreds or even thousands of times within one second. In electric bicycles, a brushless motor is placed inside the wheel hub. Power is transferred to the wheel, which reduces the physical effort associated with pedaling by 50%.

This article discusses a controller for brushless DC motors that are mounted inside the wheels of land vehicles. The motor is controlled by the user via the user console. The user can change motor speed, driving direction and deploy the electric braking system. The controller controls the steering system, the drivetrain and the braking system. Brushless DC motors can be controlled in unipolar and bipolar mode.

Structure and the basic working principle of a brushless DC motor

A brushless DC (BLDC) motor has the following characteristics:

– two BLCD motors are mounted inside wheel hubs;

– motors operate independently; therefore, the speed and direction of rotation can be controlled independently in each motor;

– the motor controller is controlled from the user console;

– different wheel combinations can be used to turn a vehicle;

– the motors are powered by a battery installed in the vehicle;

– motor operation is controlled;

– BLDC motors can be controlled in bipolar and unipolar mode.

The system is controlled from the user console where operating parameters are set by the user. Signals are transmitted by cables to microcontrollers which drive and monitor BLDC motors. Microprocessors communicate via a data bus. The controller contains the user console module and the motor control module. The user console module generates commands, and motors are controlled and monitored by the control module. Motor control modules operate independently, and each brushless motor has a dedicated control module. Brushless motors can be controlled in bipolar and unipolar mode. The control mode is selected by the

user. The user console and the motor controller communicate via the I²C bus. A simplified diagram of the designed motor control system is presented in Figure 1.

The master microcontroller (*2*) reads the command input from the user console (*1*), processes and converts the data into a signal that is transmitted to the left motor microcontroller (*3*) and the right motor microcontroller (*7*). The left motor microcontroller (*3*) and the right motor microcontroller (*7*) process the data transmitted by the master microcontroller (*2*) and the data from the left sensor (*6*) and the right sensor (*10*) which describe the position of the rotor. The left sensor (*6*) and the right sensor (*10*) monitor the rotor's position during operation. The information about the rotor's position is transmitted to the left motor (5) microcontroller (3) and the right motor (*9*) microcontroller (*7*). The left motor (*5*) microcontroller (*3*) and the right motor (*9*) microcontroller (*7*) transmit signals to the three-phase bridge of the left motor (*4*) and the three-phase bridge of the right motor (*8*), where electric current is passed through the winding of the left (*5*) and right (*9*) BLCD motor according to a given commutation sequence.

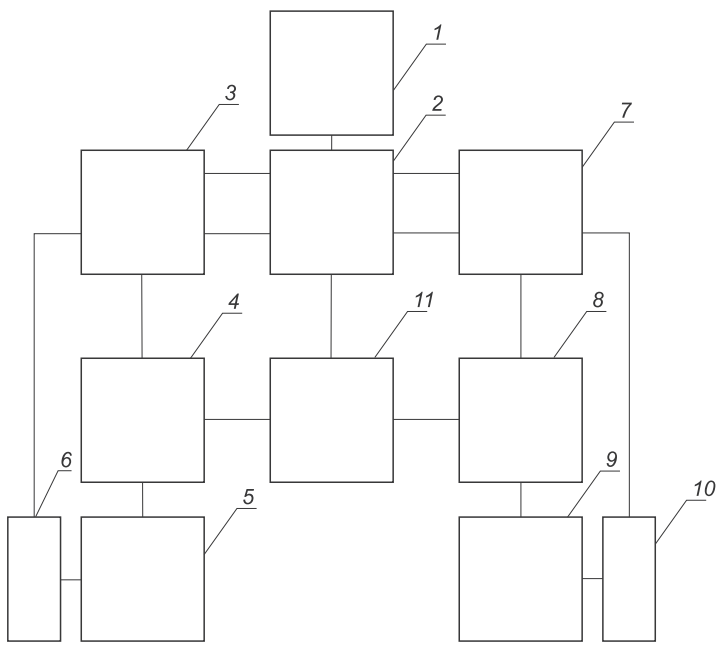

1 – control circuit, *2* – master microcontroller, *3* – left motor microcontroller, *4* – left motor three-phase bridge, *5* – left BLDC motor, *6* – left sensor, *7* – right motor microcontroller, *8* – right motor three-phase bridge, *9* – right BLDC motor, *10* – right sensor, *11* – power supply

Fig. 1. Block diagram of the designed controller for BLDC motors

Electrical and electronic design of the motor controller

A controller for driving two BLDC motors has numerous electrical and electronic components, including microcontroller integrated circuits, brushless motors, MOSFET transistors and drivers, a voltage converter, and a battery.

Characteristics of a BLDC motor

Brushless motors rely on electronic commutation to turn stator windings on and off. Stator windings are supplied with current and voltage pulses. In motors with electronic commutation:

– pulses are supplied to stator coils by inverters;

– stator poles are energized sequentially depending on the rotor's position;

– the stator does not have winding, and it is composed of permanent magnets.

Brushless DC motors are also known as permanent magnet synchronous motors with trapezoidal electromotive force (EMF). The distribution of magnetic induction produces trapezoidal EMF. The transistor inverter supplies stator coils with rectangular pulses. Each phase current flows through 1/3 of the phase (120°) in the positive direction and 1/3 of the phase in the negative direction, and current pulses are separated by 60°.

The rotor has a ferromagnetic core composed of metal supports mounted outside the housing. Three-phase star-connected windings are positioned inside grooves on the face of the rotor. The rotor is composed of permanent magnets, metal supports and solid steel components. The types of rotors are applied:

– magnets with diagonal or radial magnetization are mounted on the surface of the rotor;

– magnetic steel plates arranged in a perpendicular direction to the rotor's axis.

The first variant is characterized by a larger air gap, perpendicular distribution of magnetic induction and lower induced voltage in winding. The second variant improves sinusoidal flux distribution in the air gap. When permanent magnets are used, excess power is lost mainly in the rotor, and it is easy to evacuate. The elimination of brushes and mechanical armature increases the motor's reliability and reduces mechanical losses. Brushless DC motors are characterized by high material use and high efficiency.

Brushless motors can be divided into two categories in terms of magnetic field generation:

– motors with permanent magnets with trapezoidal or sinusoidal EMF waveforms;

– switched reluctance motors without permanent magnets.

In motors with trapezoidal EMF, current is supplied to two stator poles and the position of the magnetomotive force vector changes rapidly due to repeatable phase switching. The motor's performance is enhanced when magnetic induction has trapezoidal distribution. The moment when the inverter valve should be turned on is indicated by the location sensor. Hall effect sensors are often used for this purpose. Sinusoidal waveforms are controlled in velocity control zones. Instantaneous current in windings is controlled by a pulse width modulation (PWM) signal to obtain a sinusoidal output wave.

Current pulses can be supplied to motor windings in:

– bipolar mode,

– unipolar mode.

Brushless DC motors have the following advantages:

– high start-up torque,

– long life,

– low weight relative to other DC motors,

– precise speed control,

– rigid mechanical configuration.

Brushless DC motors have the following limitations:

– an expensive microprocessor circuit is required to control commutation and rotor position;

– smooth motion is difficult to produce at low speeds.

Connection diagram for two BLDC motors

The controller relies on two BLDC motors – the left motor and the right motor. The motors have three stator windings, and each motor is connected individually to the control system. The motors have three-phase inverter outputs and a sensor system. The three-phase bridge inverter supplies sequence current to the winding and creates a magnetic field around the conductor, which sets the rotor with permanent magnets into motion. The rotor's position is controlled by a sensor system to accomplish the appropriate commutation. The connection diagram of two BLDC motors is presented in Figure 2.

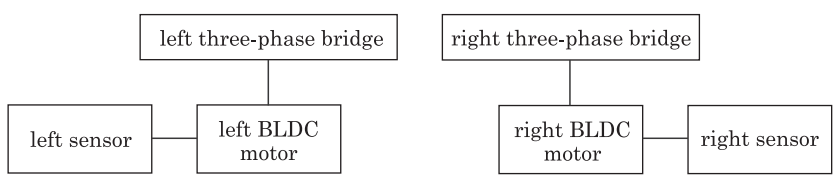

Fig. 2. Motor connection diagram

Power inverter

A BLDC motor is not equipped with a mechanical commutator, and commutation is accomplished electronically with the use of a microcontroller and an inverter. The inverter controls the supply of power between a receiver and the source. The system controls power supply by rapidly turning inverter nodes on and off. Nodes are switched due to changes in the commutation states of inverter branches. The inverter of a BLDC motor relies on voltage-controlled metal-oxide-silicon field-effect transistors (MOSFET). When gate-source voltage alters resistance in the *p*-channel or the *n*-channel, the flow of current changes between the drain and the source.

Methods of controlling a BLDC motor

Brushless DC motors commutate by turning on transistor switches in a given sequence to supply direct current to successive windings. Information about the position of the rotor shaft is provided by the sensor to guarantee that transistors are switched in the appropriate sequence. The inverter control system selects the appropriate transistor pairs by monitoring the rotor's position.

In unipolar mode, pulse amplitude is controlled by groups of positive or negative transistors. Positive transistors control pulse modulation, and negative transistors control commutation. Pulse width is modulated by one transistor group, which simplifies the structure of the electronic circuit. Loads are not evenly distributed across transistors, and switching frequency is irregular. In bipolar mode, upper and lower transistors control PWM and commutation, respectively. This method generates greater losses, but loads are more evenly distributed across transistors, and switching frequency is identical. A universal BLDC motor controller enables the user to select between unipolar and bipolar modes.

Circuit diagram of the three-phase inverter

The controller that powers left and right motor windings at a given commutation sequence features two individual three-phase direct current inverters. Each inverter bridge contains:

– three IR2101 gate drivers,
– three IRLN120N drivers,
– three 1N4148DO rectifier diodes,
– six 100 Ω resistors,
– three 10 uF and 2.2 uF capacitors.

The circuit diagrams of the transistor driver are presented in Figures 3. Coil A_L is connected between the field effect transistor of the top IRLN120N

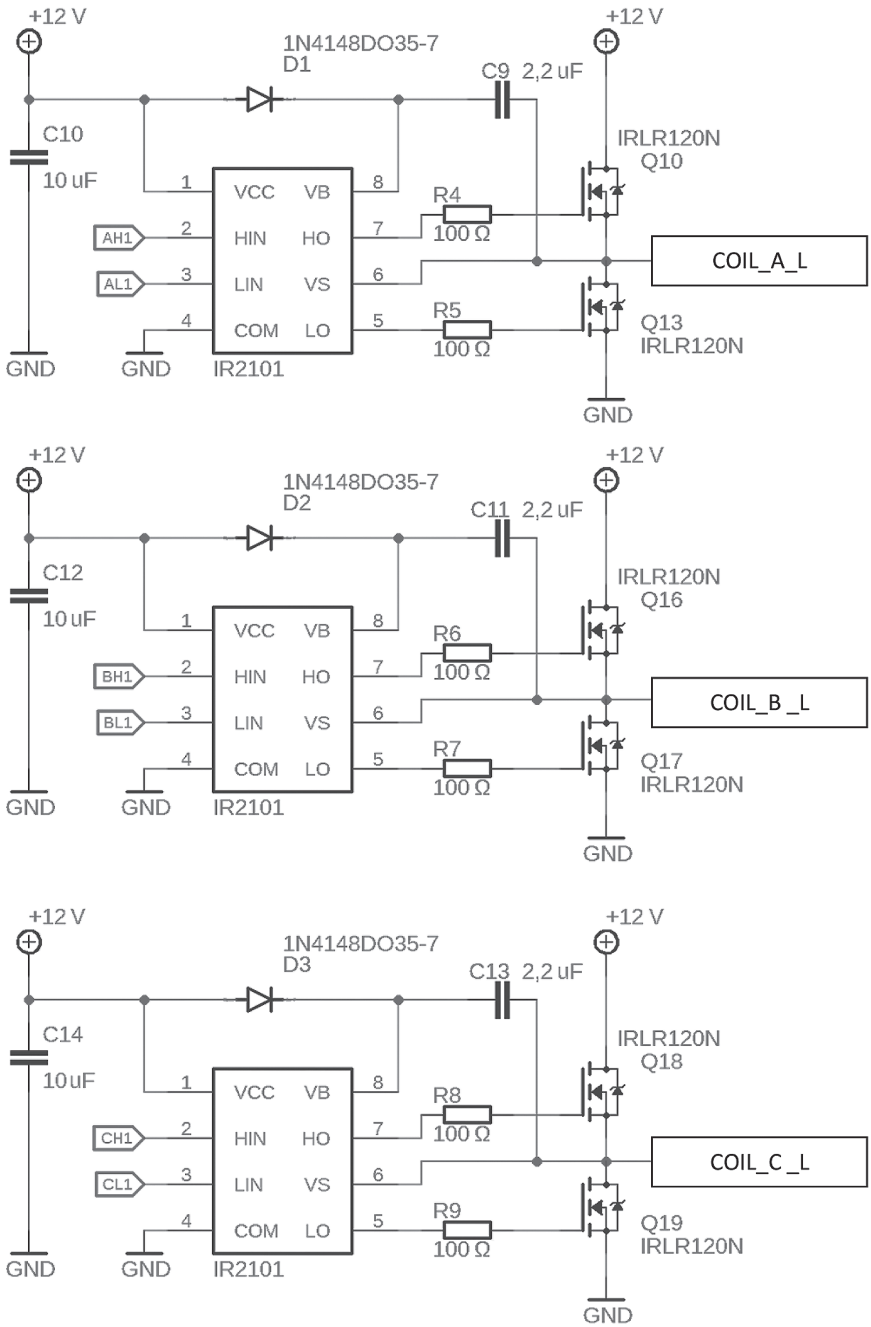

Fig. 3. Circuit diagram of a three-phase inverter connected with coils A_L, B_L and C_L in the left motor and microcontroller output
AH1, AL1, BH1, BL1, CH1 and CL1 that control the left motor

driver and the source of the lower driver. Coils AH, AL, BH, BL, CH and CL are connected with transistor drivers, and they are the microcontroller outputs that carry the PWM signal. The outputs of IR2101 drivers are connected in series with MOSFET transistors.

Determination of rotor position

The brushless motor controller relies on Hall effect sensors to detect rotor position. Sensor data are transmitted to the microcontroller which determines the position of the rotor with the use of an algorithm.

Methods for detecting rotor position

The position of the rotor in a brushless motor has to be determined to commutate the current. Various methods for detecting rotor position are used. A block diagram of a brushless motor control system is presented in Figure 4.

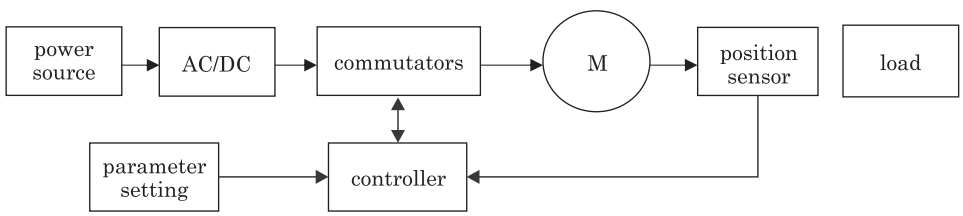

Fig. 4. Block diagram of the motor control system

Four methods are most commonly used to determine rotor position:
– Hall effect sensors,
– optical encoders and pulse sensors,
– rotor and speed calculations,
– counter-EMF measurements.

The first two methods require additional sensors. The following two approaches are sensorless methods that require effective microprocessors to determine the correct moment for energizing stator coils. Hall effect sensors were used in the designed controller. Each stator coil is provided with a Hall effect sensor. The Hall effect is induced when a magnetic field is applied in a direction perpendicular to current flow. The Lorentz force deflects the propagating carriers to one side of the semiconductor. Charges with the opposite sign accumulate on both sides of the semiconductor. Three Hall signals generate six states of commutation in a brushless motor. The resulting information is used to determine the position of the rotor.

Circuit diagram of a Hall effect sensor

Two Hall effect sensor circuits were designed for controlling rotors in the left (Fig. 5) and the right motor.

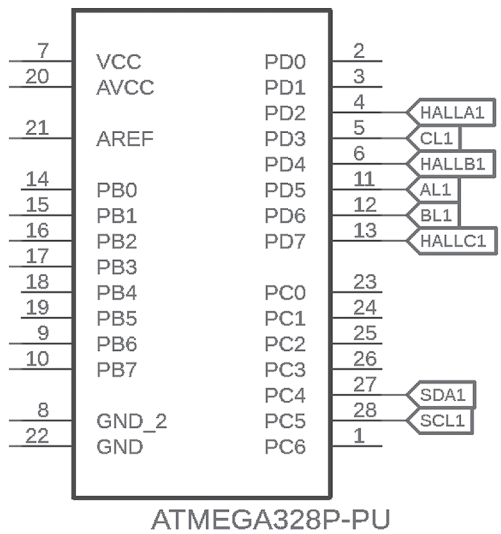

Fig. 5. Circuit diagram for interfacing Hall effect sensors with the microcontroller in the left motor

The circuits presented in Figures 5 contain three Hall effect sensors interfaced with microcontroller outputs. Hall effect sensors in the left motor are labeled as HALLA1, HALLB1, HALLC1. Hall effect sensors in the right motor are labeled as HALLA2, HALLB2, HALLC2. Rotor position sensors are mounted on motor windings.

User console

Brushless motors are controlled from the user console equipped with five pushbuttons and a potentiometer. Button S1 is the forward drive switch, button S2 is the reverse drive switch, button S3 is the right turn switch, button S4 is the left turn switch, and button S5 is the brake switch. Driving speed is controlled with the R19 10 kΩ potentiometer. A circuit diagram of the user console is presented in Figure 6.

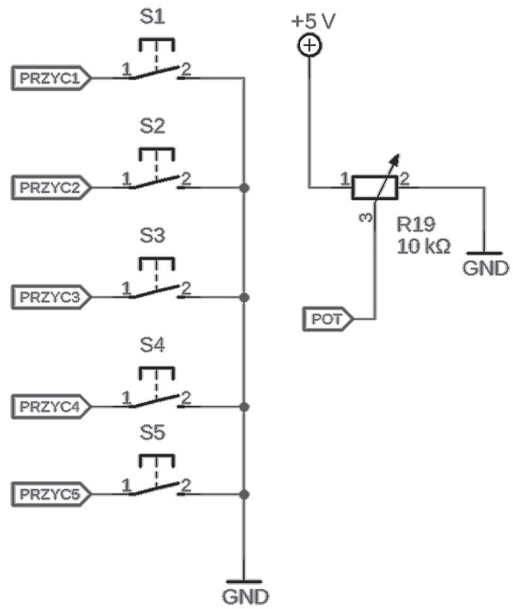

Fig. 6. Circuit diagram of the user console

Buttons 1 to 5 are connected to the inputs of the master microcontroller and the ground terminal GND. Buttons are pressed to initiate current flow between the microcontroller pin and the ground and to execute the corresponding functions in the microcontroller program. A 10 kΩ potentiometer is connected to the analog input of the POT microcontroller and the ground. The potentiometer dial is an adjustable voltage divider that controls resistance between terminals 1-3 and 1-2. Changes in resistance lead to changes in voltage between terminals POT and GND in a range of 0.5 V. The microcontroller checks the voltage applied in the POT analog input and outputs the motor speed.

Communication between microcontrollers

Microcontrollers communicate through a serial bus. The master microcontroller transmits signals to slave microcontrollers that drive the motors. The serial bus supports rapid communication, which ensures the correct operation of motors that power the vehicle's wheels. Data are transmitted with the use of the I^2C bus interface.

Communication interfaces

The microcontrollers are equipped with various communication interfaces that transmit data between sensors, displays and other microcontrollers. Interfaces can operate in serial or parallel mode. Parallel communication is characterized by high-speed data transmission. A higher number of printed circuit boards are required in systems with many communication outputs. The communication interface is controlled by a simple program. The interface circuitry for coupling microprocessors involves various devices such as address decoders, latches and tristate buffers. Serial connections have lower data transmission speeds, they require fewer outputs and simpler printed circuit boards. Serial communication software is complex and characterized by longer processing time. When the number of connections is limited, fewer signal lines are needed, and the system is less sensitive to interference. Both communication modes have their advantages and disadvantages, and they should be selected based on system requirements. The most popular communication interfaces include:

– I²C – Inter-Integrated Circuits,
– SMBus – System Management Bus,
– SPI – Serial Peripheral Interface,
– Microwire,
– 1-Wire.

The designed controller is equipped with a dual bidirectional I²C bus. The bus contains two lines: SDA and SCL. The SDA line transfers data, and SCL is the clock line that synchronizes all data transfers over the I²C bus. The devices on the I²C bus can operate as masters or slaves:

– the master device controls the bus and data transmission, transmits start and stop sequences, and generates clock pulses;
– the slave device responds to the commands of the master device.

Many systems that rely on I²C bus communication have one master microcontroller and numerous slave devices, such as input-output ports, non-volatile memory storage, and display drivers. Every slave device is assigned a unique address for communicating with the master microcontroller. A block diagram of an I²C circuit is presented in Figure 7.

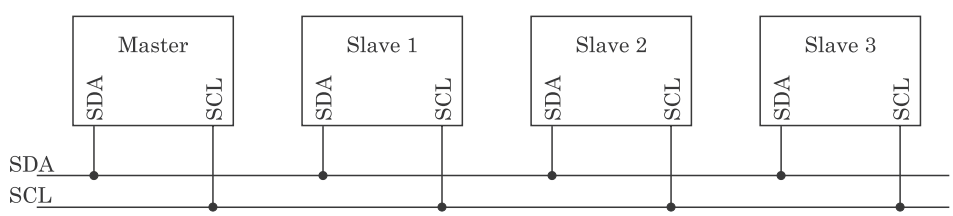

Fig. 7. Block diagram of an I²C circuit

The I²C interface transmits packets of data with a size of 8-bit frames. The number of transmitted bits changes with the system. The receipt of every data frame is acknowledged (ACK). When larger data packets are transmitted, the frames with the most significant bit (MSB) status are sent first. If data cannot be received at a given moment, the SCL clock line can be set to a low state. The transmitter remains in a wait state until the end of the low state interval.

Circuit diagram of the I²C interface

The master microcontroller communicates with motor microcontrollers via the I²C bus interface. The circuit diagram of the bus interface is presented in Figure 8.

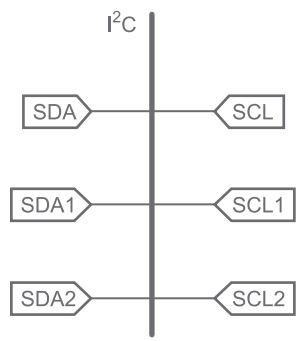

Fig. 8. Circuit diagram of the bus interface

The microcontrollers transmit and receive data via the data bus. In Figure 6, microcontroller pins are labeled as SDA and SCL. SDA1 and SCL1 are the microcontroller pins that control the left motor, and SD2 and SCL2 are the microcontroller pins that control the right motor.

Power supply for the motor controller

The microcontrollers require 5 V DC supply, and motor coils – 12 V DC supply. The described system is powered by a 12 W gel battery. Input voltage for the microcontroller is reduced to 5 V by the Pololu D24V10F5 step-down converter. This 5 V 1 A converter has a high efficiency of 80–93%.

A circuit diagram of the the step-down converter is presented in Figure 7. The gel battery supplies 12 V to the VIN supply voltage input. The VOUT voltage output supplies 5 V to the microcontroller. The GND output is connected to the grounding wire.

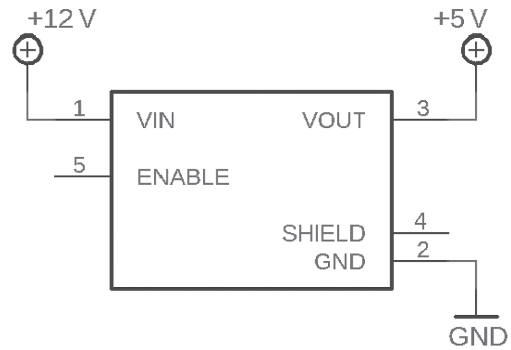

Fig. 9. Circuit diagram of the step-down converter

Summary

The designed controller for brushless DC motors has been patented (SYROKA, KRAJEWSKI 2019) for use in commercial applications. The device can be applied in electric vehicles for controlling BLDC motors mounted in wheels. It was developed as part of a research project at the University of Warmia and Mazury in Olsztyn (Books – Digital Control, SYROKA 2019) dedicated to the construction of electric vehicles and electric drives that rely on renewable sources of energy.

References

ALI E., KHALIGH A., NIE Z., LEE Y.J. 2009. *Integrated Power Electronic Converters and Digital Control*. CRC Press, Boca Raton.

BOLTON W. 2006. *Programmable Logic Controllers*. Elsevier, Amsterdam, Boston.

BUSO S., MATTAVELLI P. 2006. *Digital Control in Power Electronics*. Morgan & Claypool Publisher, San Rafael, CA.

CHEN C.-T. 1991. *Analog and Digital Control system Design: Transfer Function, State Space, and Algebraic Methods*. Saunders College Publishing, Filadelfia, Pensylwania.

DENTON T. 2016. *Electric and Hybrid Vehicles*. Routledge, San Diego.

DORF R.C., BISHOP R.H. 2008. *Modern Control System Solution Manual*. Prentice Hall, New Jersey.

FADALI S. 2009. *Digital Control Engineering, Analysis and Design*. Elsevier, Burlington.

FEUER A., GOODWIN G.C. 1996. *Sampling in Digital Signal Processing and Control*. Brikhauser, Boston.

GABOR R., KOWOL M., KOŁODZIEJ J., KMIECIK S., MYNAREK P. 2019. *Switchable reluctance motor, especially for the bicycle*. Patent No 231882.

GLINKA T., FRĘCHOWICZ A. 2007. *Brushless DC motor speed control system*. Patent No.P195447.

GREGORY P. 2006. *Starr Introduction to Applied Digital Control*. Gregory P. Starr, New Mexico.

HUSAIN I. 2003. *Electric and Hybrid Vehicles, Design Fundamentals*. CRC Press LLC, Boca Raton, London.

JONGSEONG J., WONTAE J. 2019. *Method of controlling constant current of brushless dc motor and controller of brushless dc motor using the same*. United States Patent Application Publication, US2018323736 (A1).

KHAJEPOUR A., FALLAH S., GOODARZI A. 2014. *Electric and Hybrid Vehicles Technologies, Modeling and Control: a Mechatronic Approach*. John Wiley & Sons Ltd, Chichester.

KOJIMA N., ANNAKA T. 2019. *Motor control apparatus and motor unit*. United States Patent Application Publication, US2019047517 (A1).

KOLANO K. 2020. *Method for measuring the angular position of the shaft of a brushless DC motor with shaft position sensors*. Patent No.P235653.

LANDAU I.D., ZITO G. 2006. *Digital Control Systems Design, Identification and Implementation*. Springer, London.

LUECKE J. 2005. *Analog and Digital Circuits for Electronic Control System Applications Using the TI MSP430 Microcontroller*. Elsvier, Amsterdam, Boston

MI CH., MASRUR M.A., GAO D.W. 2011. *Hybrid Electric Vehicles Principles and Applications with Practical Perspectives*. John Wiley & Sons Ltd., Chichester.

MOUDGALYA K.M. 2007. *Digital Control*. John Wiley & Sons Ltd., Chichester.

MURRAY R.M., LI Z., SHANKAR SASTRY S. 1994. *A Mathematical Introduction to Robotic Manipulation*. CRC Press, Berkeley.

OGATA K. 1995. *Discrete Time Control Systems*. Prentice-Hall, New Jersey.

PISTOIA G. 2010. *Electric and Hybrid Vehicles Power Sources, Models, Sustainability, Infrastructure and the Market*. Elsevier, Amsterdam, Boston.

SIKORA A., ZIELONKA A. 2011. *Power supply system for a BLDC motor*. patent No. P.394971.

SOYLU S. 2011. *Electric Vehicles – the Benefits and Barriers*. Edited by Seref Soylu, Rijeka.

STEVIĆ Z. 2013. *New Generation of Electric Yehicles*. Edited by Zoran Stević, Rijeka.

SYROKA Z., KRAJEWSKI K. 2019. *Controller for brushless DC motors*. Patent No. P431380, filing date: 4 October 2019.

SYROKA Z.W. 2019. *Electric Vehicels – Digital Control*. Scholars' Press, Mauritius.

ŚLUSAREK B. , PRZYBYLSKI M., GAWRYŚ P. 2014. *Hall effect sensor of the shaft position of the brushless DC motor*. Patent No.P218476.

WILLIAMSON S.S. 2013. *Energy Management Strategies for Electric and Plug-in Hybrid Electric Vehicles*. Springer, New York, London.

Guide for Autors

Introduction

Technical Sciences is a peer-reviewed research Journal published in English by thePublishing House of the University of Warmia and Mazury in Olsztyn (Poland). Journal is published continually since 1998. Until 2010 Journal was published as a yearbook, in 2011 and 2012 it was published semiyearly. From 2013, the Journal is published quarterly in the spring, summer, fall, and winter.

The Journal covers basic and applied researches in the field of engineering and the physical sciences that represent advances in understanding or modeling of the performance of technical and/or biological systems. The Journal covers most branches of engineering science including biosystems engineering, civil engineering, environmental engineering, food engineering, geodesy and cartography, information technology, mechanical engineering, materials science, production engineering etc.

Papers may report the results of experiments, theoretical analyses, design of machines and mechanization systems, processes or processing methods, new materials, new measurements methods or new ideas in information technology.

The submitted manuscripts should have clear science content in methodology, results and discussion. Appropriate scientific and statistically sound experimental designs must be included in methodology and statistics must be employed in analyzing data to discuss the impact of test variables. Moreover there should be clear evidence provided on how the given results advance the area of engineering science. Mere confirmation of existing published data is not acceptable. Manuscripts should present results of completed works.

There are three types of papers: a) research papers (full length articles); b) short communications; c) review papers.

The Journal is published in the printed and electronic version. The electronic version is published on the website ahead of printed version of Technical Sciences.

Technical Sciences does not charge submission or page fees.

Types of paper

The following articles are accepted for publication:

Reviews

Reviews should present a focused aspect on a topic of current interest in the area of biosystems engineering, civil engineering, environmental engineering, food engineering, geodesy and cartography, information technology, mechanical engineering, materials science, production engineering etc. They should include all major findings and bring together reports from a number of sources. These critical reviews should draw out comparisons and conflicts between work, and provide an overview of the 'state of the art'. They should give objective assessments of the topic by citing relevant published work, and not merely present the opinions of individual authors or summarize only work carried out by the authors or by those with whom the authors agree. Undue speculations should also be avoided. Reviews generally should not exceed 6,000 words.

Research Papers

Research Papers are reports of complete, scientifically sound, original research which contributes new knowledge to its field. Papers should not exceed 5,000 words, including figures and tables.

Short Communications

Short Communications are research papers constituting a concise description of a limited investigation. They should be completely documented, both by reference list, and description of the experimental procedures. Short Communications should not occupy more than 2,000 words, including figures and tables.

Letters to the Editor

Letters to the Editor should concern with issues raised by articles recently published in scientific journals or by recent developments in the engineering area.

Contact details for submission

The paper should be sent to the Editorial Office, as a Microsoft Word file, by e-mail: techsci@uwm.edu.pl

Referees

Author/authors should suggest, the names, addresses and e-mail addresses of at least three potential referees. The editor retains the sole right to decide whether or not the suggested reviewers are used.

Submission declaration

After final acceptance of the manuscript, the corresponding author should send to the Editorial Office the author's declaration. Submission of an article implies that the work has not been published previously (except in the form of an abstract or as part of a published lecture or academic thesis or as an electronic preprint), that it is not under consideration for publication elsewhere, that publication is approved by all authors and tacitly or explicitly by the responsible authorities where the work was carried out, and that, if accepted, it will not be published elsewhere in the same form, in English or in any other language.

To prevent cases of ghostwriting and guest authorship, the author/authors of manuscripts is/are obliged to: (i) disclose the input of each author to the text (specifying their affiliations and contributions, i.e. who is the author of the concept, assumptions, methods, protocol, etc. used during the preparation of the text); (ii) disclose information about the funding sources for the article, the contribution of research institutions, associations and other entities.

Language

Authors should prepare the full manuscript i.e. title, abstract and the main text in English (American or British usage is accepted). Polish version of the manuscript is not required.

The file type

Text should be prepared in a word processor and saved in doc or docx file (MS Office).

Article structure

Suggested structure of the manuscript is as follows:

Title
Authors and affiliations
Corresponding author
Abstract
Keywords
Introduction
Material and Methods
Results and Discussion
Conclusions

Acknowledgements (optional)
References
Tables
Figures

Subdivision – numbered sections

Text should be organized into clearly defined and numbered sections and subsections (optionally). Sections and subsections should be numbered as 1. 2. 3. then 1.1 1.2 1.3 (then 1.1.1, 1.1.2, …). The abstract should not be included in numbering section. A brief heading may be given to any subsection. Each heading should appear on its own separate line. A single line should separate paragraphs. Indentation should be used in each paragraph.

Font guidelines are as follows:

– Title: 14 pt. Times New Roman, bold, centered, with caps
– Author names and affiliations:12 pt. Times New Roman, bold, centered, italic, two blank line above
– Abstract: 10 pt. Times New Roman, full justified, one and a half space. Abstract should begin with the word Abstract immediately following the title block with one blank line in between. The word Abstract: 10 pt. Times New Roman, centered, indentation should be used
– Section Headings: Not numbered, 12 pt. Times New Roman, bold, centered; one blank line above
– Section Sub-headings: Numbered, 12 pt. Times New Roman, bold, italic, centered; one blank line above
– Regular text: 12 pt. Times New Roman, one and a half space,full justified, indentation should be used in each paragraph

Title page information

The following information should be placed at the first page:

Title

Concise and informative. If possible, authors should not use abbreviations and formulae.

Authors and affiliations

Author/authors' names should be presented below the title. The authors' affiliation addresses (department or college; university or company; city, state and zip code, country) should be placed below the names. Authors with the same affiliation must be grouped together on the same line with affiliation information following in a single block. Authors should indicate all affiliations with a lower-case superscript letter immediately after the author's name and in front of the appropriate address.

Corresponding author

It should be clearly indicated who will handle correspondence at all stages of refereeing and publication, also post-publication process. The e-mail address should be provided (footer, first page). Contact details must be kept up to date by the corresponding author.

Abstract

The abstract should have up to 100-150 words in length. A concise abstract is required. The abstract should state briefly the aim of the research, the principal results and major conclusions. Abstract must be able to stand alone. Only abbreviations firmly established in the field may be eligible. Non-standard or uncommon abbreviations should be avoided, but if essential they must be defined at their first mention in the abstract itself.

Keywords

Immediately after the abstract, author/authors should provide a maximum of 6 keywords avoiding general, plural terms and multiple concepts (avoid, for example, 'and', 'of'). Author/authors should be sparing with abbreviations: only abbreviations firmly established in the field may be eligible.

Abbreviations

Author/authors should define abbreviations that are not standard in this field. Abbreviations must be defined at their first mention there. Author/authors should ensure consistency of abbreviations throughout the article.

Units

All units used in the paper should be consistent with the SI system of measurement. If other units are mentioned, author/authors should give their equivalent in SI.

Introduction

Literature sources should be appropriately selected and cited. A literature review should discuss published information in a particular subject area. Introduction should identify, describe and analyze related research that has already been done and summarize the state of art in the topic area. Author/authors should state clearly the objectives of the work and provide an adequate background.

Material and Methods

Author/authors should provide sufficient details to allow the work to be reproduced by other researchers. Methods already published should be indicated by a reference. A theory should extend, not repeat, the background to the article already dealt within the Introduction and lay the foundation for further work. Calculations should represent a practical development from a theoretical basis.

Results and Discussion

Results should be clear and concise. Discussion should explore the significance of the results of the work, not repeat them. A combined Results and Discussion section is often appropriate.

Conclusions

The main conclusions of the study may be presented in a Conclusions section, which may stand alone or form a subsection of a Results and Discussion section.

Acknowledgements

Author/authors should include acknowledgements in a separate section at the end of the manuscript before the references. Author/authors should not include them on the title page, as a footnote to the title or otherwise. Individuals who provided help during the research study should be listed in this section.

Artwork

General points

– Make sure you use uniform lettering and sizing of your original artwork
– Embed the used fonts if the application provides that option
– Aim to use the following fonts in your illustrations: Arial, Courier, Times New Roman, Symbol
– Number equations, tables and figures according to their sequence in the text
– Size the illustrations close to the desired dimensions of the printed version

Formats

If your electronic artwork is created in a Microsoft Office application (Word, PowerPoint, Excel) then please supply 'as is' in the native document format

Regardless of the application used other than Microsoft Office, when your electronic artwork is finalized, please 'Save as' or convert the images to one of the following formats (note the resolution requirements given below):

EPS (or PDF): Vector drawings, embed all used fonts

JPEG: Color or grayscale photographs (halftones), keep to a minimum of 300 dpi

JPEG: Bitmapped (pure black & white pixels) line drawings, keep to a minimum of 1000 dpi or combinations bitmapped line/half-tone (color or grayscale), keep to a minimum of 500 dpi

Please do not:

– Supply files that are optimized for screen use (e.g., GIF, BMP, PICT, WPG); these typically have a low number of pixels and limited set of colors
– Supply files that are too low in resolution
– Submit graphics that are disproportionately large for the content

Color artwork

Author/authors should make sure that artwork files are in an acceptable format (JPEG, EPS PDF, or MS Office files) and with the correct resolution. If, together with manuscript, author/authors submit color figures then Technical Sciences will ensure that these figures will appear in color on the web as well as in the printed version at no additional charge.

Tables, figures, and equations

Tables, figures, and equations/formulae should be identified and numbered consecutively in accordance with their appearance in the text.

Equations/mathematical and physical formulae should be presented in the main text, while tables and figures should be presented at the end of file (after References section). Mathematical and physical formulae should be presented in the MS Word formula editor.

All types of figures can be black/white or color. Author/authors should ensure that each figure is numbered and has a caption. A caption should be placed below the figure. Figure must be able to stand alone (explanation of all symbols and abbreviations used in figure is required). Units must be always included. It is noted that figure and table numbering should be independent.

Tables should be numbered consecutively in accordance with their appearance in the text. Table caption should be placed above the table. Footnotes to tables should be placed below the table body and indicated with superscript lowercase letters. Vertical rules should be avoided. Author/authors should ensure that the data presented in tables do not duplicate results described in figures, diagrams, schemes, etc. Table must be able to stand alone (explanation of all symbols and abbreviations used in table is required). Units must be always included. As above, figure and table numbering should be independent.

References

References: All publications cited in the text should be presented in a list of references following the text of the manuscript. The manuscript should be carefully checked to ensure that the spelling of authors' names and dates of publications are exactly the same in the text as in the reference list. Authors should ensure that each reference cited in the text is also present in the reference list (and vice versa).

Citations may be made directly (or parenthetically). All citations in the text should refer to:

1. Single author

The author's name (without initials, with caps, unless there is ambiguity) and the year of publication should appear in the text

2. Two authors

Both authors' names (without initials, with caps) and the year of publication should appear in the text

3. Three or more authors

First author's name followed by et al. and the year of publication should appear in the text

Groups of references should be listed first alphabetically, then chronologically.

Examples:

"... have been reported recently (ALLAN, 1996a, 1996b, 1999; ALLAN and JONES, 1995). KRAMER et al. (2000) have recently shown..."

The list of references should be arranged alphabetically by authors' names, then further sorted chronologically if necessary. More than once reference from the same author(s) in the same year must be identified by the letters "a", "b", "c" etc., placed after the year of publication.

References should be given in the following form:

KUMBHAR B.K., AGARVAL R.S., DAS K. 1981. Thermal properties of fresh and frozen fish. International Journal of Refrigeration, 4(3), 143–146.

MACHADO M.F., OLIVEIRA F.A.R., GEKAS V. 1997. Modelling water uptake and soluble solids losses by puffed breakfast cereal immersed in water or milk. In Proceedings of the Seventh International Congress on Engineering and Food, Brighton, UK.

NETER J., KUTNER M.H., NACHTSCHEIM C.J., WASSERMAN W. 1966. Applied linear statistical models (4th ed., pp. 1289–1293). Irwin, Chicago.

THOMSON F.M. 1984. Storage of particulate solids. In M. E. Fayed, L. Otten (Eds.), Handbook of Powder Science and Technology (pp. 365–463). Van Nostrand Reinhold, New York.

Citation of a reference as 'in press' implies that the item has been accepted for publication.

Note that the full names of Journals should appear in reference list.

Submission checklist

The following list will be useful during the final checking of an article prior to the submission. Before sending the manuscript to the Journal for review, author/authors should ensure that the following items are present:

– Text is prepared with a word processor and saved in DOC or DOCX file (MS Office). One author has been designated as the corresponding author with contact details: e-mail address
– Manuscript has been 'spell-checked' and 'grammar-checked'
– References are in the correct format for this Journal
– All references mentioned in the Reference list are cited in the text, and vice versa
– Author/authors does/do not supply files that are too low in resolution
– Author/authors does/do not submit graphics that are disproportionately large for the content